BRNO UNIVERSITY OF TECHNOLOGY

VYSOKÉ UČENÍ TECHNICKÉ V BRNĚ

FACULTY OF MECHANICAL ENGINEERING

FAKULTA STROJNÍHO INŽENÝRSTVÍ

INSTITUTE OF PHYSICAL ENGINEERING

ÚSTAV FYZIKÁLNÍHO INŽENÝRSTVÍ

LASER WITH NAROW SPECTRAL LINEWIDTH FOR METROLOGY OF LENGTH

JEDNOFREKVENČNÍ LASER S ÚZKOU SPEKTRÁLNÍ ČÁROU PRO METROLOGII DÉLEK

DOCTORAL THESIS
DIZERTAČNÍ PRÁCE

AUTHOR   Ing. Minh Tuan Pham
AUTOR PRÁCE

SUPERVISOR   Ing. Ondřej Číp, Ph.D.
ŠKOLITEL

BRNO 2022

Abstrakt

Práce se zabývá stabilizací diodového laseru pracujícího na vlnové délce 729 nm, který slouží pro přesnou spektroskopii a interakci se zachycenými a zchlazenými ionty vápníku. Interakce s iontem vyžaduje, aby excitační laser měl extrémně úzkou šířku spektrální čáry. V práci jsou vysvětleny důležité postupy a metody vedoucí k dosažení provozu laseru se spektrální šířkou čáry v řádu Hz či nižší. Součástí práce je sestavení optické sestavy pro tento laser a k ní potřebných elektro-optických prvků. Hlavní důraz je kladen na techniky stabilizace laserové frekvence pomocí externích referencí, jejich teoretický popis a implementace je rovněž součástí této práce. Jako první přístup o zúžení spektrální čáry je zvolena metoda uzamknutí optické frekvence laseru na vybranou komponentu hřebene optických frekvencí pomocí elektronických fázových závěsů. Měření spektrálního šumu bylo provedeno pomocí dvousvazkového interferometru s nevyváženými rameny. Dosažené výsledky potlačení šumu u takto uzamčeného laseru byly poté porovnány s režimem laseru volně běžícího. Dalším postupem je uzamčení spektrální čáry laseru na velmi úzkou čáru vysoce jakostního optického rezonátoru. Touto metodou jsem dosáhl laseru s velmi úzkou spektrální čáru (v řádech desítek Hz), avšak s krátkodobou stabilitou. Finálním krokem bylo pak sestavení a použití techniky "trasfer oscillator", která zajistila dodatečnou kompenzaci nežádoucího driftu rezonančního modu optického rezonátoru a tímž zajistila dlouhodobou stabilitou celého systému. Takto stabilizovaný laser na 729 nm byl testován ve spektroskopii na zakázaném přechodu Dopplerovsky zchlazeného iontu vápníku.

Klíčová slova

Polovodičový laser s externím rezonátorem, optický rezonátor s vysokou jakostí, šířka spektrální čáry,stabilizace frekvence, kalciové hodiny, hodinový laser, fázový závěs, technika "transfer oscillator".

Abstract

The thesis deals with stabilising a diode laser operating at a wavelength of 729 nm, which is used for high-resolution spectroscopy and interacting with captured and cooled calcium ions. Interaction with the ion requires an extremely narrow spectral linewidth for the excitation laser. The work explains essential procedures and methods leading to the operation of a laser with a spectral linewidth in the order of Hz or less. The central part of the work is to design and put together an optical assembly for this laser with the necessary electro-optical elements. The main emphasis is placed on laser frequency stabilisation techniques using external references, their theoretical description and implementation are also a part of this work. The first chosen approach to narrowing the spectral linewidth is locking the optical frequency of the laser to a selected component of the optical frequency comb using electronic phase locks. Spectral noise measurements were performed using a two-beam interferometer with unbalanced arms. The achieved noise suppression results for the locked laser were then compared with the free-running laser mode. Another approach is to lock the spectral line of the laser to a very narrow line of a high-quality optical resonator. With this method, I achieved a laser with a very narrow spectral line (in the order of tens of Hz), however, with short-term stability. The next step was the construction and use of the "transfer oscillator" technique, which provided additional compensation for the unwanted drift of the resonance mode of the optical resonator and thereby ensured the long-term stability of the entire system. The laser stabilised in this way at 729 nm was tested in spectroscopy on the forbidden transition of the Doppler-cooled calcium ion.

Prohlášení

Prohlašuji, že jsem disertační práci vypracoval samostatně, pouze za odborného vedení Ing. Onřeje Čípa, Ph.D., a všechny podklady jsou uvedeny v seznamu použité literatury.

....   V Brně 25. května 2022

Contents

List of Abbreviation

ADC	Analog to digital converter
AOM	Acousto-optic modulator
APD	Avalanche photodiode
BP	Band-pass filter
CAS	Czech Academy of Sciences
CAN	Controller area network
CCD	Charge-coupled device
CRDS	Cavity ring-down spectroscopy
CAN	Controller Area Network
CTU	Czech Technical University
DAC	Digital to analog converter
DDS	Direct digital synthesis(synthesizer)
DSP	Digital signal processor
DM	Demineralized water
ECDL	External Cavity Diode Laser
EMCCD	Electron Multiplying Charge-Coupled Device
EOM	Electro-optic modulator
Fceo	Offset frequency
Frep	Repetition frequency
FSR	Free spectral range
FM	frequency modulation
FNC	Fibre noise cancellation
FPI	Fabri-Perot interferometers
FWHM	Full width at half maximum
H-maser	Hydrogen maser
HF-cavity	High finesse cavity
HR	High reflected
HPLC	High performance liquid chromatography
ISI	Institute of Scientific Instruments
I and Q	in-phase and quadrature
L377	Laser working on 377 nm
L422	Laser working on 422 nm
L854	Laser working on 854 nm
L866	Laser working on 866 nm
L729	Laser working on 729 nm
L1540	Laser working on 1540 nm
LP	Low-pass filter
MCU	Micro-controller unit

MZI	Mach-Zehnder interferometer
NBS	National Bureau od Standards
NEG	non-evaporative getter
NIST	National Institute of Standards and Technology
OC	Optical clock
OFC	Optical frequency comb
OFHC	Oxygen free high conductivity
PBS	Polarisation beam splitter
PCM	Plane-concave mirros
PE	Peltier element
PD	Photodetector
PDH	Pound–Drever–Hall
PID	Proportional–integral–derivative
PLL	Phase-locked loop
PSD	Power Spectral Density
PPM	Plane-parallel mirror
RAM	Residual amplitude modulation
RF	Radio frequency
RFFA	Radio frequency signal analyzer
SB	Sideband
SHG	Second harmonic generation
SI	International System of Units
SNR	Signal to noise ratio
SPI	Serial peripheral interface
TA	Taped amplifier
TM	Transversal Mode
TO	Transfer oscillator
TS	Temperature sensor
UHV	Ultra high vacuum
ULE	Ultra low expansion
VCO	Voltage Controlled Oscillator

Introduction and structure of the work

A *clock* is a device that uses the stable oscillation pattern as a reference (i.e. pendulum, quartz). An atomic clock is a laser whose frequency is stabilised relative to a narrow optical atomic transition. Thus the oscillator, in this case, is a trapped and isolated atom with a natural, very high oscillation rate. Thanks to this revolutionary idea and evolution of atomic frequency and time standards have taken a huge leap forward [1, 2, 3]. For nearly 100 years, the atomic frequency standard played a critical role in basic science and precision measurement. During this period, the increasing need for more precise timing and synchronisation for various applications, including navigation or test of fundamental physic, has demanded oscillators with higher frequencies and higher performance. The most recent clock can reach the stability or instability of 1.5 parts in a quintillion (1 followed by 18 zeros) in just a few thousand seconds [4].

Chap. 1 presents a brief history of time, the latest and the most stable optical clocks at present, and the theoretical background of optical atomic clocks. Furthermore, it consists of the general level scheme of the $^{40}Ca^+$ ion and summarises its interaction with the laser waves.

This work closely relates to an optical atomic clock with a single $^{40}Ca^+$ ion. The infrastructure consisting of trapping apparatus, ultra-high vacuum chamber, laser requirement, and electronics was developed and fully built at the Institute of Scientific Instruments (ISI) in Brno. The inverse of the lifetime gives a natural linewidth of this electric quadrupole transition. Therefore to be able to coherently transfer population between $4^2S_{1/2} \leftrightarrow 3^2D_{5/2}$ energy level, one needs a clock laser with an ultra-narrow spectral linewidth. This is a crucial part of the optical setup when realising the optical atomic clocks.

The main aim of this work is to design and build such a spectroscopy laser. The work focuses on implementing the best possible method for linewidth suppression available. The spectroscopy laser with suppressed linewidth to sub-Hz level gives us a tool for many experiments with trapped ions. Apart from the high-resolution spectroscopy on the ion forbidden transition for optical clock operations, it also allows us to individually manipulate the quantum state of ions. Thus, the clock laser is a gate for the information processing with cold ions going to quantum computers or quantum simulators [5].

The selection of primary laser source, its characterisation and noise properties measurement is presented in Chap. 2. Chap 3 covers a theoretical background of available methods for laser linewidth narrowing and their application in the set of my pilot experimental setup.

Chap. 4 is key part of my work, where a complex optical and electronic setup is build-up and experimentally verified and adjusted on the best operating conditions.

Chap. 5 shows my results of implemented methods by using the laser for coherent excitation of $4^2S_{1/2} \leftrightarrow 3^2D_{5/2}$ transition.

Chap 5.3.2 includes a summary of my work on the clock laser setup. I also define

the following steps to improve further the laser linewidth narrowing and the principles of delivering the resulting clock laser beam to the vacuum chamber with trapped ions.

To support the importance of this work, I have attached a three selected papers. Their reprints, brief summary, and my contribution are included in appendix I, II, III.

Background of the research topic

This work has been done under the project on trapping and laser cooling of ions, which started in 2014. It is solved with the cooperation of two research groups. Our group from the Department of Coherence Optics of the Institute of Scientific Instruments CAS focuses on the infrastructure for the ion trapping and cooling, development of a Doppler cooling lasers, construction of the highly coherent laser source working at 729 nm and precision spectroscopy with ions stored in the radio frequency trap placed in the ultra-high vacuum chamber (both parts belong to my thesis).

The main research aim of our group is frequency metrology with the cold ion, which might be used for the realisation of an experimental optical atomic clocks. The second group is the team from the Department of Optics of Palacky University Olomouc. They focus mainly on quantum mechanics and information processing like quantum algorithms and multiparticle entanglement. We all used same electro-optical setup with some modifications. The overview of the Optical table, where all the laser are prepared before being coupled and sent to particular assignment in the laboratory can be seen on Fig. 1. The overview over the trap apparatus with necessary electro-optical parts for Doppler cooling, sideband cooling and ion interrogation can be seen in Fig. 2. Although the vacuum chamber, Paul trap, and a number of necessary supporting parts for ion trapping were not directly the topic of my doctoral thesis, I participated significantly in the design, assembly and overall tuning of this complex arrangement.
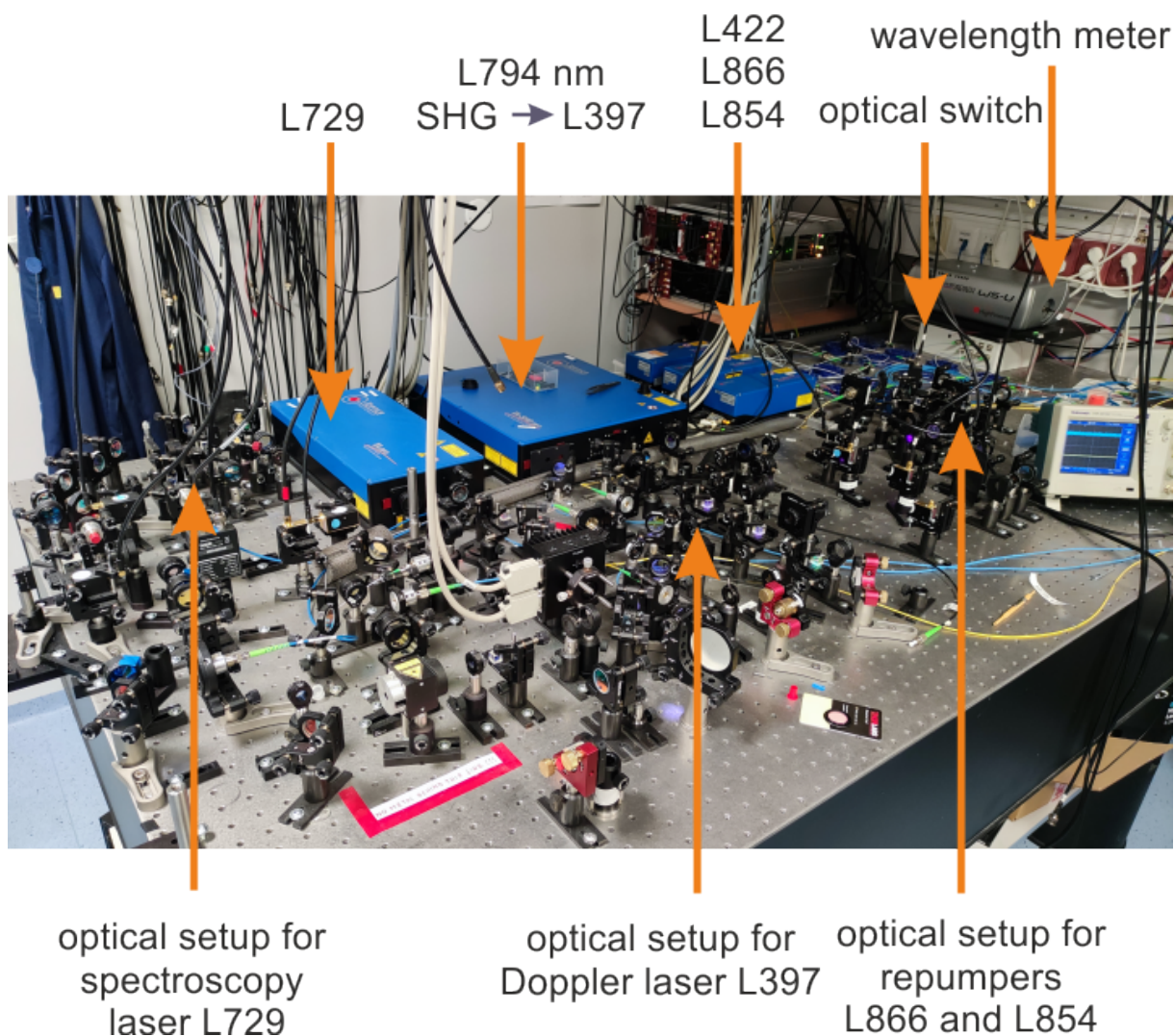
Figure 1: The overview over the optical table, where all the lasers are prepared before being coupled and sent into the chamber with the trapped ion. The main laser source is generally divided to many path, which then can be used for stabilisation to wavelength meter or are sent to another laboratory, where they are optically beat-noted with optical frequency comb. Each laser has several acousto-optic modulators placed in their path. They are used for frequency shifting, intensity stabilisation or serve in pulse sequence.
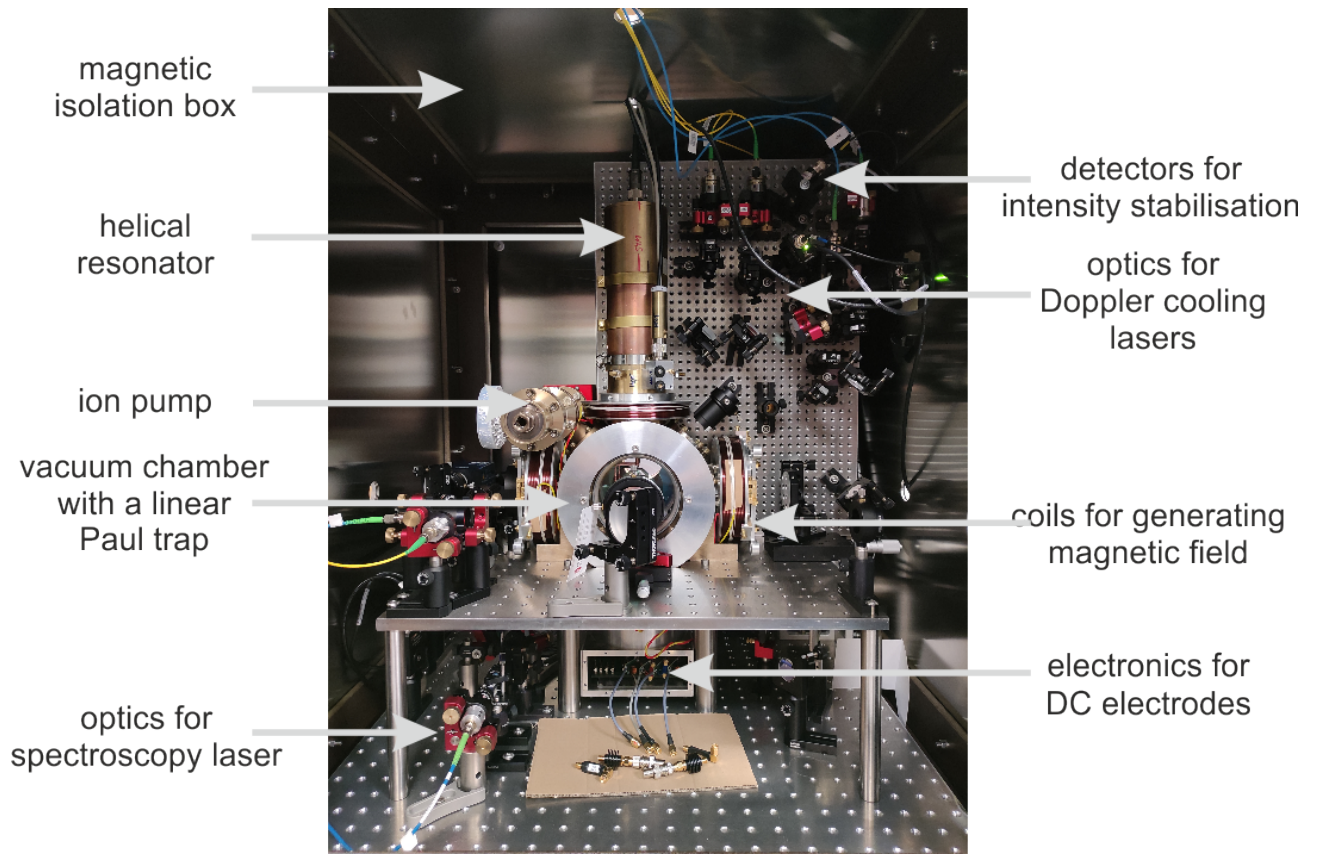
Figure 2: Ion trap apparatus with all necessary optics for Doppler cooling, sideband cooling and ion interrogation. The lasers are brought into setup via polarisation maintaining fibres. Inside the passive magnetic box, a part of the power is steered into photodetector for intensity stabilisation purposes. The main beam are prepared in terms of polarisation and position adjustment before entering the vacuum chamber. The ion fluorescence is collected by an collimating optic into an avalanche detector. One can also see the Helix resonator and all necessary electronic parts and the ion pump.

1.   Optical atomic clock

1.1   History of clockworks

Time is one of the seven fundamental physical quantities which are distinct in nature. For thousands of years, the time has accompanied man in his daily life. It told him when to plant seeds and when to harvest, when to expect dry seasons and when to prepare for winter. For that and many more reasons, ancient civilisations observed astronomical bodies to learn and determine a time, dates and seasons. They had done it by dividing natural cycles into smaller periods. A year, which is the time when earth finished one circle around the Sun, was divided into twelve months, which is the number of Moon cycles in a year. A month is then divided into four periods as it goes by four phases of the moon as it circles the earth. A day was established as one rotation around its axis, and day and night were evenly divided into 12 sections. Thus, the 24-hour day was born. Remains of those times can still be found in stone circles such as England Stonehenge and several others that are scattered around the world [6]. They have been thought to be used to predict seasonal and annual events such as equinoxes or solstices [7]. However, little is known of their civilisation or calendars as there is not much information recorded.

The first mention of the timekeeping method comes from Sumerians nearly 4000 years ago. This method is called hexagesimal timekeeping [7]. And nowadays, it is well known in both Western and Eastern societies. This numerical system has sixty as a base number. The exact reason they choose this system is unknown; however one theory is quite reasonable. At that time, people were used to counting on their hands. Using the thumb as a pointer to each finger bone on the rest four fingers, they can count to 12. Moreover, five fingers times 12 is 60. Also, the number 60 is a highly composite number having 12 factors, namely 1, 2, 3, 4, 5, 6, 10, 12, 15, 20, 30, and 60. The result is that one hour can be divided evenly into a section of 30 minutes, 20 minutes, and finally - 1 minute.

To be able to keep track of time, the first clock was invented. The so-called shadow clock, first used by Egyptians, consists of an obelisk in the middle of Circe. The half of this clocks disc was divided into 12 even sections and served as a sundial. According to the position of the Sun in the sky, an obelisk cast the shadow on the sundial showing the actual time. Although this method was very accurate, it still relied on the Sun and thus was useless at night or in a cloudy weather. Therefore several alternative timekeeping methods were developed. Among them were the water clock, merkhet clock, candle clock, sand clock, clock moon dial, etc.

The era of precision timekeeping comes with the pendulum clock. The first pendulum clock was designed and constructed by Christian Huygens, a Dutch scientist, in 1656 [8]. The advantage of a pendulum is that it works as a mechanical oscillator. Dependent on its length, the pendulum swings forth and back in a precise time interval and resists swinging at other rates. An early version of this clock goes off by less than one minute per day, and later only by 10 seconds per day, a very accurate for that time. Huygens

then invented another mechanical device, a spiral balance spring system that works like a pendulum in a clock that oscillates at a fixed resonant frequency. This portable device lays the foundation for the modern watchmaking industry. For centuries those watches have worked just fine. Then a new natural source of oscillation was discovered.

In 1880 Jacques and Pierre Curie discovered the piezoelectric properties of crystalline quartz. They found that when the electricity was applied to quartz, it vibrated at a specific, incredibly stable rate. The oscillation of quartz was more than 32000 times per second. Counting this oscillation would make an incredible precise clock. The first crystal oscillator was built in 1921, and the first quartz clock in 1927 by Warren Morrison and J. W. Horton at Bell Telephone Laboratories in Canada [9]. Those clocks would go off by 15 seconds per month. The National Bureau of Standards (NBS), now known as the National Institute for Standards and Technology (NIST), based the time standards of the United States on quartz clocks until the 1960s, when in change to today, the most precise timekeeping device, the Atomic clock.
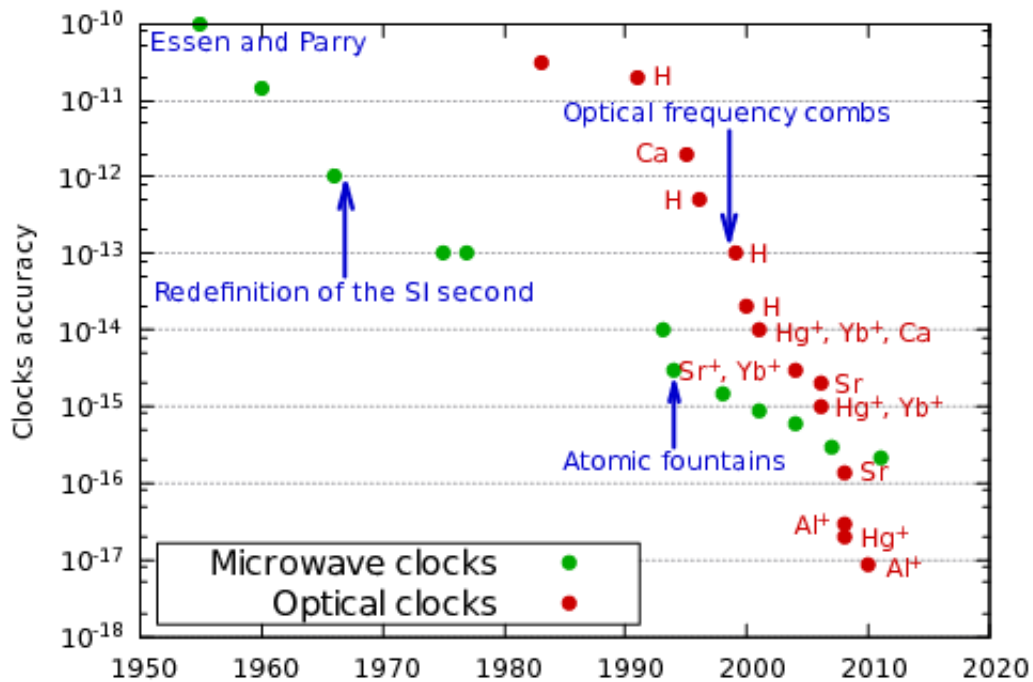
Figure 1.1: Accuracy record for microwave and optical clocks [10]. From the first Cs clock by Essen and Parry in the 1950s, clocks are getting better every year. Since development of optical frequency combs the performance of the optical clock has overcome microwave clock.

An ideal (ultra-stable) clock oscillator can be determined by three fundamental principles. The first is a high and stable oscillation rate. The reason is that a clock operating at a higher frequency has higher precision because of large number of clock "ticks" for the measured time. Secondly, it should be insensitive to external influence, isolated from

any environmental distribution. The last criteria are applicable for any standards, time included. A base unit should be realisable anywhere and anytime, and it should be as close as possible to a definition. Simply said, anyone can build his own clock, and that clock will be as precise as his neighbours. And indeed, using an atom as an oscillator can get us very close to meeting those requirements. This led to a redefinition of the second in the International System of Unit (SI) in 1967. The second is now defined as a duration of 9 192 631 770 periods of the radiation corresponding to the transition between the two hyperfine energy levels of the ground state of the ^{133}Cs atom [11].

The primary time standard - clock these days works on microwaves. Moving into the optical domain it promised better performances due to higher frequencies. However, the biggest obstacle was how to measure optical frequency directly or how to divide it to 1 Hz frequency, thus a signal with 1 s period. This disadvantage was overcome in 2000 with the introduction of the femtosecond optical frequency comb by John L. Hall and Theodor Hansch [12] (Nobel Prize in physics). The optical frequency comb (OFC) is a gearbox between the radiofrequency domain and optical frequencies and vice versa. Therefore the clock development swiftly moves from the microwave domain into the optical domain, see Fig. 1.1).

1.2 Optical atomic clocks

Two primary approaches could be considered for building the clock as an optical frequency standard. One is a single ion isolated in a radio-frequency trap, and the second neutral atoms are trapped in a magneto-optical trap [13, 14, 10]. Those systems, both placed in the ultra-high vacuum chambers, allow very high isolation of ions or atoms from external disturbances. Frequencies of narrow-band electronic transitions of those isolated ions are thus extremely stable references. Several of those systems have been already build over the years including $Al^+, Hg^{+/2+}, Hg, Sr, Sr^{+/2+}, In^{+/3+}, Mg, Ca, Ca^V, Yb^{+/2+/3+}$ and Yb [15, 16, 17, 18, 19].

Our laboratory aims to build an experimental optical clock with $^{40}Ca^+$ ion [20, 21, 22]. The great technological advantage why use Ca^+, is the availability of the wavelengths needed for ion excitation. They can be easily achieved with relatively well available laser diodes that allow large tuning over the frequencies see Subsec. 1.3 [23, 24]. The majority of lasers are provided by Toptica company. Namely, 422 nm for photo ionisation of a neutral atom. 866 and 397 nm for Doppler cooling and 729 nm and 854 nm for sideband cooling, spectroscopy and electron shelving. More information of this lase-ion interaction can be found in Subsec. 1.3.1 and Subsec. 1.3.2).

The experimental setup is schematically illustrated in Fig. 1.3. We use a linear Paul trap with four blades separated by 1.13 mm and two tips separated by 4.5 mm, providing the radial and axial confinement.

By applying the radio frequency (RF) of 29.8 MHz and power of 4W to the trap electrodes and setting the mean tips voltage to 1200V, we achieve typical secular frequen-
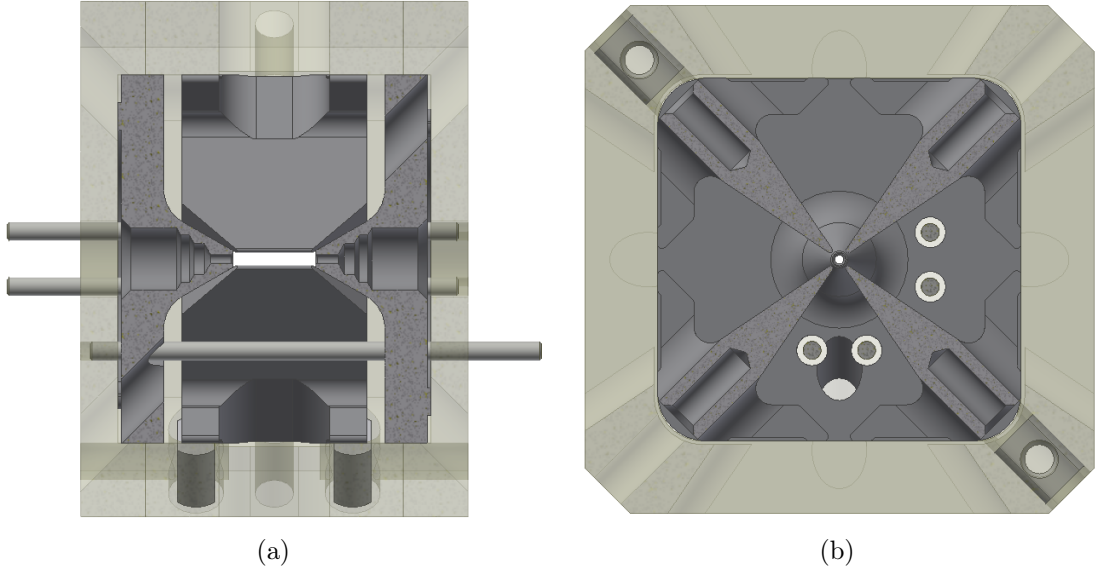
Figure 1.2: Linear Paul trap with four blades and two end-caps electrodes, providing the radial and axial confinement. An axial cross section cut reveal the two end-caps electrodes, a pair of radial electrodes and a compensation electrodes (a). The radial cross section cut show the detail on four radial electrodes symmetrically placed around an end-cup electrode (small hole between the blades) (b).

cies $\omega_r/2\pi = 2.7$ MHz in the radial and $\omega_a/2\pi = 1.1$ MHz in the axial direction. The single Ca^+ ions are loaded into a trap by photo-ionising a beam of neutral calcium atoms. Everything enclosed by an ultrahigh vacuum $< 10^{-11}$ mbar [25], sufficient isolation from the environment perturbation. The trap apparatus is then situated inside a passive magnetic shield box to suppress the magnetic perturbation during the experiment [26, 27, 28, 29]. In the trap, we can hold either one single ion or an enormous Coulomb crystal consisting of tens of thousands of ions.

1.3   Laser-ion interactions

Energy level scheme of $^{40}Ca^+$

Calcium, proved by many laboratories, is one of the most suitable elements for ion trapping and laser cooling [30, 31, 32]. Natural calcium is a mixture of the 5 isotopes $(^{40}Ca,^{42}Ca,^{43}Ca,^{44}Ca$ and $^{46}Ca)$. The most common isotope of the calcium is ^{40}Ca, which comprises 96,9% of all-natural calcium. It is the heaviest stable nuclide with equal proton and neutron numbers. Implementing the Calcium isotope as a stable reference has many advantages. Foremost all the relevant transitions are accessible by a solid-state laser source. The Fir. 1.5 shows the five lowest energy level.

Table 1.1 shows the transition rates and a corresponded wavelength for each transition. One can choose a favourable transition for Doppler cooling, resolved sideband cooling
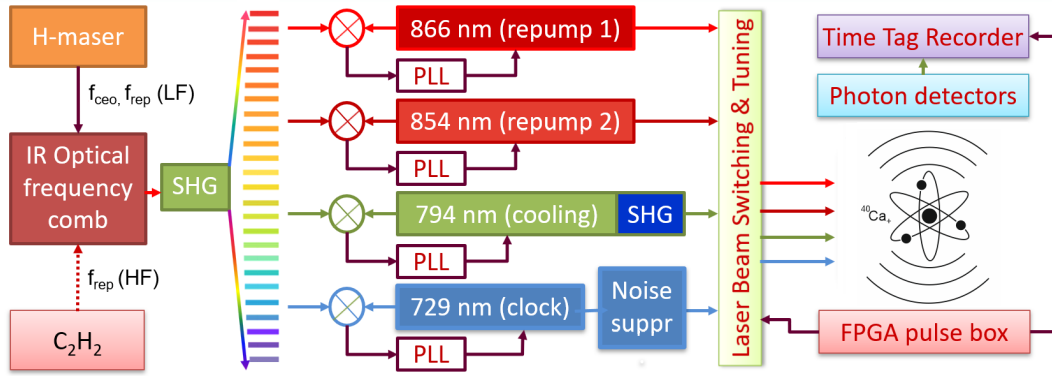
Figure 1.3: A schematic view over the electro-optical setup, including a frequency stabilisation of the lasers for cooling and integration of the $^{40}Ca^+$ ion, The fluorescence of the ion is collected by a single photon avalanche detector. H-Maser: Hydrogen maser, SHG: Second harmonic generation, PLL: Phase loop lock, FPGA pulse box: Lase switching and frequency control based on Field Programmable Gate Arrays.

| (a) | (b) |
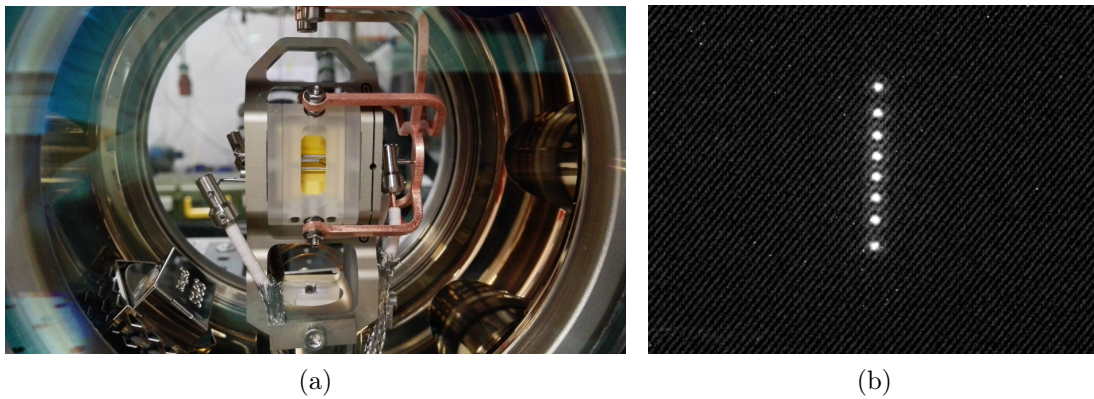
Figure 1.4: A detailed view of the linear Paul trap with gold plated electrodes (a). A fluorescence from the Coulomb crystal made of 8 Ca ions. Ions are trapped and cooled to a temperature near absolute zero by interrogating with cooling lasers (b).

or coherent manipulation of qubits.

The electric quadrupole transition of $^{40}Ca^+$

Compared to a dipole allowed transition which typically decay on ns [23], The $4^2S \leftrightarrow 3^2D$ transitions are the dipole-forbidden transitions with rather long lifetime (> 1 s). The natural linewidth of the transition is an inverse of the lifetime. Thus the linewidth of the transition is 1 Hz approx and less. This makes those transitions an ideal candidates for precision spectroscopy and optical atomic clock.

The $^{40}Ca^+$ clock transition is driven by a laser working on wavelength 729 nm. If the ion is placed inside a static magnetic field of a few Gauss, the Zeeman effect induced
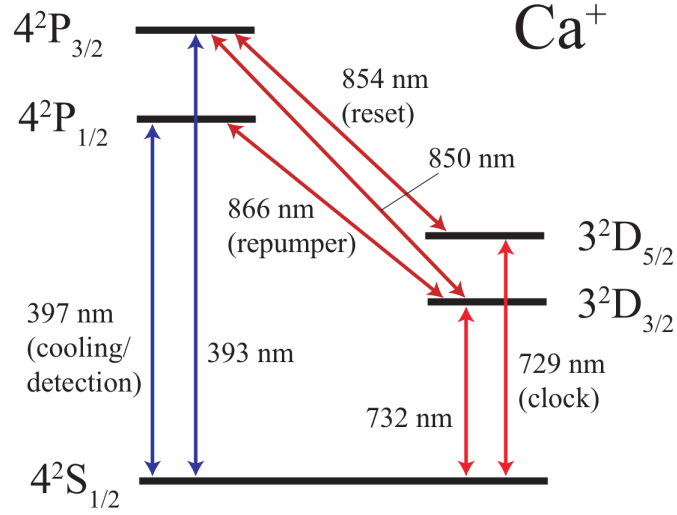
Figure 1.5: Level scheme of $^{40}Ca^+$. The $S \leftrightarrow P$ transition is used for Doppler cooling, while the $S \leftrightarrow D$ transition is used for quantum operations.

Table 1.1: **Transition wavelength and lifetimes of $^{40}Ca^+$ [33].**

		$S_{1/2} \leftrightarrow P_{1/2}$	$S_{1/2} \leftrightarrow P_{3/2}$	$S_{1/2} \leftrightarrow D_{3/2}$	$P_{3/2} \leftrightarrow D_{3/2}$	$P_{3/2} \leftrightarrow D_{5/2}$
τ_{nat}	ns	7,7(2)	7,4(3)	94,3	901	101
λ_{air}	nm	396:847	393,366	866,214	849,802	854,209

		$S_{1/2} \leftrightarrow D_{5/2}$	$S_{1/2} \leftrightarrow D_{3/2}$
τ_{nat}	s	1.045	1.080
λ_{air}	nm	396:847	393,366

Table 1.2: **Branching ratios of the P levels [24].**

$\frac{P_{1/2} \rightarrow S_{1/2}}{P_{1/2} \rightarrow D_{3/2}}$	$\frac{P_{3/2} \rightarrow S_{1/2}}{P_{3/2} \rightarrow D_{3/2}}$	$\frac{P_{3/2} \rightarrow S_{1/2}}{P_{3/2} \rightarrow D_{5/2}}$
15,88	150,8	17,6

14

by this field defining by the quantization axis and by the electric quadrupole shift splits the $4^2S_{1/2} \leftrightarrow 3^2D_{5/2}$ into ten components. There are possible six transitions available for absolute frequency measurement i.e. the clock laser is locked to the $S - D$ transition. They are shown in the Fig. 1.6.
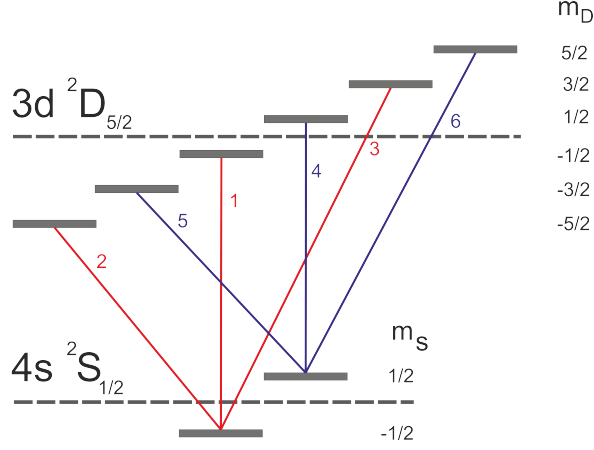
Figure 1.6: Level scheme of $4^2S_{1/2} \leftrightarrow 3^2D_{5/2}$ transition when the $^{40}Ca^+$ is place in the static magnetic field. There are six possible transition for an absolute frequency measurement.

The corresponding frequencies of these transitions are defined as a frequency difference between the magnetic sub-levels of the ground m_S and excited state m_D. They are expressed as follow:

$$
\begin{aligned}
f_1 &= \frac{1}{h}(E_D(\mid m_D = -1/2\rangle) - E_s(\mid m_S = -1/2\rangle)), \\
f_2 &= \frac{1}{h}(E_D(\mid m_D = -5/2\rangle) - E_s(\mid m_S = -1/2\rangle)), \\
f_3 &= \frac{1}{h}(E_D(\mid m_D = +3/2\rangle) - E_s(\mid m_S = -1/2\rangle)), \\
f_4 &= \frac{1}{h}(E_D(\mid m_D = +1/2\rangle) - E_s(\mid m_S = +1/2\rangle)), \\
f_5 &= \frac{1}{h}(E_D(\mid m_D = -1/2\rangle) - E_s(\mid m_S = +1/2\rangle)), \\
f_6 &= \frac{1}{h}(E_D(\mid m_D = +5/2\rangle) - E_s(\mid m_S = +1/2\rangle)).
\end{aligned}
\tag{1.1}
$$

For more convenient way we name a transitions by their magnetic sub-levels differences. So $|^2S_{1/2}, m = -1/2\rangle \leftrightarrow |^2D_{5/2}, m = -1/2\rangle$ as a $\Delta_m = 0$, $|^2S_{1/2}, m = -1/2\rangle \leftrightarrow |^2D_{5/2}, m = -5/2\rangle$ as a $\Delta_m = -2$, etc.

By adjusting the polarisation of the circularly polarised light (397 nm sigma beam) and the polarisation of the 729 laser to relative to the magnetic field, one can alternate the

coupling strength on these transitions. We then select the transition suitable for resolved sideband cooling and the transition for precise transition frequency measurement.

1.3.1 Doppler cooling

Ion trapped inside the RF trap typically has a temperature of several hundred up to a thousand Kelvin. In this regime, the energy levels of the ion are mainly influenced by Doppler effects caused by the ion kinetic energy. The motion of the ion is the superposition of two types of motion. An excessive micromotion comes from an oscillating RF trap drive. The secular motion is given by DC voltages applied to endcap electrodes providing the axial confinement and RF trap potential on quadrupole electrodes. If we want to measure ion's transition frequencies more accurately, those motions need to be cooled down to motianal ground state.

When operating in the so-called Lamb-Dicke regime, the uncertainty of systematic shifts such as second-order Doppler shift is vastly reduced. A Lamb-Dick regime (or Lamb-Dicke limit [34]) is a quantum regime in which the coupling between the ion internal qubit states and its motional states is sufficiently small so that transitions that change the motional quantum number by more than one are strongly suppressed. In order to cool the ion down, it is necessary to reduce its kinetic energy. This cooling process is called Doppler cooling [35, 36].

The table 1.1 indicates that the $S_{1/2} \leftrightarrow P_{1/2}$ transition is the most suitable for Doppler cooling of the Ca^+ ion. As it has a very short lifetime, the cooling process can be repeated many times over this period. As the $S_{1/2}$ level decays with a probability of 6% to metastable $D_{3/2}$ level, the optical pumping has to be prevented. This is achieved by simultaneously exciting the $S_{1/2} \leftrightarrow P_{1/2}$ and $D_{3/2} \leftrightarrow P_{1/2}$ transitions. Both lasers, i.e. cooling (397 nm) and repumper (866 nm) are phase-locked to frequency optical comb for more precise tuning. During the cooling process, the frequency of the repumping laser is kept on the resonance while the frequency of the laser at 397 nm is slightly red detuned. Due to the Doppler effect, atoms will always absorb more photons from the laser beam that is moving towards to. Each absorption event causes the atom to lose a momentum equal to the photon's momentum.

Due to the favourable branching ratio, the ion is cooled on the $S_{1/2} \leftrightarrow P_{1/2}$ transition while the influence of the $D_{3/2} \leftrightarrow P_{1/2}$ transition is small. Therefore, the cooling limit is expected to be close to the Doppler cooling limit of a two-level atom. Yielding a mean vibrational quantum number of $\bar{n} = 10$ for a trap frequency of 1 MHz [5]. The reachable ions temperature is then usually is in hundreds of micro kelvin. In order to cool the ion into the pure state of motion, one needs an additional cooling step. More details about this technique is presented in Subsec. 1.3.2

1.3.2 Sideband cooling

For the secular frequency of about 1 MHz, the Doppler cooling limit results in an average vibrational quantum number of about $\bar{n}$=10 [37]. Thus a second cooling step is necessary to initialise the ion into the motional ground state. This step is realised by sideband cooling technique with a 729 nm laser driving the $S_{1/2} \leftrightarrow D_{5/2}$t transition. When the laser is tuned to the red sideband from the carrier, the ion is transferred to the $D_{5/2}$ level and simultaneously the motional quantum number n is reduced by one [38, 39, 40, 41, 42].

Due to the long natural lifetime of this level, for an efficient cooling process, the ion in $D_{5/2}$ level is coupled to the fast decaying $P_{3/2}$ transition by an 854 nm laser. From the $P_{3/2}$ level, it then, by emitting a photon, decays spontaneously back into the $S_{1/2}$, see Fig. 1.7. In this very simple description, the possibility of the ion decaying into the $D_{3/2}$ instead of the $S_{1/2}$ level has been neglected. If this happens, the ion is repumped by the 866 nm laser. However, now a decay into the wrong $S_{1/2}$ state is possible, and the cycle is not closed (see Fig. 1.7). The result of the cooling process can be seen as a ratio of the blue and the red sidebands.

Figure 1.7: Sideband cooling in $^{40}Ca^+$. A 729 nm laser transfers ion from the $S_{1/2}$ to the $D_{5/2}$ energy state. This results in reducing the motional quantum number n by one. A 854 nm laser then transfers the ion to the $P_{3/2}$ which has short natural lifetime. From there it quickly decays to ground state.

1.3.3 Electron shelving technique

At the end of every experiment, the final quantum state of the atom is read out with Avalanche photodiode (APD). The electron shelving technique allows us to differentiate the occupation of the ion's transition [38, 43, 39]. The efficiency of this process is close to 100%. When the ion occupies the metastable state $D_{5/2}$ it is not addressed by the laser-cooling wavelength and thus will not be able to absorb the light. The fluorescence is

not visible until it decays into $S1/2$ state. The $D5/2$ state occupation can be determined as we repeatably drive the atomic state and measure the fluorescence on the $S1/2 \leftrightarrow P_{1/2}$ transition. The resulting photon count distribution and the appropriate atomic level for this method are shown in Fig. 1.8. The left peak corresponds to the ion being in the non-fluorescence state, while the right peak corresponds to the ion being in the fluorescing state. Both peaks have a Poissonian distribution. Using the threshold, one can discriminate between the S and the D level with an error rate as low as 0.1%.
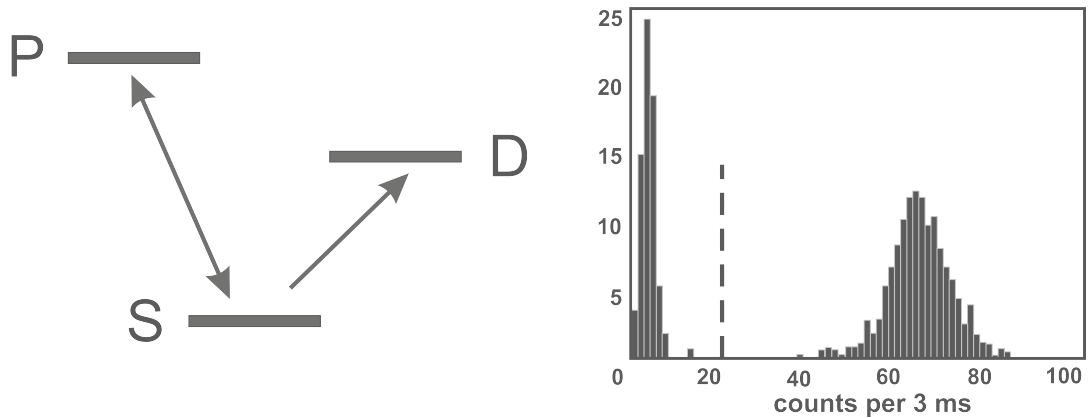

Figure 1.8: Energy level scheme with involved transitions for electron shelving technique (left), distribution of count rate for detection time 3 ms (right). Count numbers smaller then threshold (dashed line) is evaluated as ion being in non-fluorescing D state.

2. Spectroscopy laser

The spectroscopy laser, also called a clock laser, is chosen for the excitation of a transition between two narrow fine energy levels of an atom. As was already mentioned in Chap. 1, our research group selected $^{40}Ca^+$ as a qubit for our experiments. The chosen transition is the electronic quadrupole from $S_{1/2}$ to $D_{5/2}$ level. The corresponding laser wavelength needed to probe this transition is around 729 nm. The natural linewidth of this transition is given by the inverse of the lifetime. So the long lifetime of the states makes these transitions an ideal candidate for high-resolution spectroscopy [44] and for the realisation of an optical clock. For these purposes, the interrogation clock laser must have the spectral line width at the Hz or sub-Hz level.

The most common operation of the spectroscopy laser are:

- high-resolution spectroscopy of narrow transitions,

- resolved sideband cooling of the ion motion,

- detection of the state by electron shelving technique,

- measuring the heating rate of the system using the Rabi spectroscopy,

- measuring the qubit coherence using the Ramsey spectroscopy,

- measuring the stability of the $^{40}Ca^+$ clock.

2.1 External cavity diode laser

In general, there are available three kinds of lasers that work at the wavelength range of 729 nm. They are dye lasers, optically pumped solid-state lasers and semiconductor lasers. A very promising was the optically pumped Ti:Sapphire solid-state laser, which can reach the linewidth at about 25 kHz [45]. Furthermore, it has a very low noise floor close to the emission line. Nevertheless, the laser needs external optical pumping, which carries an additional laser source and thus a requirement for the optical table space. Dye lasers also have external optical pumping, but they also have a poisonous operation due to the toxicity of dye's active matter [46, 47]. The semiconductor lasers come with a compact size, wide tuning range, and high power. A special types of diode laser are external-cavity diode lasers (ECDL) [48]. Compared with a standard laser diode, the ECDL has a longer cavity that increases the damping time of the intracavity light and thus allows for lower phase noise and a smaller emission linewidth (in single-frequency operation). A further reduction of the linewidth can be achieved by placing an intracavity filter such as the diffraction grating. Typical linewidths of an ECDL are below 1 MHz. One of these robust and reliable external cavity diode lasers is a model TA-Pro (Toptica) [49] hereafter as an L729.

2.2 The spectral characterisation of the L729 laser

The critical behaviour of the spectroscopy laser is the spectral linewidth below 1 Hz with the noise background at the level < 50 dB. The first step is then to characterise the spectral properties of the L729. One traditional method for the laser spectral linewidth measurement is a beat-note measurement of the laser through optical mixing against a frequency-stable ultra-narrow linewidth laser. Unfortunately, in our case, we do not have another stable reference laser with l Hz linewidth at the non-traditional wavelength of 729 nm. However, we have an optical frequency comb FC1500 (Menlosystems GmbH) that generates the optical spectrum in the near-infrared part of the light spectrum with a doubling unit, so visible part of the spectrum can be reached.

With the arrival of the optical frequency comb comes a new era of optical metrology [50, 51]. To support the importance of the work, the fathers of these techniques, Theodor W. Hänsch and John L. Hall, shared half of the 2005 Nobel Prize in Physics for contributions to the development of laser-based precision spectroscopy, including the optical frequency comb technique.

In optics, the optical frequency comb is a laser source whose spectrum consists of a series o discrete, equally spaced frequency lines. There are several methods to generate ultra-short pulses. Among the most popular ones is with mode-locker laser. Where the lasers produce a series of optical pulses separated in time by the round-trip time of the laser cavity. Another method uses the electro-optic modulator (EOM) to modulate the phase or/and amplitude of the continuous-wave laser [52]. The optical frequency comb is, in this case, centred around the optical frequency of the continuous-wave laser and an external radio-frequency source provides the modulation. In this configuration, one can set both degrees of freedom of the comb independently [50]. Either way, each pulse is formed as a coherent superposition of numerous equally spaced optical frequencies. Those narrow spectral components are separated by a repetition frequency f_{rep}, and the spectral shift of the entire frequency comb is called an offset frequency f_{CEO}. With those two frequencies known, the OFC is fully defined, and all the it's frequencies are also known. This feature gives us a powerful tool as one can determine the unknown frequencies by beating them with a OFC.

Based on this idea, I put together a setup where the L729 laser is optically mixed with the output of the optical frequency comb. As a dispersion element, the optical grating has been used as a filter to eliminate unwanted OFC's components before a fast photodiode. The resulted beat-note signal is shown in Fig. 2.1.

The measurement shows that the spectral linewidth of beat-note is around 300 kHz approx for the integration time 1 s while our optical frequency comb has averaged tooth spectral linewidth about 50 kHz. It's clear that L729 contributes to the broad full-width at half maximum (FWHM) of the linewidth and thus it does not fulfil the requirement for the efficient pumping of long-lived forbidden transition ($4^2S_{1/2} \leftrightarrow 3^2D_{5/2}$) of $^{40}Ca^+$ ion. Therefore an implementation of the linewidth narrowing technique for the L729 is necessary. In the following chapter, I will describe several techniques I have used to
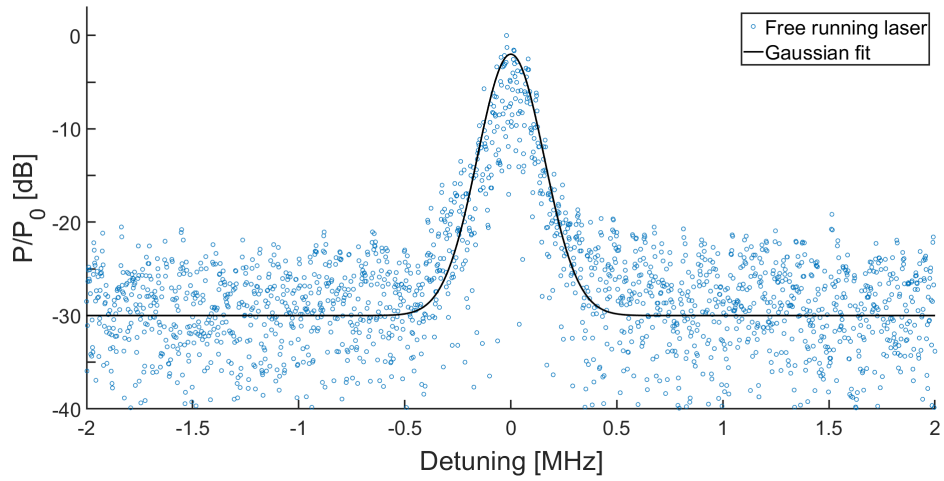
Figure 2.1: A spectral profile of the beat-note of a free running L729 and the optical frequency comb for the integration time 1 s. The laser spectral linewidth is 300 kHz approx.

achieve a laser with a narrow spectral line for high-resolution spectroscopy purposes.

3. Emission line narrowing techniques

High spectral purity and coherence laser source is a crucial feature for many applications, such as atomic physic, high-resolution spectroscopy of trapped ions, coherent manipulation, and communication, to name a few.

This work is dedicated to delivering a laser with an ultra-narrow spectral linewidth for high precision spectroscopy on $^{40}Ca^+$ ion. As mentioned in Chap. 2, to perform spectroscopy on its electric quadrupole transition, one needs a laser with a spectral linewidth at the level of Hz.

The basis of the laser system for high-resolution spectroscopy of $^{40}Ca^+$ cooled ions is the L729, whose spectral line-width is around 300 kHz. Therefore, this laser needs improvement with a technique that reliably ensures the direction of narrowing the broad spectral lines to the 1 Hz level. I have focused on several methods which I theoretically designed and experimentally implemented in my work. The main focused methods are:

- the technique of phase-locking the optical frequency of the laser on a selected tooth of an optical frequency comb,

- narrowing the broad spectral line-width with the help of a fibre interferometer,

- lock the optical frequency of the laser on a selected mode of a high-quality optical cavity,

- transferring the stability from ultra stable source using the transfer oscillator technique.

In following sections I designed and experimentally tested pilot arrangements for the individually mentioned methods. Then I compared achieved results.

3.1   Phase lock to optical frequency comb

The first approach to narrowing the linewidth of the L729 laser is using the phase-locked loop (PLL) t an external narrow-linewidth reference represented by the optical frequency comb. The principle of the method is in phase-locking to the laser optical frequency to a selected component (one tooth) of an optical frequency comb, which has approximately ten times narrower linewidth than the L729. The schematic of the setup related to the method is shown in Fig. 3.1.

A PLL is a feedback system combining a tunable oscillator (the L729 in our case) and a phase comparator, which is usually implemented using an RF mixer. On a photodetector, the input laser is non-linearly mixed with a OFC tooth producing an RF beat note signal. Any changes in the input laser frequency will appear as a change in the phase of this beat note signal. The beat note signal phase is compared to that of an RF reference signal derived from the H-maser. This detected phase shift serves as an error signal for

a cascade of fast and slow P-I-D controllers actuating the laser optical frequency. In the equilibrium state of this control loop, the offset between the laser optical frequency and the nearest comb tooth will be locked to the frequency of the RF reference signal. Provided the bandwidth of the control loop is much higher than the original laser linewidth, the resulting spectral profile of the L729 laser will copy that of the selected optical frequency OFC tooth. The pilot testing setup of the scheme has been performed and can be seen in Fig. 3.1.
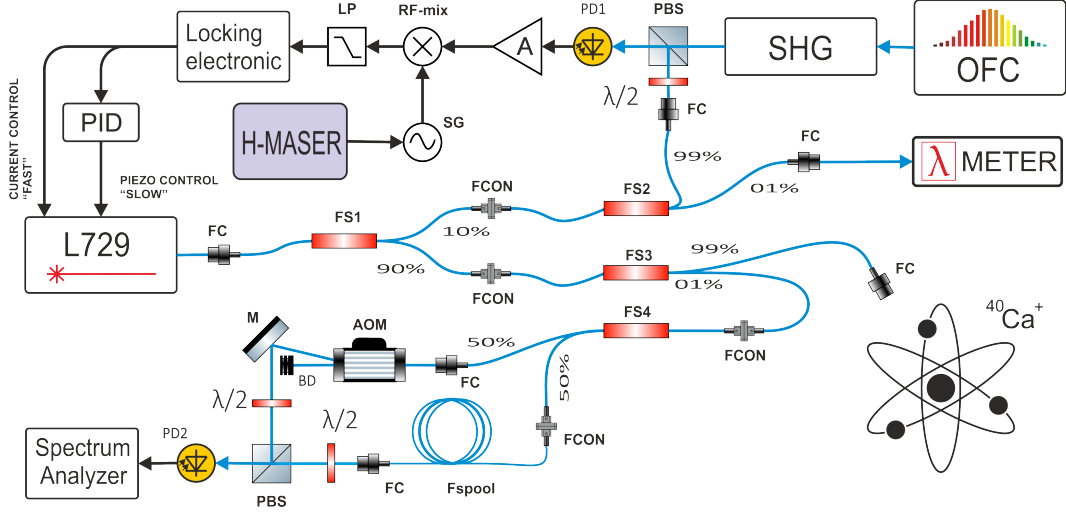

Figure 3.1: The setup with the L729 laser and the phase lock loop chain for locking the optical frequency of the L729 laser to the optical frequency comb. LP: Low-pass filter, RF-mix: Radio frequency mixer, A: Amplifier, PID: Proportional Integral Derivative controller, SG: Signal generator, PD: Photodetector, PBD: Polarizing beam splitter, FC: Fibre collimator, FS: Fibre splitter/coupler, FCON: Fibre connection, M: Mirror, BD: beam dumper, AOM: Acousto-Optic Modulator, $\lambda/2$: Half-wave plate, Fspool: Fibre spool, SHG: Second Harmonic Generation, H-maser: Hydrogen maser, λMETER: high-resolution wavelength meter, OFC: Optical Frequency Comb.

In order to verify the narrowing process of the L729, further characterisation laser frequency noise is necessary. For this purpose, I used an unbalanced Mach-Zehnder interferometer (MZI) in accordance with [53, 54]. This so-called self-heterodyning method determines the relative phase shifts between the two separated beams originating from a single source. The phase difference is induced by differences in the length of the pathways. In our case, a fibre spool delay line is inserted into one of the interferometer arms and an acousto-optics modulator (AOM) is placed in the other arm. The AOM shifts the optical frequency by 80 MHz. The heterodyne detection is accomplished by mixing signals of the laser frequencies propagated in the long and the short arm. The output beam is then focused onto a fast photodetector and analysed by a radiofrequency (RF) spectral analyser. The analysed power spectral density (PSD) of the frequency noise of the L729 laser was measured in the frequency range from 1 Hz to 200 kHz with a resol-
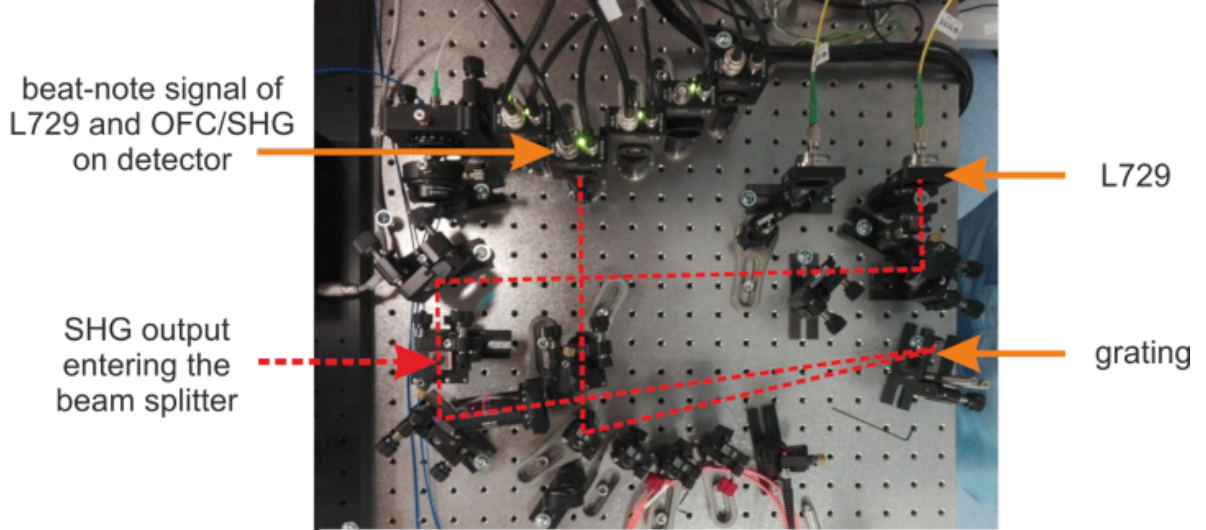
Figure 3.2: The optical setup for the stabilisation the L729 laser by phase loop lock to the optical frequency comb. The L729 is delivered via a polarisation maintaining fibre(the upper right corner). The OFC enters the SHG stage and enters the optical beat-noting setup from the left. Laser beams from L729 and OFC are aligned so that they met at the photodetector.

ution bandwidth of 1 Hz. The data was analysed after averaging 100 sweeps of the RF spectrum analyser. The comparison of the free-running laser and the laser phase locked to one tooth of the optical frequency comb is shown in Fig. 3.3 (power spectral density) and Fig. 3.4 (beat-note spectrum).

As we mentioned above, previous measurements in our laboratory revealed that the individual component (one tooth) of the optical frequency comb has a line width of 50 kHz approx. for 1 s integration time. Thus I expected that implementing the phase lock of an L729 onto the OFC would reduce laser linewidth by a factor of ten approx.. The advantage of this method, besides the line width narrowing, is that the L729 optical frequency is derived from a metrologically traceable time scale thanks to the referencing of the OFC with an active hydrogen maser that can reach a 10^{-15} fractional frequency stability for 10^4 s integration time. For high-resolution spectroscopy, this narrowing factor is still not sufficient. However, it is abundantly used for the rest of the wavelengths that do not require such a pure spectrum profile.

3.2 Stabilization using fibre-spool

The previous realisation of the laser frequency noise analyser based on the MZI with a fibre spool as a frequency discriminator gives an idea that one can use it also to spectral narrowing of the laser frequency directly.

The fibre spool is built using a 500 m long single-mode fibre tightly wound in a helix
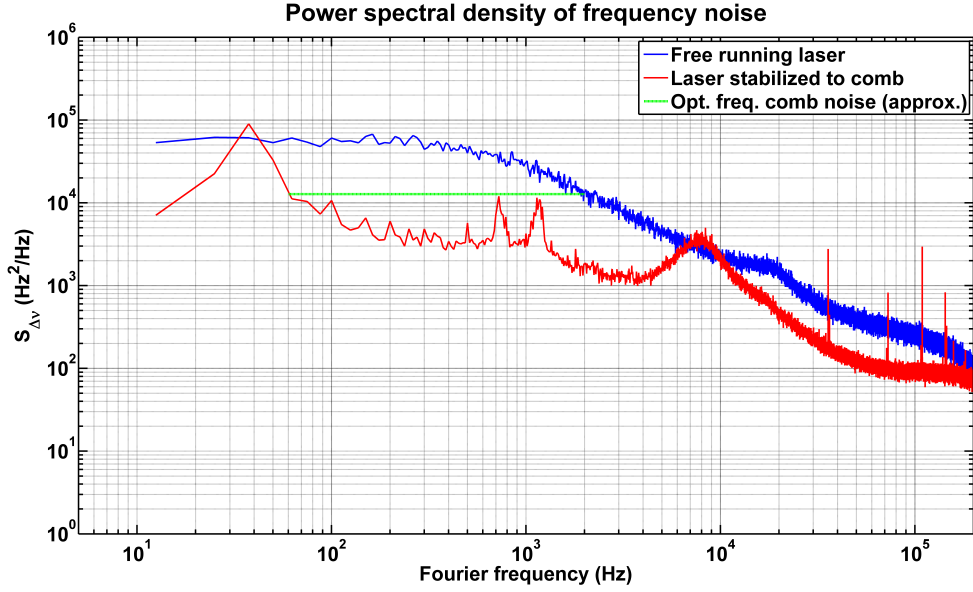
Figure 3.3: The power spectral density of the L729 frequency noise for free-running regime (blue) and for the phase lock to optical frequency comb regime (red). The green line indicates the approx. level of optical frequency comb noises.
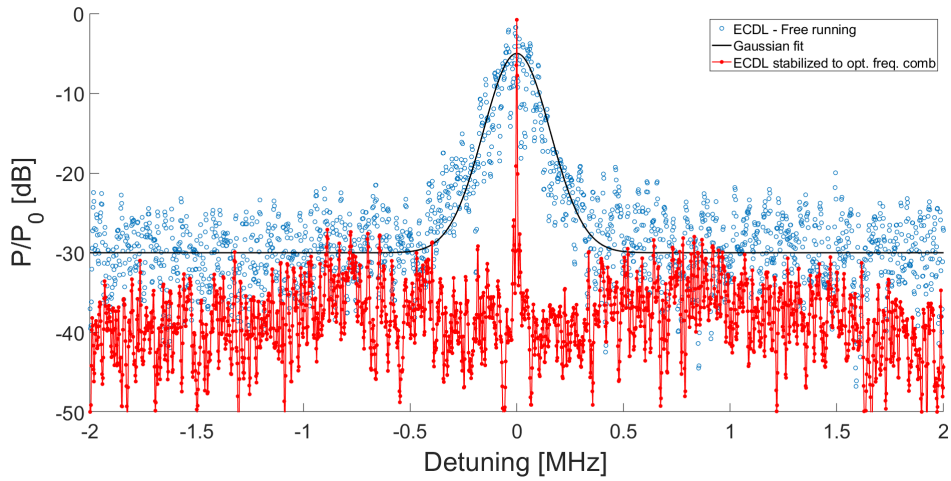
Figure 3.4: Normalized beatnote spectrum of the L729 laser. Comparison of free-running (blue) and phase-locked on the optical frequency comb tooth (red) regime.

form and gives a fixed relative time delay $\tau = 2.45$ μs. The MZI then converts the deviation of the laser optical frequency (ν_{opt}) into phase error (φ_{err}) in the radio frequency domain. The transfer function can be written as

$$\frac{\varphi_{err}(f)}{\nu_{opt}(f)} = \frac{1 - e^{-j2\pi f tau}}{jf} (rad/Hz), \tag{3.1}$$

where τ is the fibre-induced delay. The maximum bandwidth of the laser stabilisation loop is limited by the delay introduced by the fibre spool. Practically the frequency limit is $\approx 1/(2 \cdot \tau)$. In our case, the imbalance arm with 500 m results in a bandwidth limit of ≈ 0.2 MHz. The deviation of 1 Hz from the reference frequency in the optical domain will transfer into an approximately 15 μrad phase signal in the RF domain. If the fibre length is 5000 m, a 1 Hz deviation will convert into 150 μrad, etc. Here one can see that the sensitivity of the frequency discriminator is directly proportional to the length of the fibre spool.

The advantage of this method lies in its simplicity and not requiring any complicated instrumentation. However, it is essential to isolate the fibre from environmental perturbations such as temperature and vibration noises for long-term purposes. A long fibre is susceptible to mechanical stress and thus will induce excess frequency noise in fibre stabilised laser. So one can find himself stabilising not the laser, but the fibre spool as the induced noise from fibre exceeds the laser noise. To overcome this problem, one can build an isolation box around the spool or insert it into a vacuum chamber.

I put together a setup where the L729 linewidth is suppressed by MZI technique. The schematic diagram us shown in Fig. 3.5.In my experiment, the initial optical wave is divided into two separated waves by a 50/50 coupler. One enters the 500 m fibre spool, and the other one is frequency shifted by the AOM that is driven by an RF frequency f_{carr} = 80 MHz. A 50/50 beam splitter then recombines those two waves. This beat-note signal at a carrier frequency carries information about laser frequency noise and environmentally induced phase noise. The detected signal is then amplified and compared with a reference signal provided by H-maser. Depending on the phase difference of these two signals, the controller adjusts the L729 injection current.

I tested the L729 narrowed by MZI technique in the spectroscopy on the $4^2S_{1/2} \leftrightarrow 3^2D_{5/2}$ transition on the single cooled calcium ion. Thus using the primary pulse sequence, including the electron shelving technique, the spectrum of one Zeeman component is obtained (see Fig. 3.6). We can see the carrier of this transition and its secular motional sidebands when the laser was scanned over the spectrum. The spectral linewidth of the laser stabilized by MZI technique is still very broad ($<$50 kHz). For more detailed information on electron shelving, please see Subsec. 1.3.3.

3.3   Transfer oscillator technique

Another stabilisation method is based on using a so-called transfer oscillator technique described in [55, 56]. It allows us to transfer spectral profile of s highly coherent laser from one wavelength to another laser working at a different wavelength. We operate a laser working at 1540.57 nm (L1540) in our department at ISI CAS [57]. The laser L1540 is based on a narrow-linewidth fibre laser Basik1[1], which is phase locked to high-finesse optical cavity. This laser is used for stabilization of the optical frequency comb repetition

---

[1]NKT Koheras Basik.
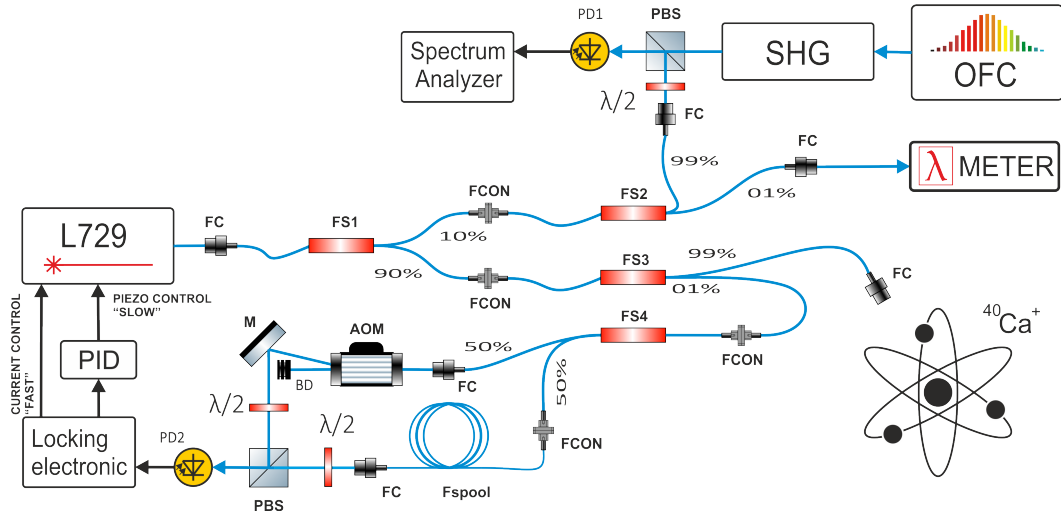
Figure 3.5: The schematic diagram of the stabilisation stage using the Mach-Zehnder interferometer in the servo-loop. PID: Proportional Integral Derivative controller, PD: Photodetector, PBD: Polarizing beamsp litter, FC: Fibre collimator, FS: Fibre splitter/coupler, FCON: Fibre connection, M: Mirror, BD: beam dumper, AOM: Acousto-Optic Modulator, $\lambda/2$: Half-wave plate, Fspool: Fibre spool, SHG: Second Harmonic Generation, λMETER: high-resolution wavelength meter, OFC: Optical Frequency Comb.

Figure 3.6: The captured spectrum of the the $S_{1/2} \rightarrow D_{5/2}$ transition of $^{40}Ca^+$ ion measured with the L729 narrowed by means of the unbalanced fibre-spool Mach-Zehnder interferometer.

frequency. Thanks to advanced synchronization technique where the H-maser plays a role of disciplining oscillator for the OFC, the laser frequency of the L1540 is stable with the

27

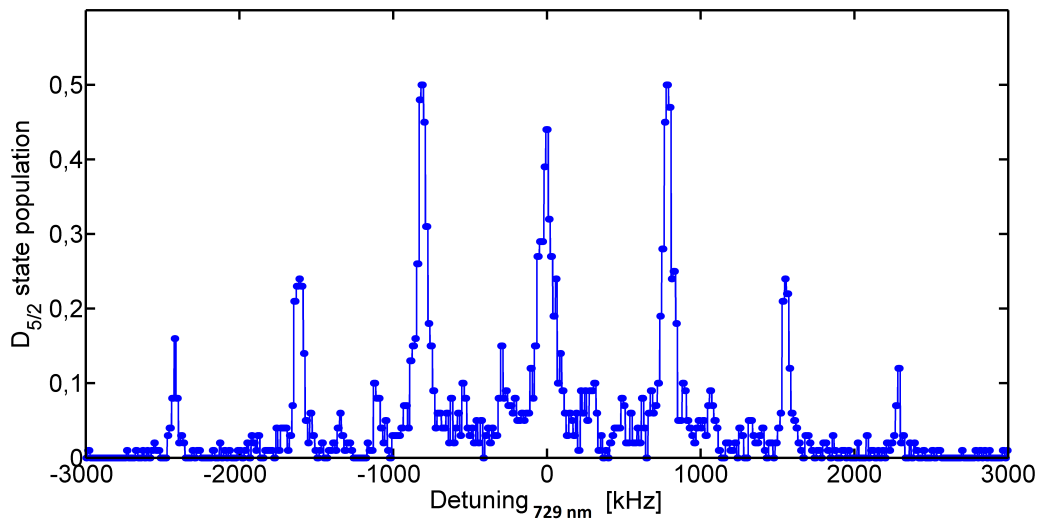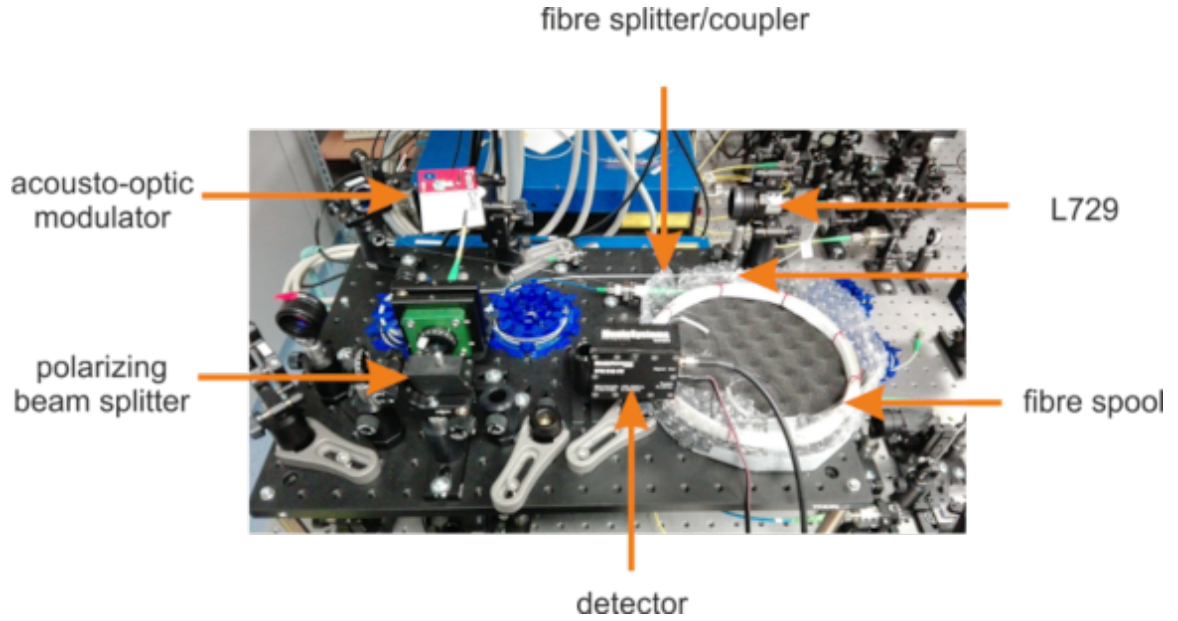Figure 3.7: The optical setup for the stabilisation the L729 laser with unbalanced Mach-Zehnder interferometer. The original wave is separated by an fibre optical splitter. One of them is frequency shifted by an acousto-optic modulator. The second one is delayed by a 500 m long fiber spool. Those two waves are then combined in a polarising beam splitter and detected by a fast photodetector.

same relative stability as the H-maser. I put together a pilot setup where the spectral profile and stability of the L1540 is transferred to spectroscopy L729 with using the OFC.
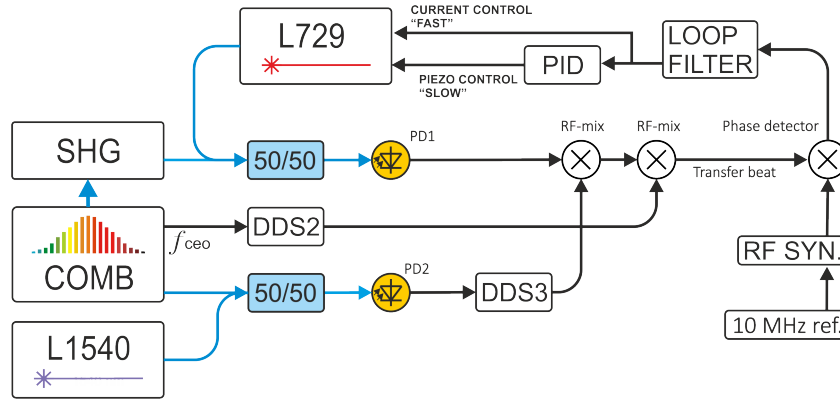
Figure 3.8: Transfer oscillator technique. DDS: Direct Digital Synthesizer, x/y: Fiber Optic Coupler. RF-mix: Radiofrequency mixer, PD: Photodetector. RF SYN: Radiofrequency synthesizer, 10 MHz reference is provided by the H-maser.

First, the L729 and L1540 lasers are individually optically heterodyned with specific teeth of the optical frequency comb, closest to their optical frequencies. We will name indices of those teeth as N_{729} and N_{1540}. Due to the properties of the OFC spectrum

defined as $\nu_k = f_{ceo} + k \cdot f_{rep}$, frequency deviations observed between the $N_{1540}{}^{th}$ tooth and L1540 relate to observed deviations between L729 and the $N_{729}{}^{th}$ tooth. The relationship between L1540 and L729 beat frequency deviation observed at the same time can be expressed as $\Delta\nu_{L729} = \Delta\nu_{L1540} \cdot \frac{N_{729}}{N_{1540}}$. To subtract this frequency noise from the L729 beat, the beat signal of L1540 is frequency multiplied by the ratio of N_{729}/N_{1540} using a direct digital synthesiser (DDS) DDS3 and then mixed with the L729 beat. The technique of frequency multiplication by DDS was thoroughly described in [58]. Since the f_{ceo} lock of the OFC has its bandwidth limited by approx. 9 kHz, there is some non-negligible residual frequency noise originating from the OFC pump laser present at higher Fourier frequencies of the f_{ceo} signal. This frequency noise is present in the L729 beat as well. The f_{ceo} signal from the OFC is thus used for subtracting this frequency noise from the L729 beat note. After frequency multiplying the f_{ceo} signal appropriately by DDS2 and mixing it with the L729 beat as shown in Fig. 3.8, we get the resulting virtual "transfer beat" independent of both f_{rep} and f_{ceo}. Using this beat signal in a phase-locked loop, we can narrow down the L729 laser to a level allowing us to efficiently transfer the qubit population into $|D_{5/2}\rangle$ with a precision <3 kHz, see Fig. 3.9.
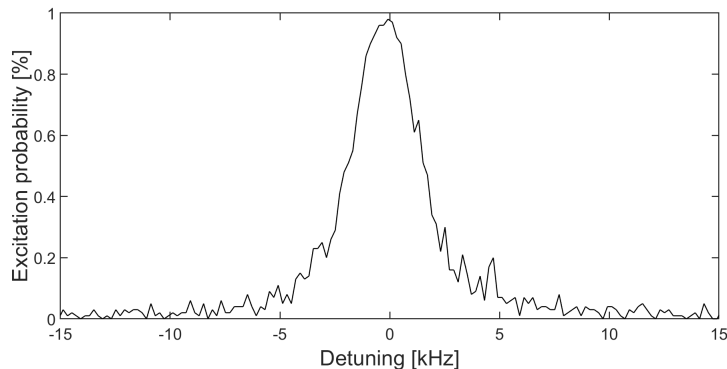
Figure 3.9: Frequency scan over a carrier on a transition $\Delta m = 0$ with the L729 narrowed by the transfer oscillator technique. The spectral linewidth is 3 kHz approx.

The disadvantage of the transfer oscillator technique lies in the complexity of the whole setup with many broadband servo loops that inevitably lead to transferring residual noise from various sources, including complex locking electronics, into the resulting laser. Those residual noises interact with the ion in the form of off-resonance excitation of the transition lines, which reduces the fidelity and degrade the cooling process.

3.4   High finesse optical cavity at 729 nm

A more traditional and, so far, the most implemented method is the phase locking technique based on ultra-stable Fabry-Perot interferometers (FPI), also known as high-finesse (HF) cavities [59]. The optical cavity consists of two highly reflective mirrors optically

contacted to stable spacer [60, 61]. The spacer is usually made from a material that has a very low expansion coefficient, like Ultra-low Expansion glass (ULE®) or a silicon single-crystal [59, 62]. HF-cavities as references are broadly used and already commercialised (Stable Laser Systems)[63]. The important property of these cavities is that their fractional frequency instability of the longitudinal cavity mode directly relates to its fractional length instability. HF cavities can serve as very sensitive frequency discriminators. Using the Pound-Drever-Hall (PDH) [64] detection technique in a servo loop, we can lock a spectroscopy laser wavelength to the HF-cavity length and achieve the laser with Hz or sub-Hz spectral linewidth [62].

Moreover, one can find a relation between the finesse of the optical cavity and the locking process. Effectively it is a number of the bounces a beam must make before leaking out or being absorbed. It is fully determined by the optical cavity losses and is independent of the optical cavity length. The finesse of HF-cavity is usually in the range of 10^5.

The higher the finesse, the higher gain one can achieve in the control loop. The limitation of this technique lies in two aspects. The first is an aging of the optical cavity's spacer which leads to permanent shift of the resonant frequency, thus very low frequency noise. The other aspect is in the Brownian thermo-mechanical noise [65, 66] in the material of mirrors, which directly leads to fluctuations of the optical length of the optical cavity and thus affects the frequency noise of the laser locked to it in broad range of frequencies. Using this method for the spectroscopy laser narrowing and frequency stabilisation, the fractional frequency stability of the laser can reach 10^{-16} level for integration times shorter than 1 s [4].

3.4.1 Optical cavity principle of operation

The optical cavity is an arrangement of mirrors which allows light to form a standing wave called an optical cavity modes at specific resonant frequencies. There are many types of optical cavities available with a different arrangements of the mirrors. Each one of them has some pros and cons. The most common type is hemiconfocal optical cavity. It's arrangement consists of a plan-parallel (PPM) and a plan-concave mirror (PCM), Fig. 3.10.

An incoming Gaussian beam enters the optical cavity via a PPM. With correct conditions, in terms of spatial light incoupling and frequency constraints, it can be matched into this optical cavity's fundamental mode (TEM_{00}). Since the physical parameters of the optical cavity is fixed, the only adjustable parameters are the position and size of the beam waist of the incoming beam. Thanks to the asymmetric arrangement of the mirrors, we can place the beam waist at the position of the planar mirror. Furthermore, by adjusting the horizontal and vertical position of the incident beam, one can ensure the right matching of the spatial model of the laser to that of the optical cavity [67]. The beam waist can be calculated as follows:
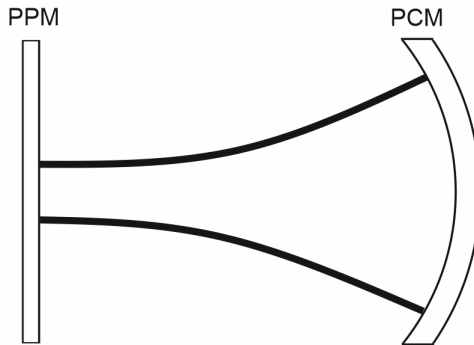
Figure 3.10: The hemiconfocal optical cavity with a plan-parallel mirror on one side and a plan-concave mirror on the other side. Here $R_{PPM} = \infty$ and $R_{PCM} = 500$ mm.

$$\omega_0^4 = \frac{\lambda^2}{\pi^2}(R - L)(L).\qquad(3.2)$$

Where R is the radius of a PCM and simultaneously the radius of curvature of Gaussian beam at the position L. The second condition requires the beam phase to reproduce itself after a competed round trip. That means that the Gaussian beam inside the optical cavity has to be restricted to certain resonance frequencies.

If all the requirement are met, the laser light resonate inside the optical cavity in the form of Hermite–Gaussian modes [68][67]. The simplest of those are the Gaussian modes, where the field distribution is defined by a Gaussian function. The intensity distribution of such a mode has n nodes in the horizontal direction and m nodes in the vertical direction. For $n = m = 0$, the mode is called the fundamental mode or axial mode TEM_{00}. It has the simplest intensity profile and thus has the highest beam quality. Other modes are called higher-order transversal modes and have a more compacted intensity profile. The axial modes spacing (between two TEM_{00} modes) is called a Free Spectral Range (FSR) and is defined as

$$\nu_{FRS} = \frac{c}{2nL}.\qquad(3.3)$$

Where n is the refractive index of the optical cavity. We can adjust the coupling into the optical cavity so that the distribution of the intensity into higher-order modes is negligible to the intensity of the TEM_{00}. By placing the sensitive photodetector after the optical cavity, we can directly observe the spectral profile of the mode. And the linewidth of the mode is defined as the full width at half maximum ($FWHM$) of the transmission peaks,

$$\delta_\nu = \frac{\nu_{FSR}}{\mathcal{F}}.\qquad(3.4)$$

Where $\mathcal{F}$ is finesse of the optical cavity. One can see that the higher the finesse, the narrower the spectrum of the transmitted spectra. Thus the better quality of the optical

cavity. A laser is typically locked to a TEM_{00} mode of the optical cavity. Thus only stepwise changes of the laser frequency by one FSR are possible.

When the light with a wavelength λ, is sent to the optical cavity and reaches the first mirror, it is partially reflected and partially transmitted. The transmitted light then travels inside the optical cavity until it reaches the second mirror, where it splits into reflected and transmitted parts again (Fig. 3.11). These transmitted and the reflected fields are then given by

$$t = \frac{E_t}{E_i} \quad and \quad r = \frac{E_r}{E_i}. \tag{3.5}$$
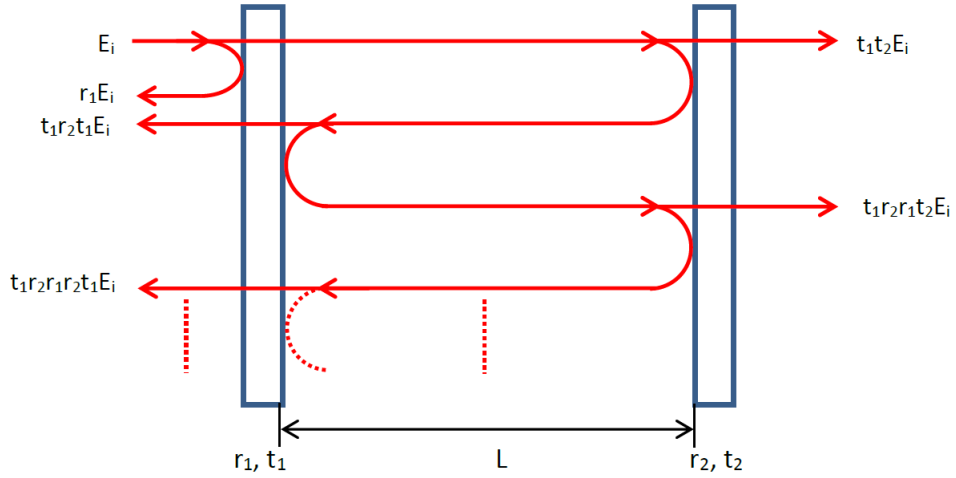
Figure 3.11: Multiple-beam interference of reflected and transmitted light in the optical cavity (for this example, it is simplified to the optical cavity arrangemenr with two PPMs).

With $E_i = E_0 e^{iwt}$ being the electric field amplitude of the incident light wave, r the reflection coefficient and t the transmission coefficient. Here r and t relates to each other as:

$$r^2 + t^2 = 1 \quad and \quad 0 \leq r, t \leq 1, \tag{3.6}$$

where $r^2 = R$ is the reflectivity and $t^2 = T$ is transmission of a mirror. For simplicity, the absorption in the mirrors is not considered.

When calculating the reflection coefficient of the optical cavity, one has to take into account the phase φ that the light accumulates during the time T_φ while bouncing from one mirror to the other and back again. Furthermore, the π phase shift of the light as it is reflected at the first mirror has to be also taking into account. The phase φ can be expressed as

$$\varphi = \omega T_\varphi = 2\pi \frac{2L}{\lambda}. \tag{3.7}$$

So a factor of $e^{i\varphi}$ has to be added for every roundtrip of the light. The total reflected field for the optical cavity without losses is then given by:

$$E_r = E_i(-r_1 + t_1 r_2 t_1 e^{i\varphi} + t_1 r_2 r_1 r_2 t_1 e^{2\varphi} + ...) = E_i(-r_1 + \frac{t_1^2 r_2 e^{i\varphi}}{1 - r_1 r_2 e^{i\varphi}}). \quad (3.8)$$

In case of a symmetric optical cavity, $t1 = t2, r1 = r2$ this equation is reduced to

$$E_r = E_i r \frac{e^{i\varphi} - 1}{1 - r^2 e^{i\varphi}}. \quad (3.9)$$

This term is important to derivering the Pound-Drever-Hall locking signal. The principle of this laser frequency stabilising method is described in [64]. The reflected and transmitted intensities of a symmetric lossless optical cavity are:

$$I_r = I_0 \frac{4R sin^2 \frac{\varphi}{2}}{T^2 + 4R sin^2 \frac{\varphi}{2}}, \quad (3.10)$$

$$I_t = I_0 \frac{T2}{T^2 + 4R sin^2 \frac{\varphi}{2}}. \quad (3.11)$$

As was aforementioned, the finesse of an optical cavity is effectively the number of bounces a beam makes before it leaks out or is absorbed. Thus the finesse is directly related to the reflectivity of the mirrors [11]. Assume the situation that the laser is suddenly switched off. The light in the optical cavity will still exist (accumulated) due to the high reflection of mirrors. But each time the beam interacts with the mirror, it loses a certain % amount of its power due to transmission. The quality of the optical cavity (i.e. of its high-reflective coatings on the mirrors) can thus be defined by its losses.

$$\alpha_r = \alpha_s + \alpha_{m1} + \alpha_{m2}. \quad (3.12)$$

Where α_s is loss due to internal scattering and $\alpha_{m1} + \alpha_{m2}$ are contribution of mirror losses that are defined as:

$$\alpha_m = \frac{1}{2L} ln \frac{1}{r}, \quad (3.13)$$

Where r is reflectivity of mirror. Finesse of the optical cavity is then defined as:

$$\mathcal{F} \approx \frac{\pi}{\alpha_r} = 2\pi \tau_p \nu_{FSR}, \quad (3.14)$$

where τ_p is mean lifetime of photons in the optical cavity.

$$\tau_p = \frac{1}{\alpha_r C}. \quad (3.15)$$

Or one could find mean lifetime of photons τ_p related to linewidth could be calculated as

$$\tau_p = \frac{1}{2\pi \delta_\nu}. \quad (3.16)$$

This widely used technique is called cavity ring-down spectroscopy (CRDS). We can precisely determine its finesse by measuring the exponentially decaying light intensity leaking from the optical cavity.

3.4.2   Pound-Drever-Hall method

The optical cavity responds to the laser frequency change and can be detect in the form of transmitted and reflected light, which can be used to produce the error signal for the servo. The simplest way is to lock the laser frequency into one side of the fringe (known as side-looking). As the slope of the fringe is very steep, just a slight change in laser frequency will produce a strong cavity response. Unfortunately, with this method, one cannot distinguish between the laser frequency and the intensity fluctuation. Also, as a modulation-free technique, the signal is detected at DC, which can contain a significant amplitude $1/f$ noise.

With the Pound-Drevel-Hall (PDH) stabilisation technique, we can avoid most drawbacks by modulating the laser phase at a high frequency. The error signal is thus detected at frequency, where the technical noise is very weak and thus total noise is near the shot-noise limit [69]. The phase-modulated signal consists of a carrier and two sidebands. One at the higher frequency $(f_{carr}+\Omega)$, with a phase relative to the carrier, is in phase with the modulation, while the one at a lower frequency $(f_{carr}-\Omega)$ is out of phase by 180°. Thanks to this odd symmetry about the optical cavity line centre, we can lock the frequency to the optical cavity resonance peak.
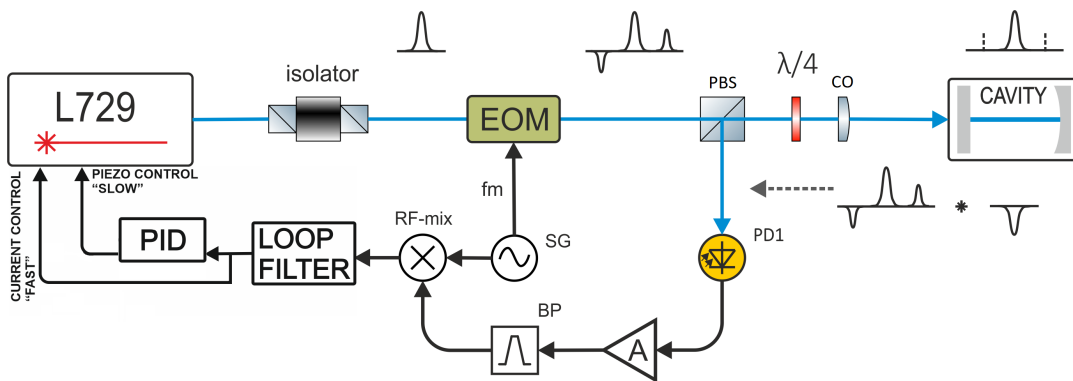
Figure 3.12: Scheme of the PDH locking technique. Isolator: Faraday isolator, EOM: Electro-optic modulator, PBS: Polarizin beam splitter, SG: Signal generator, BP: Band-pass filter, A: Amplifier, CO: Collimation optics, PID: Proportional Integral Derivative controller, fm: modulation frequency.

The Fig. 3.12, shows the basic setup for PDH locking technique. The laser beam from the L729 is firstly sent through an optical isolator to avoid the back reflection of the laser to the laser diode. The laser beam is then phase modulated EOM and coupled into the optical cavity via the polarising beam-splitter and the quarter-waveplate. The reflected beam from the optical cavity is sent back through the quarter-waveplate and the beam-splitter into the avalanche photodetector.

The detected beat-note signal is a nonlinear mixing of reflected spectra multiplied by a complex function of the optical cavity reflection coefficient. The phase and the

amplitude of this signal, at frequency f_m, depends on the laser detuning from the optical cavity mode.

The photodetector will respond as follows. If there is no phase shift of the carrier or modulation sidebands with respect to one another, there will be no response signal at the modulation frequency. The reason is that a beating signal of the carrier and the upper sideband will create a photocurrent modulation that is exactly cancelled by the out-of-phase modulation from the lower frequency side. If on the other hand, the carrier's phase is shifted or the sidebands are phase-shifted, there will be a response at the modulation frequency.

The phase-sensitive demodulation of this signal against the RF reference (driving the modulator crystal and thus providing the frequency offset between the carrier and phase modulation sidebands) converts the symmetric minimum in the optical cavity reflection coefficient into the desired antisymmetric frequency discriminator curve (better known as PDH error signal). The locking point is the zero in the central high-slope region of this curve. The steepness of this slope, thus the sensitivity to the fractional optical frequency change, is inversely proportional to the linewidth of the optical cavity mode.

The error signal leads to a fast analogue controller, which steers the frequency of the laser at the front of the high-finesse optical cavity setup. To reduce the laser linewidth effectively, such a control loop's bandwidth needs to be approximately two times higher than the initial spectral linewidth of the laser.

This technique is described in more details in [64, 70, 71, 72].

4. Experimental setup

After a thorough investigation and implementation of various frequency stabilisation techniques, I considered the limitations of each technique. The result of implementation concludes that the best technique (in both short-term and long-term points) is to optically stabilise the L729 by locking its frequency to the ultra-stable HF-cavity (ULE C729) and providing additional control for keeping the aging effect of the C729 spacer at a very low level.

4.1 Optical setup

This section aims to present my final optical assembly that is currently used at the Institute of Scientific Instruments - ion setup. The assembly is used 24/7 for high spectroscopy on trapped and laser-cooled calcium ions for carrying out many experiments from metrology, quantum optics and mechanics. I carefully selected the best aspects out of all the methods described in the Subsec. 3 and embedded them in one single optical setup. The scheme of the whole optical setup is shown in the Fig. 4.1.

The setup can be divided into two main blocks. One with the implemented the C729 and its optical requirement for the locking process. The second one is for producing the Ttransfer beat signal, which compensates for the C729 drift. A small portion of the light is firstly coupled and transported to the wavelength meter and the beating stage with the OFC. The main laser beam enters the setup with a single pass AOM for intensity stabilisation. The rest of the optical setup in the vicinity of the L729 is for frequency preparation before entering the chamber with cold $^{40}Ca^+$ ion.

4.1.1 Diode laser and fibres

The laser used for the experiment (L729) is a model TA-Pro[1]. TA-Pro series consists of a laser diode chip with one end being anti-reflection coated. The laser cavity is completed with a collimation lens and a mirror. This External-cavity diode laser is equipped with a tape amplifier (TA) which allows for high power (400 mW) at a wavelength of 729 nm. An intracavity diffraction grating provides a sufficiently wide coarse tuning of several nm. The correctly set laser typically provides approx. 20 GHz mode-hop free tuning range.

To transport a laser light into many stages, we use polarisation maintaining fibres[2]. The stabilisation stage with C729 is connected via 10 m long fibre, the beating stage with an optical frequency comb, 3 m long fibre and the ion setup 10 m long fibre.

The fibre itself induces the noise into the laser light by Doppler effect. Thus the connection path with C729 is equipped with fiber cancellation (FNC). In the future, we plan to integrate this technique also on the rest of the long fibre connection.

---

[1]TA-Pro, Toptica, Germany [49].
[2]Thorlabs, panda style PM-fiber.
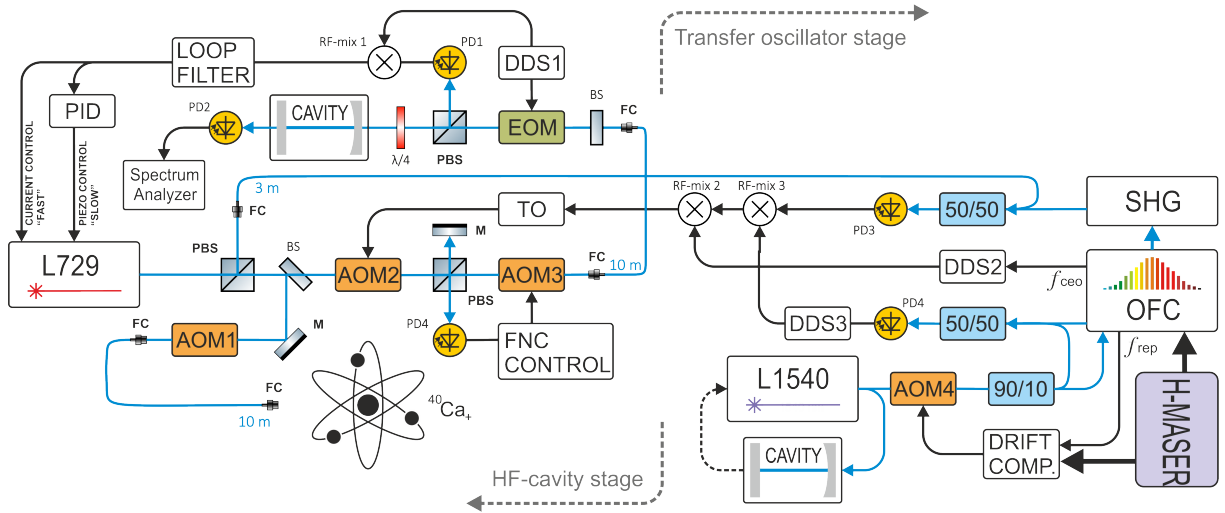
Figure 4.1: Setup for the frequency stabilization of the L729. PID: Proportional-Integral-Derivative controller, DDS: Direct Digital Synthesizer, Drift comp.: L1540 cavity drift compensation controller, AOM: Acousto-Optic Modulator, TO: Tracking oscillator, EOM: Electro-Optic Modulator, SHG: Second Harmonic Generation, FNC: Fiber Noise Cancelation, x/y: Fiber Optic Couplers, OFC: Optical Frequency Comb, SHG: Second Harmonic Generation unit.

Figure 4.2: Scheme of the TA-Pro (L729) [49]. The laser diode generate a stable light. After it pass the first isolator a portion of its light is steered out from the housing. This additional beam can be used for monitoring. The main wave is then amplified, passed through a second isolator and leave the laser housing. If the laser is well set, we can achieve an optical power of 400 mW approx.

4.1.2 Optical frequency comb

In our laboratory, we use a commercially available frequency comb[3] with an intracavity electro-optic modulator based on an Er^{3+}-doped fibre oscillator with a repetition rate $f_{rep} = 250$ MHz. The offset frequency of the COMB f_{CEO} is locked to RF reference derived from a H-maser[4]. To get a broader range of optical frequencies, the output laser beam of the OFC is doubled by a second harmonic generation (SHG) process and broadened by a photonic crystal fibre to generate a super-continuum (broad optical spectrum). The result is the OFC spectrum range from 600 to 900 nm. This gives us a reliable instrument to stabilise all the wavelengths involved with $^{40}Ca^+$ (see Fig. 1.5).

4.1.3 Transfer oscillator technique

The transfer oscillator technique produces a virtual transfer beat-note between the L729 and the L1540[5]. The mediator between two lasers is the OFC. To achieve higher coherence of the L1540, it is locked to the C1540[6].

As it was described in Sec. 3.3, using special signal conditioning under "transfer oscillator technique", the frequency noise induced by f_{rep} and f_{ceo} is removed from the beat note between L729 and the nearest OFC tooth.

The resulting virtual beat note signal between L729 and L1540 can be used either for locking the L729 optical frequency directly to L1540 or for precise monitoring and compensation of drifting exhibited by the L729 locked to a C729. In the case of this work, the second approach brings more advantages since it leads to less high-frequency technical noise to the resulting laser spectral profile.

4.1.4 Acousto-optic modulators for spectroscopy purposes

In general, the laser frequency of the transition $S_{1/2} \leftrightarrow D_{5/2}$ of $^{40}Ca^+$ does not coincide with the C729 resonance frequency. In our case, the laser frequency of L729 is needed to be tuned so that it matches the mentioned transition of the ion. For this purposes I used four AOMs[7]. They excel in many aspects (i.e. high optical power density, high diffraction efficiency, wide frequency tuning range). two of them are capable of shifting by 80 ± 40 MHz, one of them 40 ± 20 MHz and one 270 ± 100 MHz. AOM1 and AOM2 operate in the double-pass configuration. This arrangement enables to shift the frequency of the passing beam by factor two without loss in power due to the changes in coupling angle. The rest of AOMs are arranged in a single-pass configuration, which allows preservation of the beam's optical power while simultaneously operating with them. The fig. 4.1 shows the AOMs position as they follow the path of the laser. Their task is

---

[3]Menlo Systems M-Comb 1550.
[4]T4 Science iMaser 3000.
[5]NKT Koheras Basik, working at 1540.57 nm.
[6]HF-cavity (ULE), Stable lasers, finesse approx. 4.5×10^5.
[7]Brimrose corp [73].

as follows:

- AOM1 - intensity stabilisation, scanning and pulse sequencing for spectroscopy techniques with $^{40}Ca^+$ ion,

- AOM2 - slow C729 drift compensation due to aging of the HF-cavity spacer,

- AOM3 - fibre noise cancellation for the fibre connecting the laser L729 within the C729,

- AOM4 - slow C1540 drift compensation due to aging of the HF-cavity spacer L729.

The RF signals driving the AOMs are delivered either by a signal generator or by a Direct Digital Synthesizer unit, developed and built by our team in ISI CAS. All are equipped with 10 MHz stable references fed from H-maser. AOMs are operated close to their maximum RF-power limit (1.5 W), where their diffraction efficiency is specified to be optimal.

4.1.5 Electro-optic modulators

The light leaving the collimator in the C729 side first passes through a Faraday isolator. This ensures that the light reflected back will not pass through the Faraday isolator again and will not be collimated back to the L729. It prevents unwanted lasing of the L729 due to back-reflections from the optical setup. After that the light is phase modulated by an EOM[8] with frequency of $\omega = 12.9$ MHz producing the sidebands on the frequencies $\pm\Omega$ as seen in Fig. 4.3. The ratio of the optical power in the carrier and in the first sideband can be expressed as

$$\frac{P_{sideband}}{P_{carrier}} \approx 0.65. \tag{4.1}$$

4.1.6 High finesse cavity

The HF-cavity C729 operated in our laboratory is a commercially available HF-cavity working at 729 nm purchased by Stable Laser Systems. The high reflected coating on the mirror was fabricated by Advanced Thin Films. It consists of two fused silica mirrors of 0.165" thickness and 0.5" diameter, separated by a distance of 47.65 mm.

The polished finish of the inner and outer mirror substrates has a surface quality factor of 10^{-5} and 20^{-10}, respectively. Those are results from spectrometric measurements of the reflection and transmission coefficients of these substrates, carried out by the manufacturer. According to this data, the reflection coefficient r of the inner surfaces of the optical cavity mirrors at 729 nm is 0.9995, corresponding to a finesse of about 400 000 approx. But following measurement of the finesse by the ring-down technique confirmed slightly decreased value.
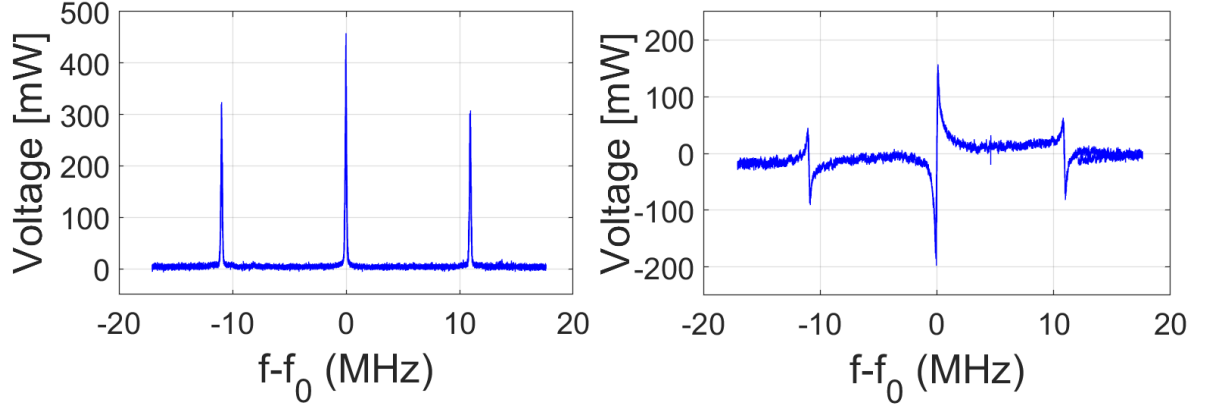
---

[8]Conoptic, model: 370 (USA)

Figure 4.3: Frequency spectrum of the EOM output with carrier and the two first order sidebands, when modulating the laser light with $\omega = 12.9$ MHz (left). A corresponding PDH error signal as the frequency of the laser were scanned. The set-point for locking the laser frequency is in the middle of the slope of of this signal (right).

The C729 spacer to which the mirrors are attached is made from premium-grade ULE glass. This type of glass has a very low thermal expansion coefficient (typically $10^{-9}K^{-1}$

The curvature of the second mirror is 500 mm. By adjusting the optical alignment of the incident beam and the axial axis of the C729 and placing the beam waist of 194 μm (calculated by Eq. (3.2)) at the plan-planar mirror (PPM), the axial modes in the C729 are generated. Even if the coupling to the C729 was optimal, the higher-order modes were always present to a small amount, especially the TEM_{01}, TEM_{10} and TEM_{11}. Those modes can distort the locking error signal and therefore diminish the performance of the C729 (lower finesse mainly). So it is in the best interest to suppress them as much as possible. Much higher-order modes were not a problem because they are out of range of the bandwidth of the locking loop. A large frequency scan of the transmission spectra of the C729 is shown in Fig. 4.4. The spectrum includes TEM_{00} modes only with the period 3.14 GHz. Some higher modes can be observed, but as they are very far from TEM_{00} mode (more than 300 MHz), they can be neglected.

Once I know the exact FSR, I calculated the C729 length using the Eq. (3.3). The resulting L of the C729 is 47.65 mm.

The finesse of the C729 was determined by the decay time τ of the light field leaking out of the C729 during the ring-down response. The exponential fit to measured data yields an average photon storage time $\tau = 17.8 \ \mu s$ thus, according to Eq. 3.14 the finesse of C729 is quantified as 351 000 approx., and the corresponding linewidth of the fundamental cavity mode is $FWHM = 8.9$ kHz approx. This narrow transition provides enough room for detecting laser frequency changes down to a Hz level.
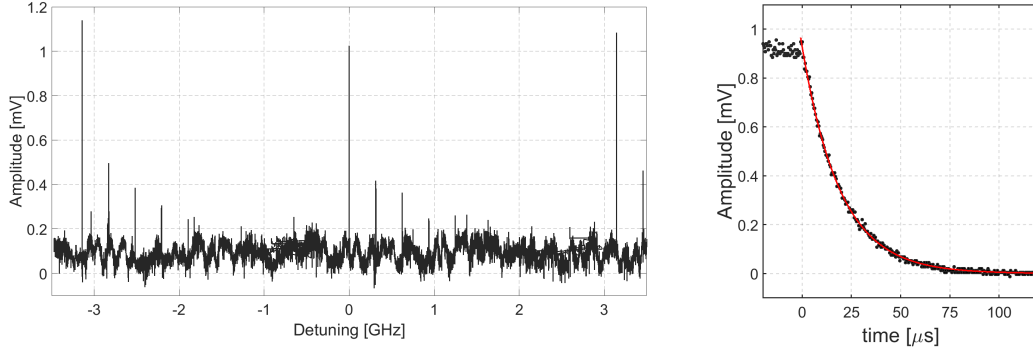
Figure 4.4: The transmission spectrum of the C729 over 9.0 GHz scanning range. The central optical frequency of the L729 was 411.041702 THz. (left). The record of the ring down measurement shows the decay of light stored inside the HF-cavity (C729) after the laser light from the L729 is switched off (right). the corresponding finesse of the C729 is 351 000 approx..

4.1.7 Optics for C729 incoupling and detection

After the EOM, the light passes through several optical components, namely the focusing lens, a beam sampler, a half-wave plate, a polarisation beam splitter (PBS) cube and the quarter-wave plate (in this order) until it reaches the first mirror of the C729. According to Subsec. 3.4.1, one needs to satisfy certain conditions for successful mode matching of the laser light into the resonance mode of the C729. The beam must be focused on the first mirror, the plane-parallel mirror. The beam waist at the position of this mirror has to have an appropriate width. By inserting the C729 diameter into the Eq. (3.2) the waist spot size on the PPM was determined to be 369 μm.

The choice of the appropriate focusing lens depends on the measured diameter of the incoming, collimated beam and the required and calculated spot size. For the fine-tuning of the focusing spot, the lens is mounted on a translation stage. The beam sampler placed before the C729 extracts a portion of the light and directs it into a photodetector for intensity monitoring followed by an intensity stabilisation. This ensures that the intensity peak visible on the transmitted spectra is caused by frequency changes and not by an intensity fluctuation of the L729 light. The intensity control also helps with unwanted heating of the C729 mirrors due to high power incoming beam. Under normal conditions, the light entering the C729 has approx. 30 μW. Using the higher power would result in a stronger PDH error signal and consequently better lock but, on the other hand, causing strong power build-up inside the optical cavity due the high-finesse of the C729. This leads to local heating of the mirrors and thus mentioned unwanted frequency drift. The quarter-wave plate ensures that the reflecting wave from the C729, which effectively passes the plate twice and thus has an opposite polarisation compared to the incoming light, will be redirected on PBS and focused into a fast photodetector. On the other side

of the C729, the transmitted light is either detected by a sensitive photodetector[9], or it is redirected to the CCD camera[10] by a flip mirror. The camera is very useful for finding the correct cavity mode, but when it is found, it is desirable to monitor the transmitted power at its full range. The overall view of the optical arrangement with the C729 HF-cavity is in Fig. 4.5.
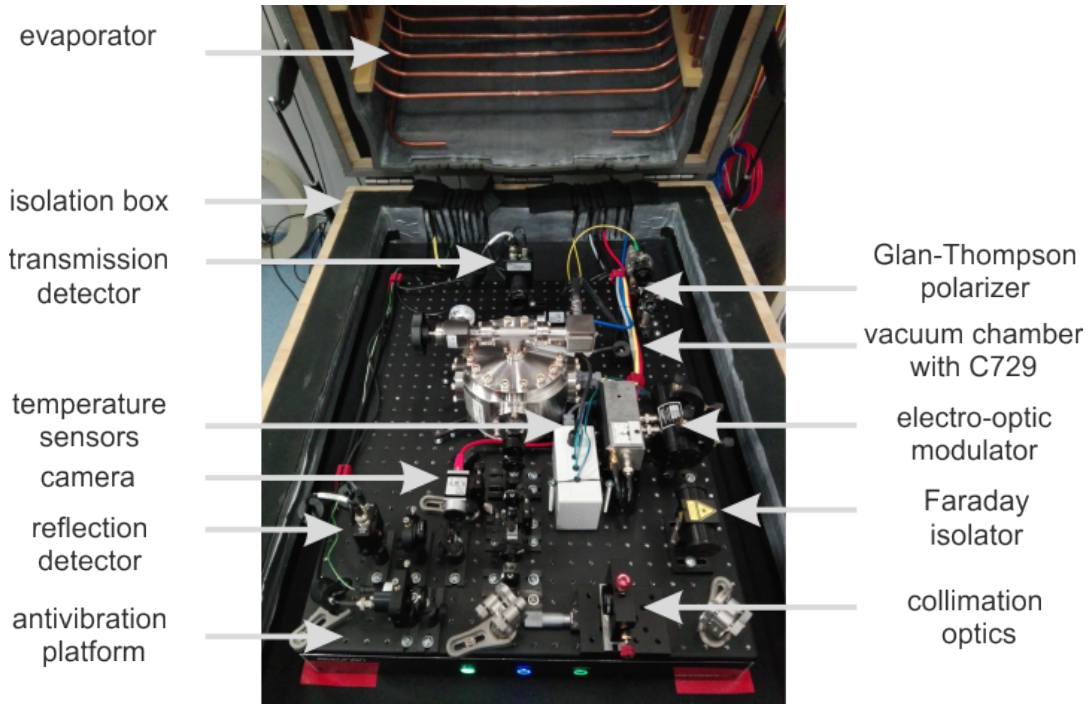
Figure 4.5: The optical setup for a mode-matching the laser wave into the C729. The vacuum chamber with the C729 is situated in the middle, surrounded by necessary optical and electro-optical elements for mode-matching, adjusting the beam waist and its spatial adjustment, cavity mode detection and generating the error locking signal. C729 optical setup lies on an anti-vibration platform on the top of several vibration isolation elements. The temperature is measured at seven points. Three PT100 temperature sensors are placed on the vacuum chamber and his surroundings. Two sensors measure the temperature of the water in both copper ends. One sensor is placed on the water heater/cooler. The lase sensor provided by Stable Systems is place in close proximity of the C729. The temperature inside the box is regulated through a water circulating in the evaporator copper tube that is installed on the box walls.

4.2 Mechanical setup

The mechanical part of the setup consists of a vacuum chamber, where the HF-cavity C729 is placed. The whole idea is to provide the cavity with a stable operating conditions

---

[9]PDA-430A, variable-gain avalanche detector, Thorlabs.
[10]Basler Ace ac460.

Figure 4.6: The view of the high-finesse optical cavity assembled in a vacuum chamber (left). Schematic of the vibration and thermal isolation platform, including the vacuum chamber and the gold, plated aluminium passive heat shield centred around the ULE cavity (The shield is temperature controlled with a Peltier element). The whole setup is then enclosed in a wooden box with thick layers of thermal isolation material (right).

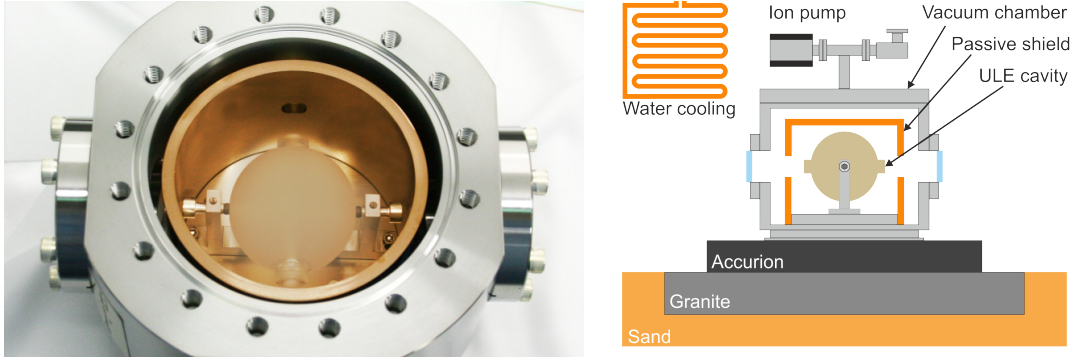and isolate the cavity from environmental perturbations such as acoustic vibration and temperature noises. The whole setup with individual isolation aspects can be seen in Fig. 4.6.

4.2.1 Vacuum chamber for HF-cavity

To minimise the fluctuation of the refractive index of the inner part of the HF-cavity, environmental vibrations on the optical cavity and thus reach a low-level thermal noise, the C729 is sealed in the vacuum chamber[11]. A high-level vacuum inside the chamber is reached with the $3\,\mathrm{l/s}$ ion getter pump[12]. The pump provides stable pressure of 7.3×10^{-8}, which is enough to isolate the cavity from thermal convection and pressure fluctuation.

In order to suppress cavity length variations due to temperature changes, the temperature of the cavity needs to be stabilised. The optimal temperature for operating the cavity is the so-called zero-crossing temperature at which the thermal expansion coefficient is crossing the zero level [74]. In the present case, the zero-crossing temperature of the C729 is 13 ± 3 °C, as was verified by the manufacturer via speed of sound measurement.

The stabilization of the cavity temperature is solved as a two-stage, in order to optimize the temperature gradient of the cavity to the laboratory where the cavity is located. The first stage is its own vacuum chamber.

The chamber contains a Peltier element[13] and a thermistors with an impedance of $10\,\mathrm{k\Omega}$ at 25 °C[14]. The thermistor is placed under the cavity holder and thus measures the temperature at very close proximity to the cavity. I used a PID-controler for temperature control of the cavity holder to keep the cavity on required temperature. The PID-controller

---

[11]Thermally insulated Stainless Steel Vacuum VH630-Can, Stable laser systems.
[12]3S Titan Ion Pump, Gamma Vacuum.
[13]TE Technology HP-127-1.0-1.3-71R.
[14]General Electric MC65F103B.

for temperature control of the cavity holder to keep the cavitz on the required temperature. The PID-controller regulates the Peltier control current so that the temperature of the cavitz holder is in 1 mK stability range at the temperature 13.5 °C. Furthermore, the cavity is enclosed inside the gold-coated aluminium passive heat shield centred around the cavity. This shield prevents the temperature exchange via radiation between the cavity and chamber walls.

To prevent the temperature gradient between the laboratory environment and the vacuum chamber. The whole setup is enclosed into a 10 mm thick wooden box inside coated with 76 mm thick foam made from compressed fibre glass[15] with 96 Kgm^{-3} density. This is the second temperature stabilizing stage. The temperature inside of the box is stabilised by a watter cooling system made from copper pipes surrounding the box walls (the helical evaporator) (Fig. 4.6).

My design of the cooling water system is based on transferring the heat obtained inside the wooden insulating box with the helical evaporator to the external radiator, which is located under the laboratory's ceiling. The transfer medium is distilled water. The external radiator is connected to the water circuit via an aluminium heater equipped with a Peltier element. The water circuit contains a water pump, but it is used only for the initialisation phase of cooling and is switched off during regular operation. The system thus works entirely on the self-gravity principle. Therefore, the liquid flow in the cooling circuit is exclusively laminar and does not generate significant acoustic interference that would be transmitted to the HF cavity.

The water circuit is equipped with three temperature sensors - thermistors. One thermistor is placed on the outlet pipe from the evaporator and the other on its inlet. The third sensor is placed in a heater fitted with the Peltier element. The temperature stabilisation inside the wooden box is based on the temperature control of the liquid that enters the evaporator in the wooden box. This temperature is monitored by the appropriate thermistor and is fed to the PID1 controller, which subsequently determines the temperature of the aluminium heater with the Peltier element. This required value is sent to the PID2 controller, which then controls the current to the aluminium cooler's Peltier element and ensures its required temperature. This system makes it possible to stabilise the temperature of the inlet liquid in the evaporator in a wooden box very robustly even when the temperature in the laboratory changes by several degrees Celsius.

The Fig. 4.8 indicates the current scheme for the water cooling system designed for temperature stabilisation of the C729 and its surroundings. The desired temperature is sent from a computer to each PIDs. They then regulate the temperature by driving the Peltier element. The temperature is measured as close to the element as possible. The temperature sensors are placed as follows. TS1 - on the aluminium cooler, TS2 - on the outlet end of the pipe, TS3 - on the inlet end of the pipe, TS4 - on the vacuum chamber, TS5 - placed in the air, TS6 - measure the temperature of the optical table, TS7 - measure the temperature of the C729.

---

[15]Prima acoustic Broadband 3".
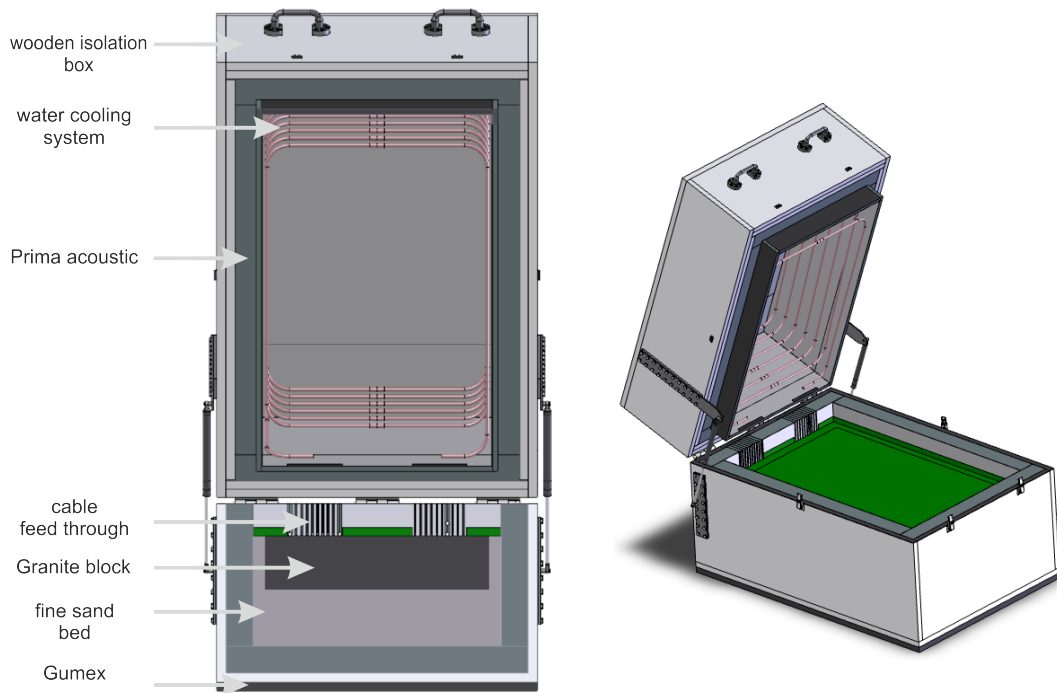
Figure 4.7: The view of a wooden box quipped with insulation elements for isolation the HF-cavity from the acoustic vibrations. The temperature inside the box is kept at stable 16°C by water cooling system (left).
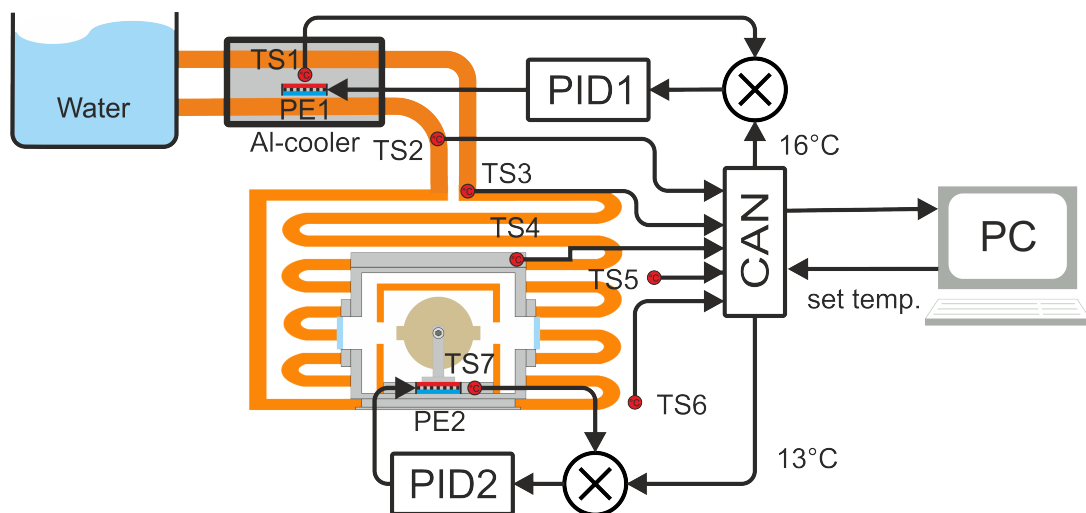
Figure 4.8: The scheme of temperature monitoring and control. PE: Peltier element, CAN: Controller Area Network, TS: Temperature sensor, PID1, PID2: Proportional-Integral-Derivative controllers. Temperature sensors: TS1 - on the aluminium cooler, TS2 - on the outlet part of the pipe, TS3 - on the inlet part of the pipe, TS4 - on the vacuum chamber, TS5 - placed in the air, TS6 - measure the temperature of the optical table, TS7 - measure the temperature of the C729 holder.

4.2.2 Vibration isolation and acoustic shielding

The vacuum chamber lies in the actively controlled vibration isolation table[16], with active bandwidth from 0.6 - 200 Hz. The isolation performance is min. 25 dB at 5 Hz and 40 dB at frequencies beyond 10 Hz. As the cavity is mounted the way that the axis of the spacer is horizontally oriented, I have decided to minimise the sensitivity of the spacers for vertical vibrations by placing the whole setup on a 250 kg block of granite. The granite block lies on a fine sand bed, and a thermal isolation box then encloses the whole setup. The block of sand is insulated from the floor by a rubber ELASTON-ELTEC FS 700 [17] which is able to absorb mechanical energy between the floor and the sand block.

Acoustic insulation consists of a 1 cm thick wooden box, which serves as the first acoustic noise isolation. The inside of the wall is laid with 76 mm thick foam made from compressed fibre glass[18] with 96 Kgm^{-3} density suppressing noise from 100 Hz to 5 kHz. The followed 2 mm thick lead sheet also adds acoustic insulation.

4.2.3 Measurement of acoustic and vibration insulation

After completing the C729 arrangement, I provided measurement of the acoustic insulation of the wooden box by a seismic accelerometer Model 731A[19] placed on the Accurion table. The record is in Fir. 4.9. For comparison, there is a record of vibration of the deflated optical table next to the wooden box where HF-cavity C729 is place. There is visible very effective suppression of vibrations in the spectral range from 0.1Hz to 150Hz by a factor 20.

4.3 Electronic setup and digital control

All the electronics used for locking the L729 to the cavity and the electronics to produce the virtual transfer beat signal were designed and built by our electronics-engineering group in the ISI CAS. If possible, the care was taken to choose low-noise active components, especially operational amplifiers.

4.3.1 Active analog loop filter - controller

The active analog loop filter module plays a role of a fast controller for locking lasers by actuating their injection current with high frequency bandwidth and minimum transport delay. Basically, it is a cascade of three operational amplifiers. The first two stages act as integrators with limited frequency response. The third stage acts as a limited differentiator. The circuitry also contains buffer amplifiers for interfacing external instruments

---

[16]Active vibration isolation system, Accurion halcyonics i4large M6/25.
[17]GUMEX company.
[18]Prima acoustic Broadband 3".
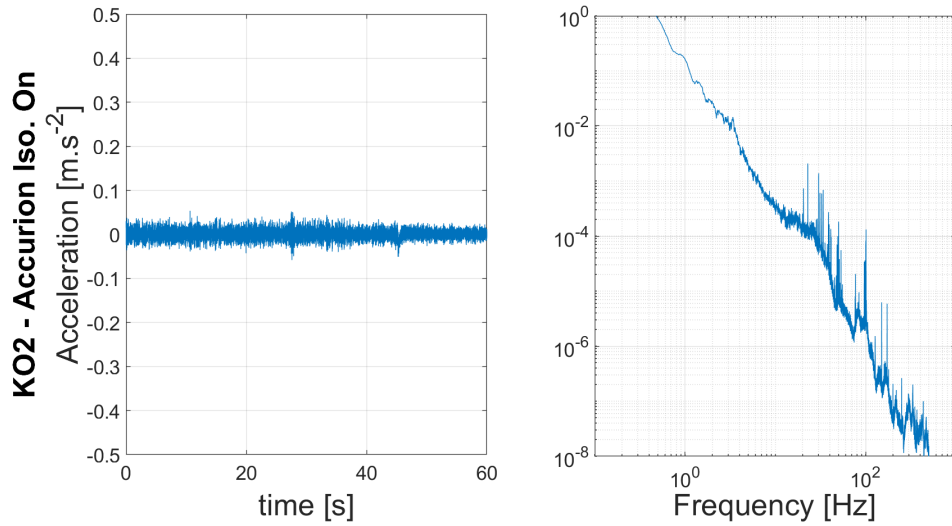[19]Wilcoxon Sensing Technologies.

Figure 4.9: Measured acoustic vibration by the seismic accelerometer Model 731A placed on the Accurion table.
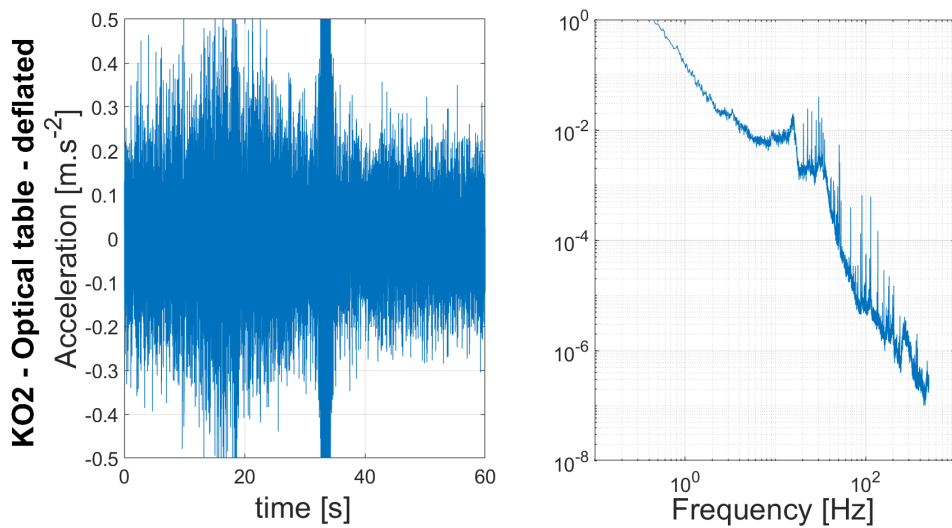

Figure 4.10: Measured acoustic vibration by the seismic accelerometer Model 731A placed on the deflated optical table next to the wooden box where HF-cavity is placed.

for monitoring the input and output signals. The active filter stages employ AD829 operational amplifiers. In the output buffer stages, the design is uses AD811 operational amplifiers, which provide both low-noise and high-bandwidth operation and output currents up to 100 mA. By triggering on-board digital inputs, the card can be remotely activated, the filter gain inverted and the slow integrator bypassed. The overall functionality of the circuit simplifies the community's well-known Toptica FALC, which lacks any remote control capabilities.

4.3.2   Digital P-I-D controller

The digital P-I-D controller employs the NXP's 56F8365 16-bit digital signal controller to implement a medium-speed digital P-I-D controller for actuating the piezo tuning stages of the L729. The input error signal is sampled using a 12-bit ADC with a 100 kHz sampling rate. The analog output control signal is produced by a 18-bit DAC at the same sampling rate. The module is fully remotely controllable and configurable from a lab computer using the Controller Area Network (CAN) bus. This card also contains a set of digital outputs which can be used to control the active loop filter card mentioned in the previous section.

4.3.3   Direct digital synthesizer

The direct digital synthesiser module is based on Analog Devices' AD9959 chip. This unit allows for simultaneously generating RF signals in 4 channels with coherent sampling. The frequency, relative phase and amplitude of each channel can be adjusted separately. The maximum generated frequency is 200 MHz. Using the on-chip PLL, the DDS sampling clock can be derived by multiplying a highly stable external reference signal. An 8-bit micro-controller (MCU) MC9S08DZ60 from NXP acts as an interface between the DDS chip and the CAN bus, which is used for the remote control.

4.3.4   Fibre noise cancellation controller

The fibre noise cancellation controller described more thoroughly in [57] is based on a modified printed circuit board of the original direct digital synthesiser module. The 8-bit MCU was replaced by a 32-bit high-speed STM32H753 digital signal processor (DSP) clocked at 400 MHz. The 16-bit ADC inputs of the DSP are digitising the output I and Q signals of an analog quadrature phase detector with the sampling rate of 4 MHz. Phase decoding and P-I-D control algorithms are implemented in the DSP that also steers the output frequency of the DDS chip over the SPI bus with 500 kHz sampling rate. This allows constructing digitally defined control loops with bandwidths up to $\approx$60 kHz. The card's firmware is versatile, so it can be reconfigured to a software defined tracking oscillator only by changing several parameters controllable over the CAN bus.

4.3.5 Digital control of the electronics and servo-loops

I used the electronics developed in ISI CAS for all control loops and supporting signal generation for providing the control of the optical setup in Fig. 4.5. I participated also on the LabVIEW software control algorithms and graphical interface for parametrization of the setup. An example of the graphic-user-interface for temperature control of the HF-cavity C729 is in Fig. 4.11
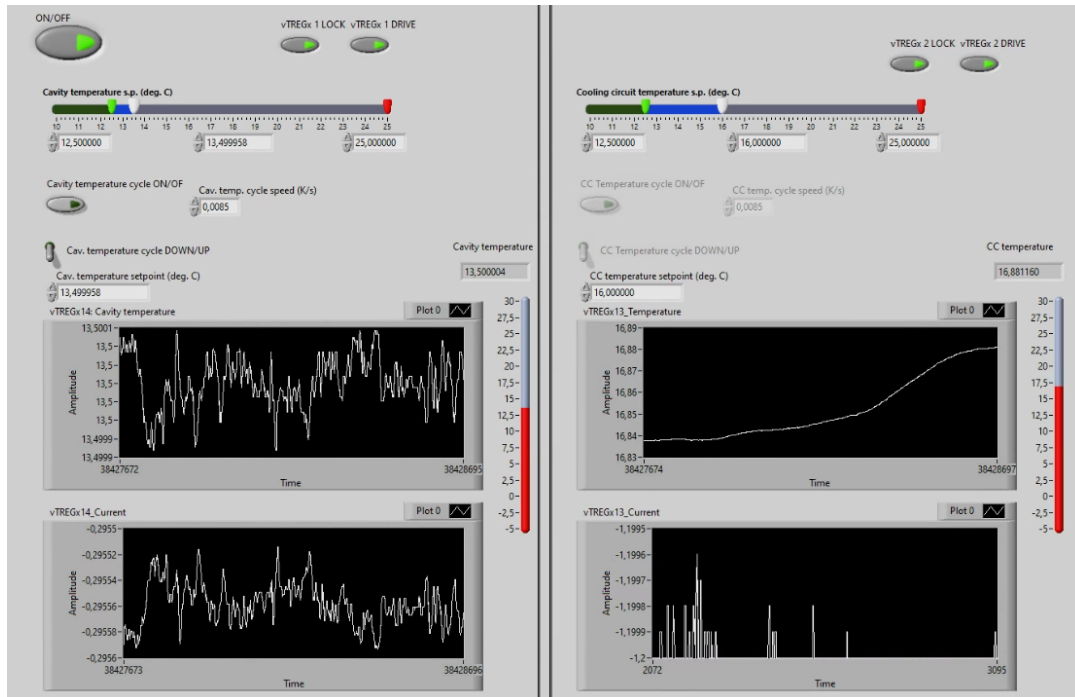

Figure 4.11: View of the control panel for the HF-cavity C729 temperature adjustment and monitoring (left). The temperature control and adjustment of the water cooling system (right). The application allows to set the desired temperature and the step how fast should it be reached. This is especially beneficial as cavities in general are very sensitive to fast temperature changes.

5. Experiments with trapped and laser cooled Calcium ion

This chapter will deliver the measurement involving the spectroscopy laser. All the measurement involving the $^{40}Ca^+$ presented in this work were measured in the $|^2S_{1/2}, m = -1/2\rangle \leftrightarrow |^2D_{5/2}, m = -1/2\rangle$ transition ($\Delta m = 0$). This transition is least sensitive to magnetic fluctuation, so the measurement of frequency behavior of the laser L729 is the most accurate. When we have a stable and precise spectroscopy laser L729, we can perform many experiments with the calcium ion. All the related spectroscopic experiments on the $S_{1/2} \leftrightarrow D_{5/2}$ transition are carried out with electron shelving, thus in pulse sequence schemes. These schemes vary with the experiment but in general, are designed as the following (Fig. 5.1).

	t [ms]	866 nm	397 nm	397 nm sig.	854 nm	729 nm	APD	
1	1,000	■	■		■			Doopler cooling
2	0,200	■		■	■			State preparation
3	2,000	■			■	■		Sideband cooling
4	0,050	■		■	■			Clear out
5	0,005	■				■		Analysis
6	0,030	■						
7	3,000	■	■				■	Detection
8	0,010	■	■	■	■			Clear out

Figure 5.1: Typical pulse sequence scheme for interrogation of $S_{1/2} \leftrightarrow P_{1/2}$ transition in electron shelving regime. The scheme can be easily altered by adding more rows as the experiments require.

The description of the electron shelving steps:

- 1 - Doppler cooling: in the first step, the ion is Doppler cooled by probing the dipole $S_{1/2} \leftrightarrow P_{1/2}$ transition with a wavelength of 397 nm and 866 nm as a pumper. This results in the ion mean vibration quantum number of less than 10 (Doppler limit).

- 2 - State preparation: the state initialization step consists of wavelength 854 nm to prevent pumping into $D_{5/2}$ and an optical pumping into $|^2S_{1/2}, m = -1/2\rangle$

- 3 - Sideband cooling: this step requires the laser L729 to be frequency tuned into the lower motional sideband (the red sideband) of the ion secular motion. The motional ground state is achieved by applying a set of pulses at 729 nm accompanied

by 854 nm. The 854 nm pulse repumps the population from long-live $D_{5/2}$ meta-stable state into a fast decaying $P_{3/2}$ state. After cooling pulses, the resulting mean vibration quantum number is close to zero (typically 0.001). This motion state of the ion is called as a ground state.

- 4 - Clear out: to ensure that the for the following experiment, the entire population is actually at $S_{1/2}(m = -1/2)$ a short pulse of circularly polarised light (397 nm sig.) is applied to the $S_{1/2} \leftrightarrow P_{1/2}$ transition. A short pulse containing 854 nm for clearing the $D_{5/2}$ state is also included.

- 5 - Quantum state analysis: after the ion is prepared into its motional ground state by previously described steps, now we can perform a designed experiment by applying several pulses of light to the $D_{1/2} \leftrightarrow D_{5/2}$ transition. The pulse duration of this step varied with the different types of experiments.

- 6 - Waiting time: it is used for detection of the phase coherence between the laser L729 and the $D_{1/2} \leftrightarrow D_{5/2}$ transition.

- 7 - Detection: during the detection, the Doppler cooling lasers at 866 and 397 nm are switched on and the fluorescence is monitored for several milliseconds. By comparing the number of counts with a threshold value, we can discriminate whether the ion was at S or D level.

- 8 – Clear out: this is the final step of the electron shelving when the quantum state of the ion is ending at $S_{1/2}$ ground state.

5.1 Spectroscopy on Zeeman levels

With the pulse sequence mentioned above, I performed the spectroscopy on Zeeman components prepared by the magnetic field of ≈ 3.2 G influencing the cooled ion in the Paul trap. The π-pulse duration (see Fig. 5.1, line 5) and the power of the laser closely correlate to each other as one can transfer all population from S to D state either by shortening the pulse duration and at the same time increase the power. High power of the laser L729 can cause spectral power broadening. Thus, it is unsuitable for this measurement when a narrow line is required.

5.2 Rabi spectroscopy

Rabi spectroscopy is named after Isidor Isaac Rabi, who initially developed this method for measuring the particle frequencies of the two-level quantum mechanical systems. It is mainly used to analyze the cyclic behaviour of a two-level quantum system in the presence of the oscillating field. The Rabi spectroscopy consists of one interaction zone, where the ion interacts with the excitation laser. In the case of $^{40}Ca^+$ ion, the Rabi oscillation

(or Rabi flop) is obtained by measuring the evolution of an excitation probability of the $S_{1/2} \leftrightarrow D_{5/2}$ transition when the pulse duration τ of the laser L729 is scanned. The intensity of the spectroscopy laser is kept constant during the measurement.
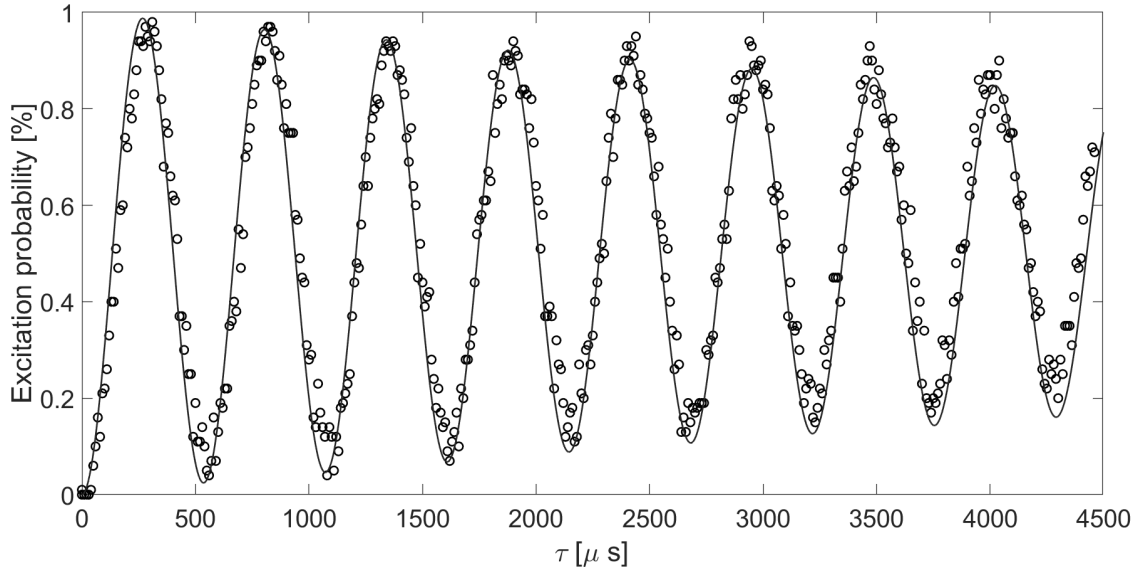
Figure 5.2: Rabi oscillation on the carrier of the $|^2S_{1/2}, m = -1/2\rangle \leftrightarrow |^2D_{5/2}, m = -1/2\rangle$ transition. If there are induced incoherence between the ground and excited levels, the Rabi oscillation slowly decays over the pulse length.

Fig. 5.2 shows the measured Rabi oscillation on carrier of the transition spectra. The Oscillation slowly decrease to 50% excitation probability as the pulse length gets longer. This is due to accumulation of incoherence to the probing laser.

We can set the π-pulse to a certain time when we excite the $|S_{1/2}\rangle \leftrightarrow |D_{5/2}\rangle$ transition and scan the frequency over this transition. Thus the L729 is in scanning regime and we can see the carrier of the transition and motional sidebands generated by a secular motion of the ion in the Paul trap.

Fig. 5.3 shows the frequency spectrum of one Zeeman component, more precisely $|^2S_{1/2}, m = -1/2\rangle \leftrightarrow |^2D_{5/2}, m = -1/2\rangle$ with its first axial and radial motional sidebands.

5.3 Ramsey spectroscopy

Ramsey spectroscopy, also known as a separated oscillating field method [75, 76], is a particle interferometry method used for measuring the particle transition frequencies. Today's most precision atomic measurements, the SI unit definition of the second or atom interferometer, have a Ramsey-type configuration in their detection chain.

The main goal of precision spectroscopy is to find the absorption frequency between the ground and the excited state of the ion. This can be accomplished by applying the
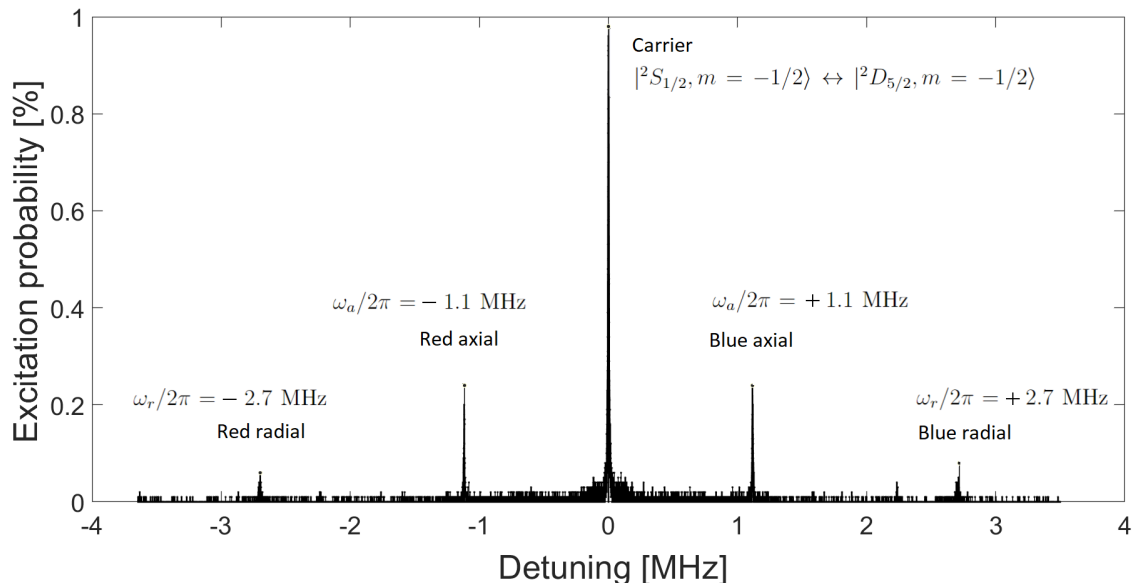
Figure 5.3: Spectrum of $|^2S_{1/2}, m = -1/2\rangle \leftrightarrow |^2D_{5/2}, m = -1/2\rangle$ transition measured with one ion in the trap. We see typical secular frequencies $\omega_r/2\pi = 2.7$ MHz in the radial and $\omega_a/2\pi = 1.1$ MHz in the axial direction.

external electromagnetic field at the frequency ω and finding the differences (also known as detuning Δ) between ω and the resonant frequency ω_0 of the transition. The excitation probability is maximized when $\Delta = 0$.

Ramsey spectroscopy is an improvement of the Rabi method by splitting the one interaction pulse (π-pulse) into two very short interaction pulses ($\pi/2$-pulse). By shortening the interaction time between the ion and the laser, there is less time to transfer the induced noise from the source. This leads to more precise determination of the Δ. The two $\pi/2$ pulses are separated by a much longer non-interaction zone (know as Ramsey time, τ_R). The Ramsey time determines the linewidth of the Ramsey fringe and thus the resolution with which Δ can be determined. The linewidth of the Ramsey fringe δ_ν is defined as

$$\delta_\nu \sim \frac{1}{\tau_R}. \tag{5.1}$$

By increasing the τ_R one can increase the precision of the detected frequency detuning. The Ramsey fringe, as it is observed through the frequency scan, is shown in the Fig.5.4. The set parameters are $\pi/2$-pulses $= 20$ μs and Ramsey waiting time $\tau_R = 1$ ms. The Ramsey pattern is effectively an oscillation under the envelope of the Rabi method.

5.3.1 Test of qubit's decoherence

The Ramsey spectroscopy is perfectly suited for a test of qubit's decoherence [77]. The experiment consists of two $\pi/2$ pulses with a probe time duration of 20 μs separated
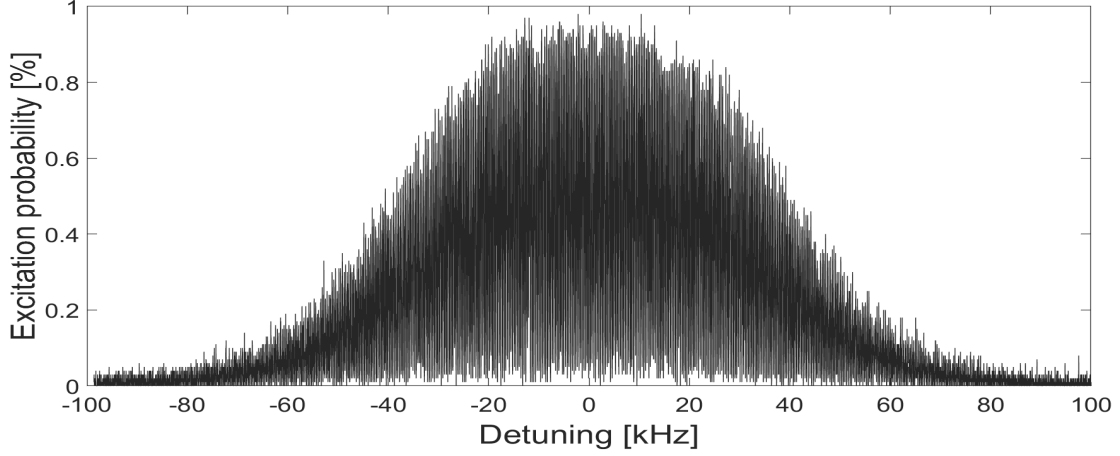
(a) Frequency scan over the carrier with Ramsey sequence.
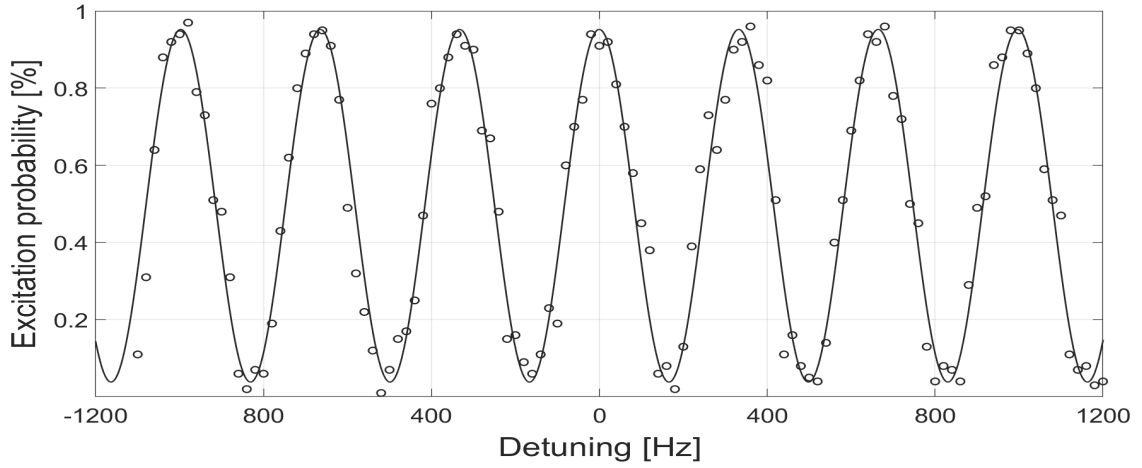
(b) A detailed zoom in 2 kHz window around the center frequency.

Figure 5.4: Frequency scan over the carrier of the $|^2S_{1/2}, m = -1/2\rangle \leftrightarrow |^2D_{5/2}, m = -1/2\rangle$ transition with a Ramsey sequence. The sequence consists of two $\pi/2$-pulses $= 20$ μs separated by Ramsey waiting time $\tau_R = 1$ ms.

by a waiting time τ_R. After applying the second pulse, the state of the ion is detected by electron shelving using the APD for fluorescence detection. Each experiment is repeated hundred times to obtain an excitation probability. Ideally, the excitation to $D_{5/2}$ should exhibit the modulation between zero and one when changing the phase between two pulses. The loss of contrast in this observed pattern is caused by a dephasing of the qubit levels when the superposition of the $|S\rangle$ and the $|D\rangle$ is exposed to decoherence for a long time. I have systematically measured the Ramsey contrast for varied delay times between two pulses (5 μs up to 10000 μs). Each data set was fitted to a sinusoidal function to get the final contrast. The observed contrast $C = P_D^{max} - P_D^{min}/P_D^{max} + P_D^{min}$ was plotted versus
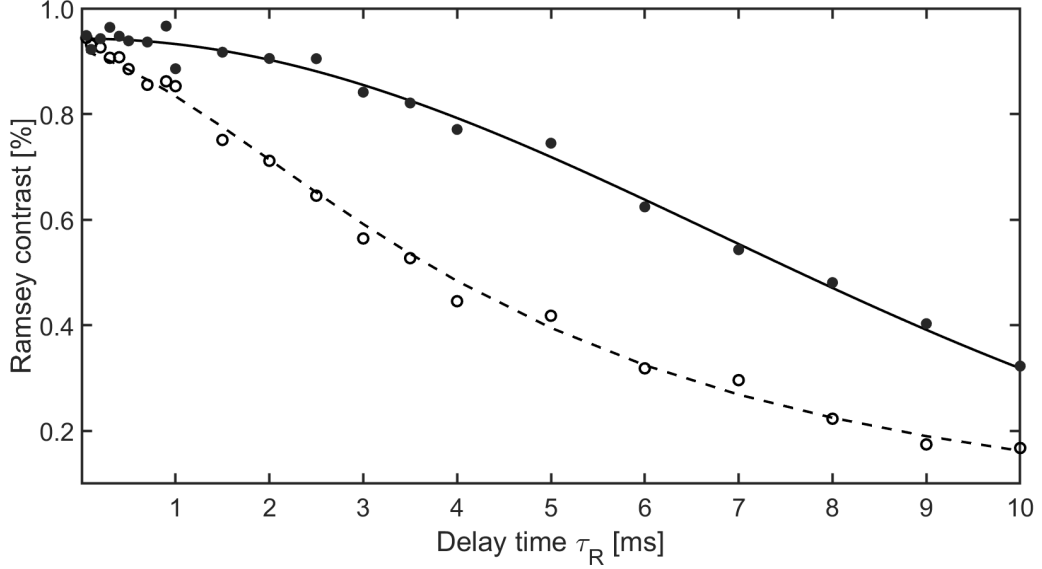
Figure 5.5: The contrast of the Ramsey pattern as a function of the delay time. Both (solid and open) circles are the data measured on the same Zeeman component ($|^2S_{1/2}, m = -1/2\rangle \leftrightarrow |^2D_{5/2}, m = -1/2\rangle$) with the same waiting time (τ_R). Open circles represented measurement when the L729 was locked to the virtual transfer beat. Solid circles represented the measurement when the L729 was referenced by the HF-cavity length, and its drift was compensated using the transfer oscillator technique. The coherent time was extended nearly twice.

the delay time in Fig. 5.5. To describe the decrease of contrast, we fit the measured data with a Gaussian function. The resulting laser linewidth $\Delta_{\nu_{FWHM}} = 29$ Hz corresponds to Ramsey time of 7.64 μs. Thus with the L729 locked to the C729 and using the TO as a fine-tuning tool, we increased the Ramsey contrast by order of two. For the comparison, I also measured the Ramsey contrast for $\Delta m = 2$ with a similar results.

5.3.2 Locking the L729 to $S_{1/2} \leftrightarrow D_{5/2}$ transition of $^{40}Ca^+$

Ramsey spectroscopy is foremost used as a tool to reference the laser to the ion forbidden transition ($S_{1/2} \leftrightarrow D_{5/2}$). There are several methods to reference the clock laser into such a clock transition. The simplest way is to lock the optical frequency of the laser to the highest peak of the Ramsey fringe. Nevertheless, the situation is similar to when one locks the laser to the cavity mode. The fluctuation of the peak intensity cannot be traced and can be caused either by the intensity instability of the laser or the frequency deviation from the central frequency. To trace the frequency fluctuation setting, the measuring point at the middle of the fringe slope seems the most appropriate. Similar to HF-cavity, at this point, the slightest change in frequency causes a massive response in detected intensity (in this case, excitation probability). However, how can one decide the direction of the frequency drift? To overcome this trouble, we can deploy a second measuring point

on the opposite side of the same fringe. We will call the measured excitation probabilities in those points as P_L and P_R (left and right side of the fringe).

P_L and P_R are separated by a line width of the fringe. We then set the frequency of the AOM f_{AOM} so that it matches the centre frequency f_{centre} of the highest peak. If the excitation probability at the f_{centre} changes due to a drop-off laser intensity, the P_L and P_R will remain the same. When the excitation probability on the one measured point changes due to the frequency deviation from the f_{centre}, the excitation probability of the other measured point will change by the same amount but in the opposite direction. P_L and P_R are sent to the digital servo loop controller, which then accordingly adjusts the f_{AOM} so that the P_L and P_R are equal and ideally at 50% probability.

The computed Allan deviation (ADEV) is a traditional way to estimate the frequency stability of the clock [78]. Allan deviation is defined as

$$\sigma_y(\tau) = \sqrt{\sigma_y^2(\tau)}, \tag{5.2}$$

where the $\sigma_y^2(\tau)$ is Allan variance, which is defined as

$$\sigma_y^2(\tau) = \frac{1}{2}(\overline{y}_{n+1} - \overline{y})^2. \tag{5.3}$$

The τ is the observation period, $\overline{y}_n$ is the nth fractional frequency average over the observation time τ. The samples are taken with no dead-time between them, which means the time between each frequency sample is equal to τ.

Usually, the clock stability is compared against a far more accurate reference. The most stable reference available in our laboratory in ISI CAS is the H-maser. The stability of the H-maser can reach approx. 1×10^{-15} for the integration time in the vicinity of 10^4.

The ADEV in our case is computed from extracted frequencies f_{AOM} over the measured time. Here we can see that at the very short time τ, the ADEV is high. This is due to noise contribution. This hump at $\tau = 30$ s comes from the servo loop for compensating the drifting of the C1540. This was later found during the comparison campaign between the ISI CAS and the Federal office of metrology and surveying [57]. At longer τ the noise is average out. Hence the ADEV decreases. The error bars increase with the τ because large τ requires many data points, and thus, it is time-consuming. The lowest part of the ADEV (before it starts to increase again) is the highest achieved stability. This is not observed in the presented ADEV as the measured data points was too short.
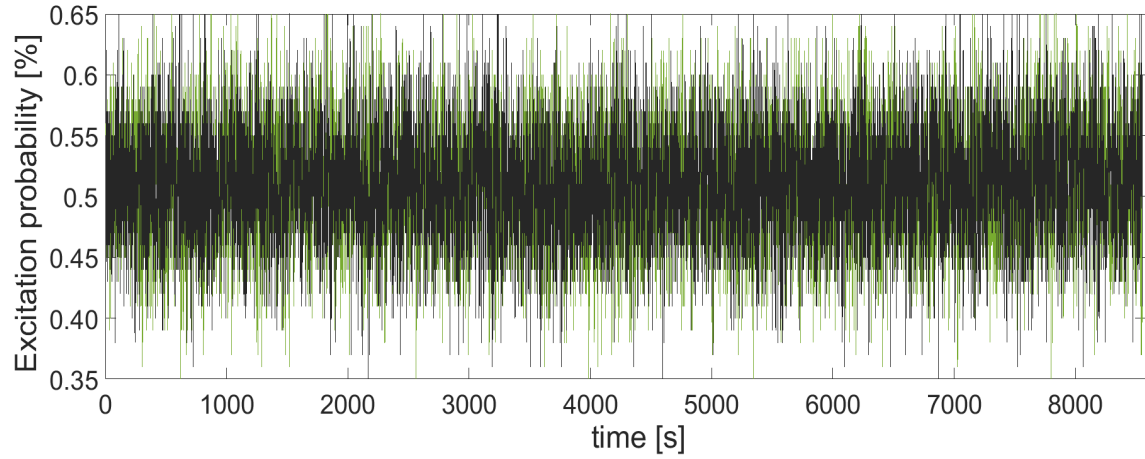
(a)
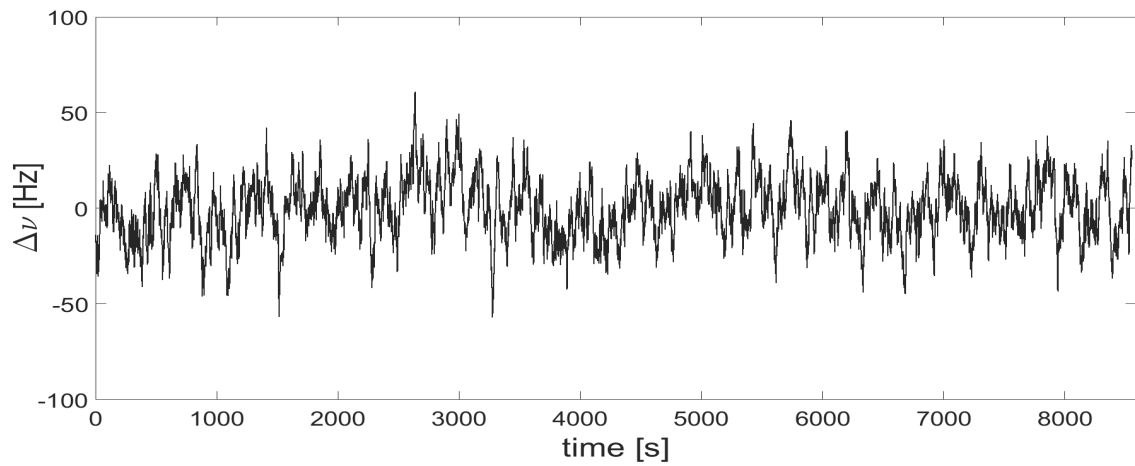
(b).

Figure 5.6: (a) The plot of the excitation probability of two measured points symmetrically placed around the central frequency. When the laser L729 is locked to the $|^2 S_{1/2}, m = -1/2\rangle \leftrightarrow |^2 D_{5/2}, m = -1/2\rangle$ transition of $^{40}Ca^+$, their values remain the same over the measured time. (b), The extracted frequency deviation from the center frequency of $|^2 S_{1/2}, m = -1/2\rangle \leftrightarrow |^2 D_{5/2}, m = -1/2\rangle$ transition .

Figure 5.7: Allan deviation for extracted frequency of the AOM when the L729 is locked to the $|{}^2S_{1/2}, m = -1/2\rangle \leftrightarrow |{}^2D_{5/2}, m = -1/2\rangle$ transition within Ramsey technique detection of the central frequency of this transition.

Conclusion

This doctoral work aimed to develop a laser source with an ultra-narrow spectral emission line called a spectroscopy or clock laser. The ultra-narrow spectral linewidth is crucial not only for high-resolution spectroscopy on trapped and laser-cooled particles but the laser is also used for ground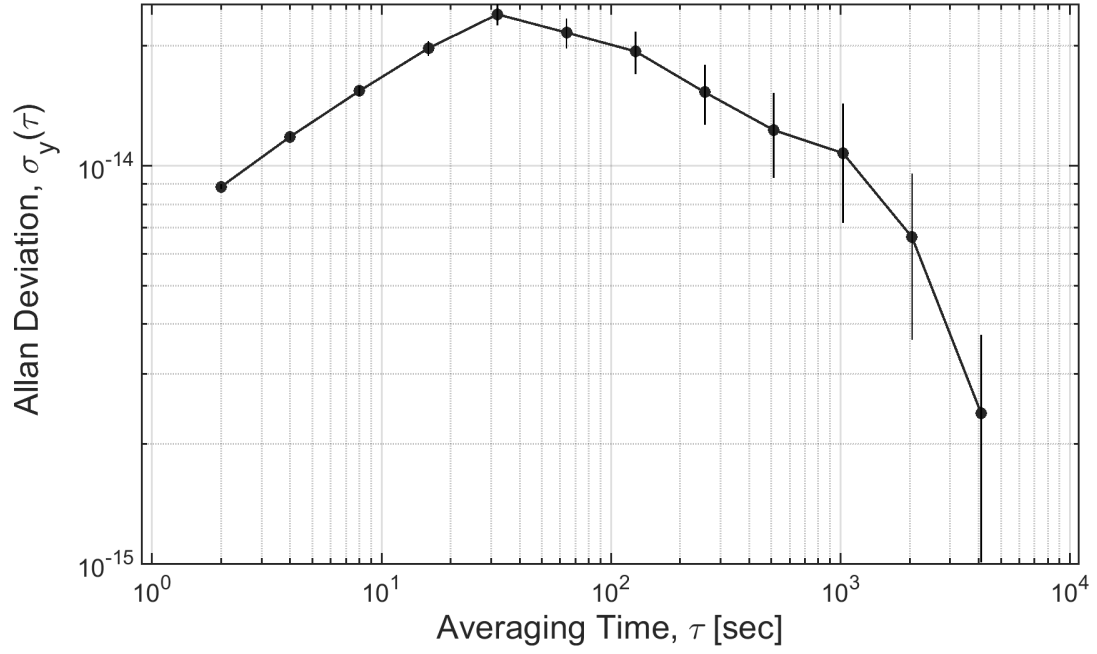-state cooling, electron shelving techniques and many other application as an interrogation source. The laser source thus must excel in short-term stability as well as in long-term stability. This is not an easy task as one usually must reconcile with one at the expense of the other.

The heart of our optical atomic clock system is a $^{40}Ca^+$ ion. The clock transition of the Ca ion is an electric quadrupole transition $S_{1/2} \leftrightarrow D_{5/2}$. It has a rather long lifetime, > 1 s. Thus, to transfer the population into this level coherently, the probing laser has to have a linewidth at the Hz or sub-Hz level. However, by driving this transition, one can get a stable oscillation of 411 THz with 1 Hz precision. This is the ultimate aim of my work.

The work mainly focuses on exploring and analysing the available method to stabilise the optical frequency of the external cavity diode laser working at 729 nm (model TA-Pro, Toptica). The L729, in its free-running regime, has a relatively wide spectral linewidth (approx. 300 kHz).

After a thorough investigation and implementation of various frequency spectral narrowing techniques, i.e. phase lock the laser to an optical frequency comb, stabilisation using the unbalanced Mach-Zehnder interferometer with a fibre spool, implementing a transfer oscillator technique. I came to the conclusion that the best technique (in both short-term and long-term point of view) is to optically reference the L729 by locking its optical frequency to the ultra-stable reference, a high finesse optical cavity followed de-drifting of the cavity aging by the complex setup with the optical frequency comb disciplined by the RF reference – Hydrogen maser. It led to very complex arrangement where I took many experiences from the field of vacuum technique, wave optics, polarization optics, optical modulators, spectroscopy detection techniques, control and analog and digital signal processing, RF electronics and finally as well as from the field of quantum physics and quantum mechanics.

I have designed and built a complete vacuum, optical and mechanical system to ensure reliable cavity operation. The optical part consists of elements for mode-matching the laser to the cavity and for generating the locking error signal. I designed and experimentally realized the mechanical arrangement of the cavity box witch isolated the cavity from the laboratory environment consisting of thermal fluctuation and vibration noise.

I put together the complex optical setup where the laser L729 optical frequency is locked to the cavity mode using the Pound-Drever-Hall detection technique in a servo loop. However, even though I achieved an ultra-narrow spectroscopy laser L729, the locking frequency exhibited a drift due to the Brownian and ageing effects affecting the cavity. I have used a transfer oscillator technique with help of the optical frequency comb

disciplined by the H-maser to bypass this problem as a precise tracking oscillator, which then tunes the frequency of the AOM before HF-cavity; so that the unwanted frequency drift is compensated. I also completed the ring-down response technique for HF-cavity finesse investigation. The cavity finesse measured by a ring-down response is 351 000, corresponding to the linewidth of the fundamental mode of the cavity to 8.9 kHz. I implemented and fully exploited Ramsey spectroscopy technique for a test of qubit's decoherence of $^{40}Ca^+$ ion with the L729 laser and thus testing the performance of the spectroscopy laser. I have then systematically measured the Ramsey contrast for varied delay times between two pulses (5 s up to 10000 s)

I fitted the measured data with a Gaussian function to describe the linewidth of the L729 laser. The resulting laser linewidth of the L729 is $\Delta_{\nu_{FWHM}} = 29$ Hz which corresponds to the Ramsey time of 7.64 μs. I assume that the majority of the noise component causing the spectral broadening in the resulting laser linewidth is caused by the unstabilised optical fibre path between the laser and the vacuum chamber with the trapped ion. This will be a part of future research.

After my final adjustment of the narrowed laser L729 for spectroscopy purposes, the laser was used for many experiments in quantum physics, quantum mechanics, and time metrology. Since it was possible to achieve significant results with this laser, which were subsequently published (see Appendix I-III of the thesis), I consider the completed spectroscopic laser L729 to be the key to further research in the field of laser ion cooling, experiments in quantum mechanics and fundamental time metrology, such as the operation of optical atomic clocks.

References

1. HALL, John L. Nobel Lecture: Defining and measuring optical frequencies. *Reviews of Modern Physics* [online]. 2006, vol. 78, no. 4, pp. 1279–1295 [visited on 2022-06-24]. Available from DOI: `10.1103/RevModPhys.78.1279`. Publisher: American Physical Society.

2. HANSCH, Theodor W. Nobel Lecture: Passion for precision. *Reviews of Modern Physics* [online]. 2006, vol. 78, no. 4, pp. 1297–1309 [visited on 2022-06-24]. Available from DOI: `10.1103/RevModPhys.78.1297`. Publisher: American Physical Society.

3. WINELAND, David J. Nobel Lecture: Superposition, entanglement, and raising Schrodinger's cat. *Reviews of Modern Physics* [online]. 2013, vol. 85, no. 3, pp. 1103–1114 [visited on 2022-06-24]. Available from DOI: `10.1103/RevModPhys.85.1103`. Publisher: American Physical Society.

4. SCHIOPPO, M.; BROWN, R. C.; MCGREW, W. F.; HINKLEY, N.; FASANO, R. J.; BELOY, K.; YOON, T. H.; MILANI, G.; NICOLODI, D.; SHERMAN, J. A.; PHILLIPS, N. B.; OATES, C. W.; LUDLOW, A. D. Ultrastable optical clock with two cold-atom ensembles. *Nature Photonics* [online]. 2017, vol. 11, no. 1, pp. 48–52 [visited on 2022-06-24]. ISSN 1749-4893. Available from DOI: `10.1038/nphoton.2016.231`. Number: 1 Publisher: Nature Publishing Group.

5. LEIBFRIED, D.; BLATT, R.; MONROE, C.; WINELAND, D. Quantum dynamics of single trapped ions. *Reviews of Modern Physics* [online]. 2003, vol. 75, no. 1, pp. 281–324 [visited on 2022-05-30]. ISSN 0034-6861, ISSN 1539-0756. Available from DOI: `10.1103/RevModPhys.75.281`.

6. HAWKINS, Gerald S. *Stonehenge decoded*. 1966. OCLC: 16772970.

7. BRUTON, Eric. *The history of clocks and watches* [online]. New York : Crescent Books : Distributed by Crown, 1982 [visited on 2022-05-30]. ISBN 978-0-517-37744-4. Available from: `http://archive.org/details/historyofclocksw0000brut_u3o0`.

8. DAVIES, Eryl. *DK Pockets: Inventions*. London: Dorling Kindersley, 1995. ISBN 978-0-7513-5184-2.

9. HORTON, J.W.; MARRISON, W.A. Precision Determination of Frequency. *Proceedings of the Institute of Radio Engineers*. 1928, vol. 16, no. 2, pp. 137–154. ISSN 2162-6626. Available from DOI: `10.1109/JRPROC.1928.221372`. Conference Name: Proceedings of the Institute of Radio Engineers.

10. DELVA, Pacôme; LODEWYCK, Jérôme. *Atomic clocks: new prospects in metrology and geodesy* [online]. 2013-08 [visited on 2022-05-30]. Tech. rep., arXiv:1308.6766. arXiv. Available from DOI: `10.48550/arXiv.1308.6766`. arXiv:1308.6766 [gr-qc, physics:physics] type: article.

11. SULLIVAN, D.B. Time and frequency measurement at NIST: the first 100 years. In: *Proceedings of the 2001 IEEE International Frequncy Control Symposium and PDA Exhibition (Cat. No.01CH37218)*. 2001, pp. 4–17. Available from DOI: 10.1109/FREQ.2001.956152. ISSN: 1075-6787.

12. *The Nobel Prize in Physics 2005* [online]. [N.d.] [visited on 2022-06-06]. Available from: https://www.nobelprize.org/prizes/physics/2005/summary/.

13. UDEM, Th.; DIDDAMS, S. A.; VOGEL, K. R.; OATES, C. W.; CURTIS, E. A.; LEE, W. D.; ITANO, W. M.; DRULLINGER, R. E.; BERGQUIST, J. C.; HOLLBERG, L. Absolute Frequency Measurements of the Hg+and Ca Optical Clock Transitions with a Femtosecond Laser. *Physical Review Letters* [online]. 2001, vol. 86, no. 22, pp. 4996–4999 [visited on 2022-05-30]. Available from DOI: 10.1103/PhysRevLett.86.4996. Publisher: American Physical Society.

14. DIDDAMS, S. A.; UDEM, Th.; BERGQUIST, J. C.; CURTIS, E. A.; DRULLINGER, R. E.; HOLLBERG, L.; ITANO, W. M.; LEE, W. D.; OATES, C. W.; VOGEL, K. R.; WINELAND, D. J. An Optical Clock Based on a Single Trapped 199Hg+ Ion. *Science* [online]. 2001, vol. 293, no. 5531, pp. 825–828 [visited on 2022-05-31]. Available from DOI: 10.1126/science.1061171. Publisher: American Association for the Advancement of Science.

15. *Optical Atomic Clocks* [online]. 2015 [visited on 2022-06-20]. Available from DOI: 10.48550/arXiv.1407.3493. Number: arXiv:1407.3493 arXiv:1407.3493 [physics].

16. *Nuclear clocks for testing fundamental physics* [online]. 2020 [visited on 2022-06-20]. Available from DOI: 10.48550/arXiv.2012.09304. Number: arXiv:2012.09304 arXiv:2012.09304 [nucl-ex, physics:physics, physics:quant-ph].

17. POLI, N.; OATES, C. W.; GILL, P.; TINO, G. M. Optical atomic clocks. *La Rivista del Nuovo Cimento* [online]. 2013, vol. 36, no. 12, pp. 555–624 [visited on 2022-06-20]. ISSN 0393697X, ISSN 0393697X. Available from DOI: 10.1393/ncr/i2013-10095-x. arXiv:1401.2378 [physics].

18. *An Optical Atomic Clock Based on a Highly Charged Ion.* [N.d.]. Available from DOI: 10.48550/arXiv.2205.13053.

19. *Fundamental Physics with a State-of-the-Art Optical Clock in Space* [online]. 2021 [visited on 2022-06-20]. Available from DOI: 10.48550/arXiv.2112.10817. Number: arXiv:2112.10817 arXiv:2112.10817 [gr-qc, physics:physics].

20. *Evaluation of the performance of a 40Ca+ - 27Al+ optical clock* [online]. 2020 [visited on 2022-06-20]. Available from DOI: 10.48550/arXiv.2012.05496. Number: arXiv:2012.05496 arXiv:2012.05496 [physics].

21. AHARON, Nati; SPETHMANN, Nicolas; LEROUX, Ian D.; SCHMIDT, Piet O.; RETZKER, Alex. Robust optical clock transitions in trapped ions. *New Journal of Physics* [online]. 2019, vol. 21, no. 8, p. 083040 [visited on 2022-06-20]. ISSN 1367-2630. Available from DOI: `10.1088/1367-2630/ab3871`. arXiv:1811.06732 [physics, physics:quant-ph].

22. CAO, Jian; ZHANG, Ping; SHANG, Junjuan; CUI, Kaifeng; YUAN, Jinbo; CHAO, Sijia; WANG, Shaomao; SHU, Hualin; HUANG, Xueren. A transportable 40Ca+ single-ion clock with 7.7x10^(-17) systematic uncertainty. *Applied Physics B* [online]. 2017, vol. 123, no. 4, p. 112 [visited on 2022-06-20]. ISSN 0946-2171, ISSN 1432-0649. Available from DOI: `10.1007/s00340-017-6671-5`. arXiv:1607.03731 [physics].

23. SAHOO, B.; ISLAM, M.; DAS, B; CHAUDHURI, R.; MUKHERJEE, D. Lifetimes of the metastable D3/2,5/22 states in Ca+, Sr+, and Ba+. *Physical Review A*. 2006, p. 62504.

24. LIAW, Sy-Sang. Ab initio calculation of the lifetimes of 4p and 3d levels of 40Ca+. *Physical Review A* [online]. 1995, vol. 51, no. 3, R1723–R1726 [visited on 2022-06-01]. Available from DOI: `10.1103/PhysRevA.51.R1723`. Publisher: American Physical Society.

25. OBSIL, P.; LESUNDAK, A.; PHAM, T.; LAKHMANSKIY, K.; PODHORA, L.; ORAL, M.; CIP, O.; SLODICKA, L. A room-temperature ion trapping apparatus with hydrogen partial pressure below 10^(-11) mBar. *Review of Scientific Instruments* [online]. 2019, vol. 90, no. 8, p. 083201 [visited on 2022-06-19]. ISSN 0034-6748, ISSN 1089-7623. Available from DOI: `10.1063/1.5104346`. arXiv:1904.13242 [physics, physics:quant-ph].

26. XU, Xiao-Tian; WANG, Zong-Yao; JIAO, Rui-Heng; YI, Chang-Rui; SUN, Wei; CHEN, Shuai. Ultra-low noise magnetic field for quantum gases. *Review of Scientific Instruments* [online]. 2019, vol. 90, no. 5, p. 054708 [visited on 2022-06-20]. ISSN 0034-6748, ISSN 1089-7623. Available from DOI: `10.1063/1.5087957`. arXiv:1904.11642 [physics, physics:quant-ph].

27. MERKEL, B.; THIRUMALAI, K.; TARLTON, J. E.; SCHÄFER, V. M.; BALLANCE, C. J.; HARTY, T. P.; LUCAS, D. M. Magnetic field stabilization system for atomic physics experiments. *Review of Scientific Instruments* [online]. 2019, vol. 90, no. 4, p. 044702 [visited on 2022-06-20]. ISSN 0034-6748, ISSN 1089-7623. Available from DOI: `10.1063/1.5080093`. arXiv:1808.03310 [physics, physics:quant-ph].

28. HANLEY, R. K.; ALLCOCK, D. T. C.; HARTY, T. P.; SEPIOL, M. A.; LUCAS, D. M. Precision measurement of the 43Ca+nuclear magnetic moment. *Physical Review A* [online]. 2021, vol. 104, no. 5, p. 052804 [visited on 2022-06-20]. ISSN 2469-9926, ISSN 2469-9934. Available from DOI: `10.1103/PhysRevA.104.052804`. arXiv:2105.10352 [nucl-ex, physics:physics, physics:quant-ph].

29. RUSTER, T.; SCHMIEGELOW, C. T.; KAUFMANN, H.; SCHMIDT KALER, F.; WARSCHBURGER, C.; POSCHINGER, U. G. A long lived Zeeman trapped-ion qubit. *Applied Physics B* [online]. 2016, vol. 122, no. 10, p. 254 [visited on 2022-06-20]. ISSN 0946-2171, ISSN 1432-0649. Available from DOI: `10.1007/s00340-016-6527-4`. arXiv:1606.07220 [quant-ph].

30. HUANG, Y.; CAO, J.; LIU, P.; LIANG, K.; OU, B.; GUAN, H.; HUANG, X.; LI, T.; GAO, K. Hertz-level Measurement of the 40Ca+ 4s 2S1/2-3d 2D5/2 Clock Transition Frequency With Respect to the SI Second through GPS. *Physical Review A* [online]. 2012, vol. 85, no. 3, p. 030503 [visited on 2022-06-20]. ISSN 1050-2947, ISSN 1094-1622. Available from DOI: `10.1103/PhysRevA.85.030503`. arXiv:1111.5174 [physics].

31. MATSUBARA, Kensuke; HACHISU, Hidekazu; LI, Ying; NAGANO, Shigeo; LOCKE, Clayton; NOGAMI, Asahiko; KAJITA, Masatoshi; HAYASAKA, Kazuhiro; IDO, Tetsuya; HOSOKAWA, Mizuhiko. Direct comparison of a Ca+ single ion clock against a Sr optical lattice clock. *Optics Express* [online]. 2012, vol. 20, no. 20, p. 22034 [visited on 2022-06-20]. ISSN 1094-4087. Available from DOI: `10.1364/OE.20.022034`. arXiv:1208.4654 [physics, physics:quant-ph].

32. ROOS, C. F.; CHWALLA, M.; KIM, K.; RIEBE, M.; BLATT, R. 'Designer atoms' for quantum metrology. *Nature* [online]. 2006, vol. 443, no. 7109, pp. 316–319 [visited on 2022-06-20]. ISSN 0028-0836, ISSN 1476-4687. Available from DOI: `10.1038/nature05101`. arXiv:quant-ph/0701215.

33. JAMES, D.F.V. Quantum dynamics of cold trapped ions with application to quantum computation. *Applied Physics B* [online]. 1998, vol. 66, no. 2, pp. 181–190 [visited on 2022-06-01]. ISSN 1432-0649. Available from DOI: `10.1007/s003400050373`.

34. ROOS, C. F.; LEIBFRIED, D.; MUNDT, A.; SCHMIDT-KALER, F.; ESCHNER, J.; BLATT, R. Experimental demonstration of ground state laser cooling with electromagnetically induced transparency. *Physical Review Letters* [online]. 2000, vol. 85, no. 26, pp. 5547–5550 [visited on 2022-05-20]. ISSN 0031-9007, ISSN 1079-7114. Available from DOI: `10.1103/PhysRevLett.85.5547`. arXiv:quant-ph/0009034.

35. HENDRICKS, R. J.; SORENSEN, J. L.; CHAMPENOIS, C.; KNOOP, M.; DREWSEN, M. Doppler cooling of calcium ions using a dipole-forbidden transition. *Physical Review A* [online]. 2008, vol. 77, no. 2, p. 021401 [visited on 2022-05-20]. ISSN 1050-2947, ISSN 1094-1622. Available from DOI: `10.1103/PhysRevA.77.021401`. arXiv:0707.1969 [quant-ph].

36. LINDENFELSER, F.; MARINELLI, M.; NEGNEVITSKY, V.; RAGG, S.; HOME, J. P. Cooling atomic ions with visible and infra-red light. *New Journal of Physics* [online]. 2017, vol. 19, no. 6, p. 063041 [visited on 2022-05-20]. ISSN 1367-2630. Available from DOI: `10.1088/1367-2630/aa7150`. arXiv:1611.08414 [physics, physics:quant-ph].

37. ROOS, C. F.; CHWALLA, M.; MONZ, T.; SCHINDLER, P.; KIM, K.; RIEBE, M.; BLATT, R. QUANTUM INFORMATION PROCESSING AND RAMSEY SPECTROSCOPY WITH TRAPPED IONS. In: *Laser Spectroscopy* [online]. Telluride, Colorado, USA: WORLD SCIENTIFIC, 2008, pp. 53–62 [visited on 2022-05-20]. Available from DOI: 10.1142/9789812813206_0005.

38. STEVENS, D.; BROCHARD, J.; STEANE, A. M. Simple experimental methods for trapped ion quantum processors. *Physical Review A* [online]. 1998, vol. 58, no. 4, pp. 2750–2759 [visited on 2022-06-20]. ISSN 1050-2947, ISSN 1094-1622. Available from DOI: 10.1103/PhysRevA.58.2750. arXiv:quant-ph/9802058.

39. SCHMIDT-KALER, F.; ROOS, Ch; NAEGERL, H. C.; ROHDE, H.; GULDE, S.; MUNDT, A.; LEDERBAUER, M.; THALHAMMER, G.; ZEIGER, Th; BARTON, P.; HORNEKAER, L.; REYMOND, G.; LEIBFRIED, D.; ESCHNER, J.; BLATT, R. Ground state cooling, quantum state engineering and study of decoherence of ions in Paul traps. *Journal of Modern Optics* [online]. 2000, vol. 47, no. 14-15, pp. 2573–2582 [visited on 2022-06-20]. ISSN 0950-0340, ISSN 1362-3044. Available from DOI: 10.1080/09500340008232182. arXiv:quant-ph/0003096.

40. RAAB, Ch; ESCHNER, J.; BOLLE, J.; OBERST, H.; SCHMIDT-KALER, F.; BLATT, R. Motional sidebands and direct measurement of the cooling rate in the resonance fluorescence of a single trapped ion. *Physical Review Letters* [online]. 2000, vol. 85, no. 3, pp. 538–541 [visited on 2022-06-20]. ISSN 0031-9007, ISSN 1079-7114. Available from DOI: 10.1103/PhysRevLett.85.538. arXiv:quant-ph/0003009.

41. MORIGI, G.; ESCHNER, J.; CIRAC, J. I.; ZOLLER, P. Laser Cooling of two trapped ions: Sideband cooling beyond the Lamb-Dicke limit. *Physical Review A* [online]. 1999, vol. 59, no. 5, pp. 3797–3808 [visited on 2022-06-20]. ISSN 1050-2947, ISSN 1094-1622. Available from DOI: 10.1103/PhysRevA.59.3797. arXiv:quant-ph/9812014.

42. HAMANN, S. E.; HAYCOCK, D. L.; KLOSE, G.; PAX, P. H.; DEUTSCH, I. H.; JESSEN, P. S. Resolved-sideband Raman cooling to the ground state of an optical lattice. *Physical Review Letters* [online]. 1998, vol. 80, no. 19, pp. 4149–4152 [visited on 2022-06-20]. ISSN 0031-9007, ISSN 1079-7114. Available from DOI: 10.1103/PhysRevLett.80.4149. arXiv:quant-ph/9801025.

43. KHAYKOVICH, L.; FRIEDMAN, N.; BALUSCHEV, S.; FATHI, D.; DAVIDSON, N. High sensitivity two-photon spectroscopy in a dark optical trap, based on electron shelving [online]. 1999 [visited on 2022-06-20]. Available from DOI: 10.48550/arXiv.physics/9912002. Number: arXiv:physics/9912002 arXiv:physics/9912002.

44. DEMTRODER, W. *Laser Spectroscopy* [online]. [N.d.] [visited on 2022-05-30]. Available from: https://link.springer.com/book/10.1007/978-3-662-05155-9.

45. *SOLSTIS TITAN | SolsTiS | M Squared* [online]. [N.d.] [visited on 2022-06-22]. Available from: https://www.m2lasers.com/solstis-titan.html.

46. SHANK, C. V.; IPPEN, E. P. Subpicosecond kilowatt pulses from a mode-locked cw dye laser. *Applied Physics Letters* [online]. 1974, vol. 24, no. 8, pp. 373–375 [visited on 2022-06-22]. ISSN 0003-6951. Available from DOI: 10.1063/1.1655222. Publisher: American Institute of Physics.

47. VALDMANIS, J. A.; FORK, R. L.; GORDON, J. P. Generation of optical pulses as short as 27 femtoseconds directly from a laser balancing self-phase modulation, group-velocity dispersion, saturable absorption, and saturable gain. *Optics Letters* [online]. 1985, vol. 10, no. 3, pp. 131–133 [visited on 2022-06-22]. ISSN 1539-4794. Available from DOI: 10.1364/OL.10.000131. Publisher: Optica Publishing Group.

48. LITTMAN, Michael G. Novel geometry for single-mode scanning of tunable lasers. *Optics Letters* [online]. 1981, vol. 6, no. 3, pp. 117–118 [visited on 2022-05-30]. ISSN 1539-4794. Available from DOI: 10.1364/OL.6.000117. Publisher: Optica Publishing Group.

49. TOPTICA. *TA pro* [online]. [N.d.] [visited on 2022-06-03]. Available from: https://www.toptica.com/products/tunable-diode-lasers/amplified-lasers/ta-pro.

50. TORRES-COMPANY, Victor; WEINER, Andrew M. Optical frequency comb technology for ultra-broadband radio-frequency photonics. *Laser and Photonics Reviews* [online]. 2014, vol. 8, no. 3, pp. 368–393 [visited on 2022-06-06]. ISSN 18638880. Available from DOI: 10.1002/lpor.201300126. arXiv:1403.2776 [physics].

51. FORTIER, Tara; BAUMANN, Esther. 20 years of developments in optical frequency comb technology and applications. *Communications Physics* [online]. 2019, vol. 2, no. 1, p. 153 [visited on 2022-06-19]. ISSN 2399-3650. Available from DOI: 10.1038/s42005-019-0249-y. arXiv:1909.05384 [physics].

52. WEI ZHANG; LOURS, M.; FISCHER, M.; HOLZWARTH, R.; SANTARELLI, G.; COQ, Y. L. Characterizing a fiber based frequency comb with electro optic modulator. *IEEE Transactions on Ultrasonics, Ferroelectrics and Frequency Control* [online]. 2012, vol. 59, no. 3, pp. 432–438 [visited on 2022-06-06]. ISSN 0885-3010. Available from DOI: 10.1109/TUFFC.2012.2212.

53. HILWEG, Christopher; MASSA, Francesco; MARTYNOV, Denis; MAVALVALA, Nergis; CHRUSCIEL, Piotr T.; WALTHER, Philip. Gravitationally induced phase shift on a single photon. *New Journal of Physics* [online]. 2017, vol. 19, no. 3, p. 033028 [visited on 2022-06-20]. ISSN 1367-2630. Available from DOI: 10.1088/1367-2630/aa638f. arXiv:1612.03612 [quant-ph].

54. XAVIER, G. B.; WEID, J. P. von der. Stable single-photon interference in a 1 km fiber-optic Mach–Zehnder interferometer with continuous phase adjustment. *Optics Letters* [online]. 2011, vol. 36, no. 10, pp. 1764–1766 [visited on 2022-06-20]. ISSN 1539-4794. Available from DOI: 10.1364/OL.36.001764. Publisher: Optica Publishing Group.

55. STENGER, Jorn; SCHNATZ, Harald; TAMM, Christian; TELLE, Harald R. Ultraprecise Measurement of Optical Frequency Ratios. *Physical Review Letters* [online]. 2002, vol. 88, no. 7, p. 073601 [visited on 2022-05-25]. ISSN 0031-9007, ISSN 1079-7114. Available from DOI: 10.1103/PhysRevLett.88.073601.

56. TELLE, H.R.; LIPPHARDT, B.; STENGER, J. Kerr-lens, mode-locked lasers as transfer oscillators for optical frequency measurements. *Applied Physics B: Lasers and Optics* [online]. 2002, vol. 74, no. 1, pp. 1–6 [visited on 2022-05-25]. ISSN 0946-2171, ISSN 1432-0649. Available from DOI: 10.1007/s003400100735.

57. CIZEK, Martin; PRAVDOVA, Lenka; MINH TUAN, Pham; LESUNDAK, Adam; HRABINA, Jan; LAZAR, Josef; PRONEBNER, Thomas; AEIKENS, Elke; PREMPER, Jorg; HAVLIS, Ondrej; VELC, Radek; SMOTLACHA, Vladimir; ALTMANNOVA, Lada; SCHUMM, Thorsten; VOJTECH, Josef; NIESSNER, Anton; CIP, Ondrej. Coherent fibre link for synchronization of delocalized atomic clocks. *Optics Express* [online]. 2022, vol. 30, no. 4, p. 5450 [visited on 2022-05-20]. ISSN 1094-4087. Available from DOI: 10.1364/OE.447498.

58. SCHARNHORST, Nils; WÜBBENA, Jannes B.; HANNIG, Stephan; JAKOBSEN, Kornelius; KRAMER, Johannes; LEROUX, Ian D.; SCHMIDT, Piet O. High bandwidth transfer of phase stability through a fiber frequency comb. *Optics Express* [online]. 2015, vol. 23, no. 15, p. 19771 [visited on 2022-05-25]. ISSN 1094-4087. Available from DOI: 10.1364/OE.23.019771.

59. YOUNG, B. C.; CRUZ, F. C.; ITANO, W. M.; BERGQUIST, J. C. Visible Lasers with Subhertz Linewidths. *Physical Review Letters* [online]. 1999, vol. 82, no. 19, pp. 3799–3802 [visited on 2022-05-20]. ISSN 0031-9007, ISSN 1079-7114. Available from DOI: 10.1103/PhysRevLett.82.3799.

60. STERR, U.; LEGERO, T.; KESSLER, T.; SCHNATZ, H.; GROSCHE, G.; TERRA, O.; RIEHLE, F. Ultrastable lasers: new developments and applications. In: IDO, Tetsuya; REID, Derryck T. (eds.) [online]. San Diego, CA, 2009, 74310A [visited on 2022-05-20]. Available from DOI: 10.1117/12.825217.

61. LEIBRANDT, David R.; THORPE, Michael J.; NOTCUTT, Mark; DRULLINGER, Robert E.; ROSENBAND, Till; BERGQUIST, James C. Spherical reference cavities for frequency stabilization of lasers in non-laboratory environments. *Optics Express* [online]. 2011, vol. 19, no. 4, p. 3471 [visited on 2022-05-20]. ISSN 1094-4087. Available from DOI: 10.1364/OE.19.003471.

62. ALNIS, J; MATVEEV, A; KOLACHEVSKY, N; WILKEN, T; UDEM, Th; HANSCH, T W. Sub-Hz line width diode lasers by stabilization to vibrationally and thermally compensated ULE Fabry- Perot cavities. [N.d.], p. 18.

63. STABLE. *Home* [online]. [N.d.] [visited on 2022-07-03]. Available from: https://stablelasers.com/.

64. DREVER, R. W. P.; HALL, J. L.; KOWALSKI, F. V.; HOUGH, J.; FORD, G. M.; MUNLEY, A. J.; WARD, H. Laser phase and frequency stabilization using an optical resonator. *Applied Physics B Photophysics and Laser Chemistry* [online]. 1983, vol. 31, no. 2, pp. 97–105 [visited on 2022-05-20]. ISSN 0721-7269, ISSN 1432-0649. Available from DOI: `10.1007/BF00702605`.

65. KELLER, Jonas. Spectroscopic characterization of ion motion for an optical clock based on Coulomb crystals. [N.d.], p. 135.

66. NUMATA, Kenji; KEMERY, Amy; CAMP, Jordan. Thermal-Noise Limit in the Frequency Stabilization of Lasers with Rigid Cavities. *Physical Review Letters* [online]. 2004, vol. 93, no. 25, p. 250602 [visited on 2022-05-20]. ISSN 0031-9007, ISSN 1079-7114. Available from DOI: `10.1103/PhysRevLett.93.250602`.

67. SIEGMAN, A. E. *Lasers*. Mill Valley, Calif.: University Science Books, 1986. OCLC: 14525287.

68. *Gaussian, Hermite-Gaussian, and Laguerre-Gaussian beams: A primer* [online]. 2004 [visited on 2022-06-19]. Available from DOI: `10.48550/arXiv.physics/0410021`. Number: arXiv:physics/0410021 arXiv:physics/0410021.

69. VAN ZEE, Roger D.; LOONEY, J. Patrick. *Cavity-enhanced spectroscopies*. Amsterdam: Academic Press, 2002. Experimental methods in the physical sciences, no. 40. ISBN 978-0-12-475987-9.

70. ENDO, Mamoru; SCHIBLI, Thomas R. Residual phase noise suppression for Pound-Drever-Hall cavity stabilization with an electro-optic modulator. *OSA Continuum* [online]. 2018, vol. 1, no. 1, p. 116 [visited on 2022-06-20]. ISSN 2578-7519. Available from DOI: `10.1364/OSAC.1.000116`.

71. BLACK, Eric D. An introduction to Pound–Drever–Hall laser frequency stabilization. *American Journal of Physics* [online]. 2001, vol. 69, no. 1, pp. 79–87 [visited on 2022-06-20]. ISSN 0002-9505, ISSN 1943-2909. Available from DOI: `10.1119/1.1286663`.

72. BITOU, Youichi. High-accuracy displacement metrology and control using a dual Fabry-Perot cavity with an optical frequency comb generator. *Precision Engineering* [online]. 2009, vol. 33, no. 2, pp. 187–193 [visited on 2022-06-20]. ISSN 01416359. Available from DOI: `10.1016/j.precisioneng.2008.05.004`.

73. BRIMROSE. *Brimrose Corp.* [Online]. [N.d.] [visited on 2022-06-16]. Available from: `https://www.brimrose.com`.

74. FOX, Richard W. Temperature analysis of low-expansion Fabry-Perot cavities [online]. 2009, vol. 17, no. 17, pp. 15023–15031 [visited on 2022-06-16]. Available from: `https://www.nist.gov/publications/temperature-analysis-low-expansion-fabry-perot-cavities`. Last Modified: 2017-02-19T20:02-05:00.

75. RAMSEY, Norman F. A New Molecular Beam Resonance Method. *Physical Review* [online]. 1949, vol. 76, no. 7, pp. 996–996 [visited on 2022-05-20]. Available from DOI: `10.1103/PhysRev.76.996`. Publisher: American Physical Society.

76. RAMSEY, Norman F. A Molecular Beam Resonance Method with Separated Oscillating Fields. *Physical Review* [online]. 1950, vol. 78, no. 6, pp. 695–699 [visited on 2022-06-27]. Available from DOI: `10.1103/PhysRev.78.695`. Publisher: American Physical Society.

77. SCHMIDT-KALER, F; GULDE, S; RIEBE, M; DEUSCHLE, T; KREUTER, A; LANCASTER, G; BECHER, C; ESCHNER, J; H FFNER, H; BLATT, R. The coherence of qubits based on single Ca ions. *Journal of Physics B: Atomic, Molecular and Optical Physics* [online]. 2003, vol. 36, no. 3, pp. 623–636 [visited on 2022-05-20]. ISSN 0953-4075. Available from DOI: `10.1088/0953-4075/36/3/319`.

78. ALLAN, D.W. Statistics of atomic frequency standards. *Proceedings of the IEEE* [online]. 1966, vol. 54, no. 2, pp. 221–230 [visited on 2022-06-26]. ISSN 0018-9219. Available from DOI: `10.1109/PROC.1966.4634`.

79. LESUNDAK, Adam; PHAM, Tuan M.; CIZEK, Martin; OBSIL, Petr; SLODICKA, Lukas; CIP, Ondrej. Optical frequency analysis on dark state of a single trapped ion. *Optics Express* [online]. 2020, vol. 28, no. 9, pp. 13091–13103 [visited on 2022-05-31]. ISSN 1094-4087. Available from DOI: `10.1364/OE.389411`. Place: Washington Publisher: Optical Soc Amer WOS:000530854700045.

Appendix I

Key publications and my contribution

Here is a list of the first- and co-authored publications included in the doctoral thesis, together with my contribution to each article.

- **Research article 1** (page 83)

A room-temperature ion trapping apparatus with hydrogen partial pressure below 10^{-11} mBar

P. Obšil, A. Lešundák, <u>T. Pham</u>, K. Lakhmanskiy, L. Podhora, M. Oral, O. Číp, and L. Slodička

Contribution:

- I participated in preparing, cleaning and assembly of vacuum apparatus.
- I participated in preparing and assembly of apparatus for loading and trapping ion.
- I prepared and build an optical path for ionisation lasers.
- I prepared and build an optical path for Doppler lasers.
- I prepared and build an optical path for spectroscopy laser.
- I participated in building an optical path for fluorescence detection.
- I controlled and managed technical support during measurements.
- I prepared and participated in measurements.
- I participated in editing the manuscript.

- **Research article 2** (page 91)

Optical frequency analysis on dark state of a single trapped ion

A. Lesundak, T. M. pham, M. Cizek, P. Obsil, L. Slodicka, and O. Cip

Contribution:

- I controlled and managed technical support during measurements.
- I prepared and build an optical path for Doppler lasers.
- I prepared and participated in measurements.
- I participated in processing the data.
- I participated in editing the manuscript.

- **Research article 3** (page 105)

Frequency stabilisation of 729 nm external cavity diode laser with a combined approach using the high finesse cavity and transfer oscillator technique

<u>M. T. Pham</u>, M. Cizek, A. Lesundak, A. Kovalenko, P. Obsil, P. Jedlicka, L. Slodicka and O. Cip

Contribution:

- I cleaned and put together the vacuum setup for HF-cavity C729.
- I designed and put together an optical setup for locking the laser to HF-cavity.
- I put together isolation elements, designed and and build an insulation box.
- I designed and put together a water cooling system.
- I participated in cleaning and assembling a vacuum setup for HF-cavity c1540.
- I participated in assembling of optical setup for mode-matching the laser to HF-cavity.
- I designed and put together an optical path for Doppler lasers.
- I designed and build an electro-optical setup for spectroscopy laser.
- I designed and build an electro-optical setup for interaction with the trapped ion.
- I designed and build an electro-optical setup for fiber noise cancellation.
- I designed the experiment with trapped and cooled ion, measured and analyzed the data.

Appendix II

Commentary on key-publications

Here are a commentary on key-publications included in the doctoral thesis

Developing and building a new functional infrastructure for spectroscopy on the trapped and cooled ion is tremendous and adventurous work. It requires knowledge from many fields and a fair amount of dedication work. However, the fruit of this work is harvested many times in the form of a highly specialised and precise tool that allows us to observe an otherwise hidden scientific phenomenon. In this chapter, I would like to present three scientific articles that show the results we have achieved thanks to this infrastructure.

Research article 1 focuses on designing and assembling an apparatus that will serve for ion trapping and storing. An ultra-high vacuum (UHV) is necessary to isolate the ion from the laboratory environment and is crucial for any experiments involving ground state cooling. Suppose the one finds himself that the pressure is not sufficient. In that case, it is labouring to disassemble the whole apparatus and get through a cleaning process again. For these reasons, the techniques to achieve an ultra-high vacuum are continuously revisited and improved by many laboratories.

This article presents our procedure for building a UHV apparatus containing a quadruple linear trap for storing the $^{40}Ca^+$ ions. The first part focuses on vacuum components, cleaning, and outgassing the apparatus. The resulting pressure level corresponds, to our best knowledge, to one of the best results achieved in non-cryogenic vacuum apparatus. Embraced by this result, we estimate the partial pressure by measuring the reaction rates of the long $^{40}Ca^+$ ion string with a hydrogen background gas (BG).

The main chamber and the adjacent parts are made from stainless steel SS 316 LN. We prefered this alloy due to its relatively low magnetic permeability, which helps to minimise an unwanted magnetic field affecting the trapping region. The vacuum pressure inside a chamber is kept by a combination of an ion pump combined with a non-evaporative getter (NEG)[1] and NEG pump[2]. Both consist of parts made from SS 304 L stainless steel. The ion pump also consists of a solid permanent magnet necessary for the operation of the pump. This magnetic part is kept as far from the trap centre as possible. Other parts contributing to the gassing of the chamber and thus the deterioration of the vacuum are viewports (fused silica), trap holder and assembly (Macor, titanium, sapphire crystal, indium). The trap electrodes are made from six titanium electrodes, four for radial confinement and two for axial confinement. The electrodes were electroplated with approx. 10 μm thick gold layer to enhance the electrical conductivity for the applied RF-drive. The electric connection is provided by oxygen-free high conductivity (OFHC) copper The. A detailed list of all components installed inside the vacuum chamber is listed in the paper.

The most crucial step is the cleaning process of the above-listed part, many of which come directly from the manufacturer without any cleaning. Each material needs to be cleaned with a specific order of chemicals and some in an ultrasound bath (US). The cleaning process consists of pre-cleaning, using detergent solutions like Simple Green®. After that, the hard cleaning step uses high-performance liquid chromatography (HPLC)

---

[1]SAES Getters, NEXTorr D 100-5.

[2]SAES Getters, CapaciTorr D 50.

grade alcohols. We summarise the whole cleaning process, including the duration of each step, in a table I. and II., see [25].

Even when the parts are properly cleaned, one just cleaned out the near-surface molecules. However, residual molecules are still embedded within the internal surface of the chamber itself. They will permeate the bulk to the surface as the vacuum increases, and the restraining pressure is removed. To deal with the outgassing of those molecules, one can establish the diffusion barrier on the surface of the chamber. This traditional method used in many laboratories is air-bake. The bake-out can be divided into three steps. We first bake out all the stained steel parts of the chamber to 400 °C for 8 hours. In the second step, the chamber is enclosed, and while the apparatus is pumped by a turbomolecular pump together with a Roots-type pre-pump system[3], the temperature is set to 270 °C for ten days. The final bake-out includes the insertion of a trapping apparatus and all the necessary parts into the chamber, and while pumping by turbomolecular pump, the whole setup was heated to 195 °C for another ten days. During the final part of the bake-out (temperature is ramped down to 45 °C, we also activate the oven consisting of neutral calcium ore and the activation of the ion pump and the NEG.

After the baking process, we close the valve separating the chamber from the pre-pump (Turbomolecular pump). Now The pressure inside the chamber is monitored by the ion pump in the form of inserted current. After approximately two hours, the current reached 0 nA. This corresponds to the pressure level below gauging capabilities, which is specified to be about $< 10^{-11}$ mBar for nitrogen gas. To be able to estimate the actual hydrogen pressure level, we carried out a measurement based on the reaction rate of the given atomic isotope with the background gas.

There are possible two interactions between the ion and a BG. One is an elastic collision, which transfers the momentum to the ion. The ion is heated up and changes its position in the crystal, or in worst cases, even leaves the trap. The inelastic collision, on the other hand, results in the formation of molecular ions.

Due to our relatively deep trap potential (approx. 3.5 eV), it is scarce to observe the direct loss of the ion. To measure the elastic collision, one then can purposely load the non-fluorescing isotope to the string. However, such a method is highly ineffective and relates to too many parameters. Due to these reasons, we focused on the second type of collision. The molecular reaction rates are highly insensitive to particular trap settings and laser cooling parameters, thus leading to relatively small systematic uncertainties of the measured pressure.

The inelastic collision rate can be estimated as

$$^{40}Ca^+(4P_{1/2}) + H_2 \rightarrow ^{40}H^+ + H. \tag{5.4}$$
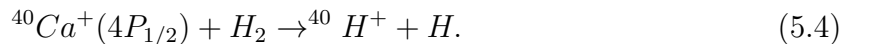
The dynamic of this reaction is

$$N(^{40}Ca^+) = N_0(^{40}Ca^+) \cdot e^{-\gamma \cdot t}, \tag{5.5}$$

---

[3]Pfeiffer Vacuum, HiCube 80 Pro/ACP 15.

where $N_0(^{40}Ca^+)$ is the number of non reacted ions at the beginning of the measurement period $t = 0$, $N(^{40}Ca^+)$ is the number of non-reacted ions after time t, γ is the reaction rate and it is equals to $p_e \cdot n_{H2} \cdot k_r$, with p_e being the probability of $4P_{1/2}$ level population, n_{H2} the number density of the H_2 gas, and k_r is the reaction rate constant.

The main experiment consists of loading a 34-ion long string. The string was Doppler cooled with 397 nm laser and 866 nm laser as a repumper. The fluorescence scattered from ions was collected by an EMCCD camera with 1.95 Hz rate and 500 ms acquisition time. The time-lapse images were processed one by one by averaging the photon counts from pixels surrounding the ion image for each ion separately. The post-processing of the 51-hour-long captured record shows the four reactions. Whenever the ion goes dark, it stays in the non-fluorescence state on a time scale of minutes before being bright again. The measurement resulted in the partial hydrogen pressure of $P_{H_2} \leq (5.5 \pm 2.8) \cdot 10^{-12}$ mBar. For a detailed description of measurement parameters and discussion, please see page 83.

Research article 2 is set to the field of high-precision sensing and spectroscopy. High precision spectroscopy is a well-developed field and is used on a daily basis by many laboratories. It is, in most cases, the essential step before performing the actual experiments. Yet it still holds immense potential for further advancement by utilisation of newly available tools for light signal generation.

In general, to be able to analyse a spectrum of optically beated signal consisting of two optical fields separated by hundreds of THz, one usually needs an optical frequency comb, which serves as a mediator of those two fields. This requirement often cannot be fulfilled due to the cost of the whole equipment. This paper proposes a method for estimating the optical frequency spectrum using the time-resolved measurement of light scattered from a single trapped $^{40}Ca^+$ ion. The interference mediated by laser-cooled atoms allows for an optical frequency beating of two optical fields. Furthermore, the sensitivity of frequency deviation is enhanced by driving the atom close to a two-photon resonance in a lambda-type energy level scheme. This atomic-level scheme enables the observation of dark states in emitted fluorescence that occurs among the vast majority o spices commonly utilised in ion trap experiments.

In the case of $^{40}Ca^+$ ion, the lasers driving this lambda-like scheme is at wavelengths 397 nm and 866 nm. The 397 nm laser serves as a Doppler cooling of the ion motion by probing the $4S_{1/2} \leftrightarrow 4P_{1/2}$ transition. The 866 nm is a repumper in case the population descend from $4P_{1/2}$ to $3D_{3/2}$. For more detailed information about $^{40}Ca^+$ level scheme, please see the Subsec. 1.3.

When both laser are detuned from the resonance state by exactly the same value $(\Delta_{866} - \Delta_{397} = 0)$, the population of the excited state $4P_{1/2}$ disappears. This corresponds to a dark state with no fluorescence emission. In practice, the dark population is limited by the finite linewidth of the two involved lasers and finite coherence between the ground state $S_{1/2}$ and $D_{3/2}$ as well as a thermal population of atomic motion.

This work aim to deliver a complete analysis of the limitation of this method. To have

a reliable and stable measuring tools We firstly phase lock both lasers to particular teeth of the fibre frequency comb, which is referenced by a hydrogen maser. With this step, the lasers will adopt the frequency stability of the OFC. Hence the linewidth of the lasers will narrow down to approx. 80 Hz (measured by beating both lasers with the OFC).

The scheme is set as follow. The measurement point, i.e. the point most sensitive to frequency deviation, is set to the middle of the slope of the dark resonance. This relatively steep (gradient of 2.2 counts $\cdot$s$^{-1}\cdot$ kHz^{-1}) linear area is ideal for frequency sensing as a slight change in frequency will result in a significant response in fluorescence intensity. The dynamic response of the ion fluorescence to the frequency detuning of the excitation laser is observed by setting the 866 nm laser as an analyser to which a deterministic frequency modulation is applied. In contrast, the 397 nm laser serves as a reference field with a fixed frequency.

We then Analyzed the fluorescence respond for various set of modulation frequencies f_m, frequency deviations A and frequency detunings $= \Delta_{866} - \Delta_{397}$. Each measurement is analysed as a signal to noise ratio (SNR) with respect to the time bin length τ. The length of individual measurements T is set to be an integer multiple of $1/f_m$, to avoid the spectral leaking in the FFT spectrum.

The first measurement focus on the influence of the modulation frequency on the SNR of the method. The SNR were systematically measured for various modulated detunings Δ_{866} in the range from 66 Hz to 120 kHz. The duration of each measurement was 300 s with a fixed deviation A of 300 kHz.

The SNR is calculated as S_m/N_m, where S_m is the FFT frequency component at the modulation frequency f_m and N_m is the average amplitude of the whole FFT spectrum except the DC component.

The resulted SNR is plotted against the gate interval τ in Fig. 4.[79]. The resulting dependence shows that a similar SNR can be achieved for modulation between 66 Hz and 6.6 kHz. Higher modulation frequencies will decrease the signal-to-noise ratio of the fluorescence intensity response.

The second measurement puts the dependency of the SNR ratio against deviation variations and different measurement lengths. The modulation frequency is kept at a fixed number, 66 Hz, to avoid any effect of fast modulation on the observability of high modulation amplitudes (see the previous measurement). The spectral width of the dark resonance slope gives the expected upper limit. At the same time, the lowest detectable modulation depths will depend on the amount of detection noise. The SNR data was measured for a set of deviation values from 10 to 1000 kHz and for measured time T, 2.5 and 500 s. The result tells us that with higher the deviation, the higher SNR will be, and the lowest detectable deviation is $A_{lim} = 68 \pm 5$ kHz. Also, an x-times lower the A one can get the same SNR value simply by prolonging the measured time by a factor x^2.

These two measurements give us a general insight into the proposed method's limitation for given frequencies. However, the whole spectrum needs to be searched when estimating the amplitude of unknown frequency. In this case, the SNR can be calculated as $SNR(T,\tau) = S_{max}/N_m$, where S_{max} is the highest amplitude component of the whole

FFT frequency spectrum except the DC component. The detectable frequency deviation limit A_{lim} of this measurement is 68 ± 5 kHz for T=5 and 8.6 ± 0.4 kHz for T = 500 s.

For the complete and detailed description of the presented method, its analysis and proposed further applications, please see page 91.

Research article 3 closely relates to the theme of the thesis. Unfortunately, at the time of this thesis, it is not yet published. The paper is already well prepared except for some minor details unrelated to the measured method or result presented in the paper. Due to those reasons, I have decided to attach it to this work.

The paper presents the latest result on the innovative stabilisation method currently used in our laboratory. The main goal of this paper is to deliver a report on the enhancement of the already existing method commonly used for stabilisation the optical frequency of the laser into a more stable reference.

For decades atomic frequency standards played a critical role in basic science and precision measurement. During this period, the increasing need for more precise timing and synchronisation for a wide range of applications, including navigation, synchronisation or test of fundamental physics, has demanded oscillators with higher frequencies and higher performance. To excite those oscillators coherently, a high spectra purity of the laser source is a crucial feature and stabilisation techniques have constantly been renewed and developed over time.

A commonly used technique is the transfer oscillator technique. The stability is transferred from an ultra-stable master source into a laser using the mediator. The main advantage of this is that one can stabilise the laser to the stable reference on different wavelengths. Also, many stabilisation stages can be built to share the one ultra-stable reference. However, due to the complexity of this technique with many wide band servo loops, it inevitably leads to transferring the residual noise accumulated in these servo bumps into the resulting laser. Those servo pumps are visible on the frequency spectra and interact with ions during the measurement. This occurs especially during the measurement when the short pulse (a few-μs) duration is required. This results in relatively high laser intensity and decreases the measurement's fidelity.

A traditional way to stabilise the optical frequency is by locking its frequency to an ultra-stable length of the high-finesse cavities. HF-cavity consists of the pair of the HR coated mirrors optically contacted to a stable spacer. The spacer delivers the primary stability of the whole system. Thus the material from which the body is made has to have a very low expansion coefficient like ULE or silicon. The quality optical cavity, also known as finesse, is calculated by the quality of the mirror coatings. The higher the reflectivity of the mirror, the longer the beam will bounce on them before it leaves the optical cavity. The main characteristic of the cavity is that its length instability is directly related to the longitudinal cavity mode. Thus they are highly selective frequency discriminators. However, the cavity is a physical component, and thus it is susceptible to environmental perturbations from which it needs to be isolated. Even well isolated, the cavity exhibit a slow drift due

to Brownian thermal motion and the ageing effect. In our case, it is approximately 0.3 Hz·s^{-1}, which reduces the laser's liability and fidelity of the measurement.

Both techniques, if used alone, have their advantages but also limitations. Whether it is instability due to drift of the cavity length and thus causes the drift of the locking point or off-resonant driving of the transition due to transferred noises from the servo loop. It continuously decreases the laser coherency and fidelity of the measurement and causes inaccuracy while determining the detuning from the resonance frequency.

We then propose combining those methods when only the best features of both methods are involved. The laser locked to the cavity will deliver the short-term stability, while the long-term stability will be achieved by implementing the virtual beat as a precise tracing and servo loop correction of the cavity drift.

The cavity installed in our laboratory (C729) is made from ULE. It is 47.65 mm long and has a finesse of 351 000. This corresponds to mode free spectral range of 3.14 GHz and a linewidth of the central mode $FHWM = 8.9$ KHz. This narrow transition provides enough room to detect laser frequency changes down to Hz. The laser is referenced to the cavity using the standard P-D-H stabilisation technique. The cavity and the necessary optic involved are enclosed into a wooden box, with various isolation elements ensuring that the cavity is isolated from thermal and vibration perturbations. For more detailed info on the setup, please see page 105.

The primary reference for the transfer oscillator technique is a stable laser (NKT Koheras Basik) working at 1540.57 nm (L1540), whose stability is transferred to spectroscopy laser working at 729 nm. A mediator of those two lasers is the OFC.

First, the L729 and L1540 lasers are individually optically beated with specific teeth of the OFC closest to their optical frequencies. We will name indices of those teeth as N_{729} and N_{1540}

frequency deviations observed between the $N_{1540}{}^{th}$ tooth and L1540 relate to observed deviations between L729 and the $N_{729}{}^{th}$ tooth. This relationship can be expressed as $\Delta\nu_{L729} = \Delta\nu_{L1540} \cdot N_{729}/N_{1540}$.

To subtract this frequency noise from the L729 beat, the beat signal of L1540 is frequency multiplied by the ratio of N_{729}/N_{1540} using a direct digital synthesiser (DDS) Chap. 4 and then mixed with the L729 beat. Since the f_{ceo} lock of the OFC has its bandwidth limited by approx. 9 kHz, there is some non-negligible residual frequency noise originating from the OFC pump laser present at higher Fourier frequencies of the f_{ceo} signal. This frequency noise is present in the L729 beat as well. The f_{ceo} signal from the OFC is thus used for subtracting this frequency noise from the L729 beat note. After frequency multiplying the f_{ceo} signal appropriately by another DDS and mixing it with the L729 resulting in a virtual "transfer beat". This signal is independent to both f_{rep} and f_{ceo}. This signal is used as a precise tracking oscillator to compensate for the cavity drift.

We demonstrate the practical impact of this stabilisation setup by performing a coherent manipulation on the $|^2S_{1/2}, m = -1/2\rangle \leftrightarrow |^2D_{5/2}, m = -1/2\rangle$ narrow transition of the $^{40}Ca^+ion$. The finite laser coherence value was then estimated through a Ramsey

separated oscillating field method. The resulting laser linewidth is calculated from the fit over the set of measured Ramsey contrasts. Our implementation results in Ramsey time of 7.64, correspond to laser linewidth μs $\Delta_{\nu_{FWHM}} = 28.9$ Hz. This is near twice the improvement compared to when the virtual beat signal is directly used in a wide band servo loop for locking the L729 to L1540.

Many experiments demand a pulse's length in a few milliseconds range. In this regime, the power broadening caused by high laser power operation can magnify the residual noises that are contained in the spectra. However, in this case, the only wide band servo loop is the P-D-H lock with a bandwidth of a few kHz. Thus the higher frequency noises are suppressed. This is demonstrated in the measured transition spectra of the ion. The fidelity obtained using our method is 99%. In contrast, we add the same spectral line scanned with the L729 locked only to the virtual beat in a wide-band servo loop. One can see that the spectrum also contains the residual noises from the servo, visible thanks to power broadening. The excitation contrast is limited to 94%. In both cases, the laser intensity was stabilised so that the π pulse remains 25 μs.

Appendix III

Key-publications reprints

Here are attached key-publications

Research article 1

A room-temperature ion trapping apparatus with hydrogen partial pressure below 10^{-11} mBar

P. Obšil, A. Lešundák, T. Pham, K. Lakhmanskiy, L. Podhora, M. Oral, O. Číp, and L. Slodička

A room-temperature ion trapping apparatus with hydrogen partial pressure below 10^{-11} mBar

P. Obšil,[1] A. Lešundák,[2] T. Pham,[2] K. Lakhmanskiy,[3] L. Podhora,[1] M. Oral,[2] O. Číp,[2] and L. Slodička[1, a)]

[1)]*Department of Optics, Palacký University, 17. listopadu 12, 771 46 Olomouc, Czech Republic*

[2)]*Institute of Scientific Instruments of the Czech Academy of Sciences, Královopolská 147, 612 64 Brno, Czech Republic*

[3)]*Institut für Experimentalphysik, Universität Innsbruck, Technikerstraße 25, 6020 Innsbruck, Austria*

(Dated: 3 December 2019)

The lifetime of trapped ion ensembles corresponds to a crucial parameter determining the potential scalability of their prospective applications and is often limited by the achievable vacuum level in the apparatus. We report on the realization of a room-temperature ^{40}Ca$^+$ ion trapping vacuum apparatus with unprecedentedly low reaction rates of ions with a dominant vacuum contaminant: hydrogen. We present our trap assembly procedures and hydrogen pressure characterization by analysis of the CaH$^+$ molecule formation rate.

I. INTRODUCTION

Experimental platforms utilizing controllable electric potentials for storing several charged atomic particles have become pivotal in several modern research fields, including precision metrology, sensing, or quantum information processing[1–3]. Besides representing a pioneering platform for tests of a large number of advanced applications of quantum optics phenomena, they have also provided an indispensable resource for fundamental studies of atomic structure and its interaction with electromagnetic radiation. Dozens of experimental research groups worldwide utilize atomic ion traps as the main experimental platform and several efforts for the development of standardized technological substances with the possibility of involving automated industrial processing have emerged in past few years[4,5]. One of the crucial technological challenges in process of realization of ion trapping apparatus corresponds to establishing sufficient vacuum environment in the trapping region. The achieved vacuum pressure is proportional to the mean free path of residual atomic particles, which in turn determines the achievable lifetime of the trapped ionic system. The collisions with the background gases can lead to thermalization of ions and their crystalized spatial structures, chemical reactions, or even direct ejection of ions from the trapping potential[6,7]. Vacuum quality can thus directly limit performed experiments and impose requirements on frequent ion reloading in some of the most advanced branches of ion trapping applications which involve large numbers of ions[3,8–15].

The target vacuum pressures suitable for trapping single atomic ions or small ion crystals are in the ultra-high-vacuum (UHV) regime, well below 10^{-9} mBar[7,16]. Demands on the feasibility of scaling up the number of trapped ions further substantially decrease the required values of vacuum pressure levels, as the number of collisions scales linearly with the number of trapped ions. For thoroughly cleaned and well-baked chambers pre-pumped with a turbomolecular pump, the limiting residual element with highest partial pressure corresponds to a hydrogen due to its large concentration in stainless steel and high diffusion rate[17]. The chemical reactions of hydrogen with various atomic ion species were formerly studied due to their creation feasibility and suitability for studies of ultracold ion chemistry[18,19], direct or sympathetic laser cooling[20–24], proposed as sensitive probes of fundamental theories[25], or considered as astrophysically important molecules[26].

Here we present our procedure of building an UHV apparatus containing a linear Paul trap for spatial localization of ^{40}Ca$^+$ ions and estimation of the achieved hydrogen pressure using the measurement of the molecular reaction rates. The first part summarizes the particular employed procedures of vacuum chamber assembly, which are, up to small differences, well established in the experimental quantum optics community working with trapped cold atoms or ions. The resulting vacuum pressure level corresponds, to our best knowledge, to one of the best values reached in non-cryogenic vacuum apparatus in experimental trapped ion research and therefore we focus on the rigorous estimation of the pressure of the residual gas with the highest partial pressure corresponding to hydrogen molecules. The pressure is gauged by ^{40}Ca$^+$ ion crystal by measurement and evaluation of reaction rates with the hydrogen background gas. The conclusion includes a comparison of presented results with recent works focused on the estimation of vacuum pressures from observable interaction rates of trapped ions with background gas.

II. VACUUM CONSTRUCTION

The presented vacuum chamber is composed of and contains solely UHV compatible materials with low outgassing rates. The vacuum chamber and employed vacuum flanges are made from stainless steel SS 316 LN with low relative magnetic permeability in order to minimize unknown magnetic field gradients across the trapping region. For the same reason, all stainless steel components of the trap and its holder which mainly correspond to small screws are also made from SS 316 LN. The only exception corresponds to the combined

---

vacuum pump (SAES group, NEXTorr® D 100-5), which has SS 304 parts and includes a permanent magnet necessary for the operation of the ion pump, however, its position within the chamber corresponds to the largest distance to the trap. In addition to stainless steel, the large surface of the chamber is employed for optical access using a fused silica vacuum viewports with a broadband anti-reflection coatings covering 397 to 850 nm range. The trap and ion source assembly further contain Macor®, titanium, sapphire crystal, and an indium sealed source of calcium atoms. The trap electrodes are connected to oxygen-free high conductivity (OFHC) copper feedthroughs using an OFHC copper conductors and additional wires with Kapton® isolation were used for the connection of the in-vacuum thermistor. Several parts were silver-plated, which included chamber assembly screws and majority of the OFHC copper gaskets. The total volume of the vacuum chamber has been estimated to approximately 1.6 litres.

The Paul trap itself is formed by six titanium electrodes, four radial and two axial, and additional two pairs of SS 316 LN stainless steel micro-motion compensation electrodes[27]. All titanium electrodes were electroplated by approximately 10 μm thick gold layer to avoid any oxidized surfaces in the proximity of the trapping potential and, at the same time, enhance the electrical conductivity for the applied radio-frequency drive, which in turn results in lower temperature of the trap due to suppressed electric power dissipation. Before the electroplating, electrodes were cleaned in an ultrasonic bath with acetone and methanol, respectively. Subsequently, hydrogen fluoride was used to remove native titanium oxide. All etched parts were stored in the water in order to slow down any further oxidation. A gold sulfite electroplating solution TSG-250 heated to 60°C was used for creation of satin-smooth electrodeposits on the titanium surface. The endcap electrodes were electroplated with 10 mA current for 40 minutes and radial electrodes with 5 mA for 30 minutes. The achieved gold surface has a low roughness with grain size of less than a micron in diameter. The trap design corresponds to ion to radial electrodes and ion to axial electrodes distances of 566 μm and 2250 μm, respectively. We note that the measured heating rates with single ^{40}Ca^{+} ion using the thermometry on the $4S_{1/2} \leftrightarrow 3D_{5/2}$ transition in the final assembled setup are 5.1 ± 0.4 phonon/s for the axial motion at 1.2 MHz.

Besides choosing the appropriate UHV compatible materials, the crucial point in the process of building any UHV vacuum chamber is cleanliness. Outgassing will play an important role below pressure levels of 10^{-6} mBar and potential residual organic compounds can limit the achievable vacuum pressure. During the whole cleaning and assembling process we were strictly using cleanroom suits, nitril powder free gloves certified for clean room applications, hair nets and anti-dust mouth masks. The setup was assembled in the regular optical laboratory inside a flow box employing the filter of class H13 of norm EN 1822. The parts of the vacuum chamber and pumping station assembly were cleaned in the ultrasonic (US) bath with industrial detergents, demineralized (DM) water and high-performance liquid chromatography (HPLC) grade alcohols, respectively. For the sake of comprehensiveness and repeatability, we specify the employed cleaning procedure in

Table I. The in-vacuum parts made from an OFHC copper

TABLE I. Overview of the general cleaning procedure used mainly for stainless steel parts.

1.	10 min. in US bath in 5% Simple Green®
2.	Rinse under DM water to get rid of the detergent
3.	5 min. in US bath in DM water
4.	Quick rinse (~10 s) under DM water
5.	10 min. in US bath in HPLC Aceton
6.	Quick rinse (~10 s) under DM water
7.	10 min. in US bath in HPLC Methanol

tend to quickly oxidize on the surface when exposed to air and the oxide layers were removed by etching in diluted citric acid contained in industrial detergent Citranox®. The cleaned surface oxidizes fast in wet environment and it is important to avoid any contact with water or long exposure to air after final cleaning. Note that the employed cleaning procedure for copper parts presented in Tab. II avoids the Aceton cleaning[28]. We didn't use any ultrasonic bath (US) cleaning for the em-

TABLE II. Overview of the copper cleaning procedure.

1.	10-15 min. in US bath in 2% Citranox®
2.	Rapid (~2 s) rinse under DM water to get rid of the detergent and immediate submerge into HPLC Isopropyl alcohol
3.	10 min. in US bath in HPLC Isopropyl alcohol
4.	10 min. in US bath in HPLC Methanol

ployed vacuum chamber, electrical feedthroughs, and optical viewports, as they were specified to be clean upon delivery and so we just wiped them with HPLC methanol before the assembly. The gold-plated trap electrodes were merely submerged in the methanol bath. The thoroughly cleaned parts were always stored exclusively in flowbox during the periods of assembly procedures.

Four different vacuum pumps were employed for the achievement of the resulting UHV pressures. Outside the vacuum chamber, a turbomolecular pump together with a Roots type pre-pump delivered as a single vacuum system (Pfeiffer Vacuum, HiCube 80 Pro/ACP 15) were used for reaching the UHV levels before activation of the entrapment pumps inside the chamber. The pumps in the vacuum chamber correspond to an ion pump combined with non-evaporative getter (NEG) pump (SAES Getters, NEXTorr® D 100-5) and single NEG pump (SAES Getters, CapaciTorr® D 50) positioned in the proximity of the ion trapping region at 55 mm distance, see Fig. 1.

The vacuum level in a properly cleaned and outgassed apparatus is typically determined by hydrogen partial pressure, which diffuses through and from bulk stainless steel[17,29]. The conventional method of dealing with outgassing of hydrogen is based on establishment of a diffusion barrier on the surface of the stainless steel parts by an air-baking[30]. It has been predicted and observed that even small coating defects of the oxidized stainless steel flanges can lead to a lateral diffusion and outgassing of a hydrogen atoms into the chamber[31]. The
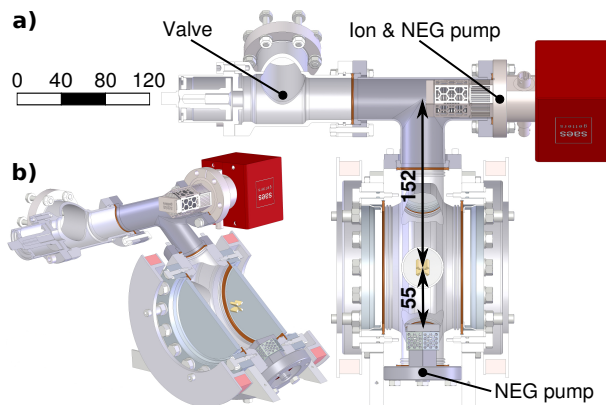
FIG. 1. A 3D-views of the employed vacuum chamber depict the relative positioning of the ion trap, entrapment pumps, and vacuum valve. a) The side-top projection with spatial scale in millimeters. b) The rotated perspective for illustration of the overall structure of the vacuum chamber.

air-bake in a clean oven was realized after cleaning procedure with all stainless steel parts including the chamber, blank flanges, reduction and T-shape pipe[30]. The temperature was ramped up at a rate of 1°C per minute to 400°C, where it was maintained for 8 hours and afterwards ramped down at the same rate to reach room temperature. The air-bake resulted in **a** visible golden colour of the stainless steel surface corresponding to chromium-oxide. A second baking step with simultaneous pumping of the preassembled chamber has been realized in order to outgas the hydrogen and water as much as possible before the final assembly. The chamber was assembled with blank stainless steel flanges instead of viewports and the entrapment pumps and Paul trap were not installed, which allowed baking of the chamber at 270 °C. After approximately one hour from the beginning of the pumping, a sufficiently low pressure had been established to perform a helium leak test which showed no detectable leaks. The ramp up and down speed of the temperature in the oven was set to the rate 15°C per hour and the system was pumped at 270 °C for 228 hours. During the whole baking time the partial gas pressures were monitored using the residual gas analyser (RGA) and a substantial decrease of the most prominent residual compounds, including predominant hydrogen, nitrogen, water, methanol and carbon dioxide, was observed. It is recommended to fill your vacuum system with pure nitrogen gas or at least dry air when opening the vacuum chamber, because outgassing of nitrogen is much easier than water adsorbed from humid air. The controlled filling of the chamber by high grade nitrogen also helps to avoid the risk of its contamination. The third baking included the final assembly of ion trapping apparatus and its temperature was limited by optical viewports to 200°C. Similarly as in the second baking stage, the helium leak test has been performed soon after starting the pumping procedure and then the temperature inside the baking oven was ramped up at a rate of 15 °C per hour to the target temperature of 195 °C where it stayed for

10 days. The ramp down at the same rate has been targeted to 45 °C at which the ion pump magnets were attached and the pump was running for 1 minute for degassing. After removal of the magnets, the atomic oven containing calcium metal powder originally closed under an argon atmosphere and sealed with indium plug was heated for 2 minutes to degas. Last procedure realized inside the baking oven was the activation of NEG pumps using the original commercial driving units. One of the NEGs was first started in the conditioning regime to avoid a rapid increase of pressure in the chamber and after about 2 minutes also the conditioning of the second NEG pump was switched on. The actual pressure was observed on RGA and after 15 minutes the full activation power was switched on for the first NEG pump and with a 2 minutes delay also the second. Both NEG pumps were activated for 1 hour and after that, both driving units and baking oven were switched off. After thermalization of the NEG pumps, the ion pump was switched on and the valve between chamber and turbomolecular pump was closed a few minutes afterwards, while the chamber temperature being still at about 40 °C.

The last partial pressures before the valve closure estimated at RGA were signifying the dominant residual gas being hydrogen with the partial pressure of $(4.62 \pm 0.05) \cdot 10^{-8}$ mBar followed by more than an order of magnitude lower population of nitrogen/carbon monoxide $(1.5 \pm 0.2) \cdot 10^{-9}$ mBar, carbon dioxide $(1.3 \pm 0.2) \cdot 10^{-9}$ mBar, water $(1.0 \pm 0.2) \cdot 10^{-9}$ mBar and methanol $(6 \pm 2) \cdot 10^{-10}$ mBar, with the rest of the residuals being below the noise floor of the RGA at about $2 \cdot 10^{-10}$ mBar level. The valve closure has resulted in a step increase of hydrogen pressure on RGA outside the chamber, which was the clear sign of its pumping by NEGs. The current on the ion pump monitor decreased quickly and after approximately two hours it showed solely 0 nA corresponding to the pressure level below its gauging capabilities, which is specified to be limited to about $< 10^{-11}$ mBar for nitrogen gas.

III. ESTIMATION OF THE HYDROGEN PRESSURE

The attainable information about the pressure level inside the chamber using the ion pump gauge is rough and gives limited knowledge about the quality of achieved vacuum. Unfortunately, it corresponds to the only available instrument for vacuum pressure estimation in our setup, similarly as for most of apparatus in the ion trapping community. The basic technical prerequisite for operation of many trapped ion experiments is the sufficiently long lifetime of the laser-cooled crystallized ion ensemble, which is typically limited by the surrounding vacuum level, laser cooling efficiency, or physical properties of the particular employed trap. The dependence of the ion crystal lifetime on the vacuum level can be in turn used for the precise estimation of the vacuum level and, together with the knowledge of particular reaction rate constants of given atomic isotope with prominent vacuum contaminants, serve also for the residual gas analysis. The conventional methods for vacuum pressure analysis using trapped atomic ions are based on estimation of rates of two types of interaction with

background gas. One is corresponding to inelastic collisions leading to the formation of molecular ions[7], and the other is involving the elastic momentum transfer, which can result in an exchange of ion positions, rapid thermalization of ion crystal, or even loss of ions from the trap[32]. The relatively high depth of our trapping potential estimated at 3.5 eV prevents a direct escape of ions and we do not observe any ion loss in usual experimental settings. At the same time, unambiguous measurement of ion crystal thermalization rates can be tricky due to short Doppler re-cooling times. For these reasons, elastic collision rates with background gas are typically measured by observation of crystal structure changes with one or more non-fluorescing ions purposely loaded in the string[32,33]. However, such method is highly dependent on particular trapping parameters which determine the potential barrier between observed crystal orders, electric field noise properties, or motional state of ions and probability of thermal activation of position flips[7,32]. On the other hand, the vacuum analysis based on the observation of molecular reaction rates is highly insensitive to particular trapping and laser cooling settings and can thus lead to smaller systematic uncertainties of the estimated pressures, provided that the type of the molecular association reaction and corresponding rate coefficients are well known.

The presented vacuum chamber contains $^{40}Ca^+$ ion trapping apparatus and the hydrogen partial pressure can thus be estimated by measurement of the rate of the reaction[19,20]

$$^{40}Ca^+(4P_{1/2}) + H_2 \rightarrow {}^{40}CaH^+ + H, \tag{1}$$
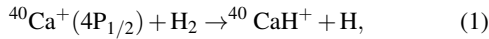
with its dynamics given by

$$N(^{40}Ca^+) = N_0(^{40}Ca^+) \cdot e^{-\gamma \cdot t}. \tag{2}$$

Here, γ is the reaction rate, $N_0(^{40}Ca^+)$ is the number of non-reacted ions at the beginning of the measurement period $t = 0$, and $N(^{40}Ca^+)$ is the number of non-reacted ions after time t. The reaction rate $\gamma = p_e n_{H_2} k_r$, with p_e being the probability of $4P_{1/2}$ level population, n_{H_2} the number density of the H_2 gas, and k_r is the reaction rate constant.

We trap linear $^{40}Ca^+$ ion strings in the installed linear Paul trap operated with 30.2 MHz radio-frequency drive and 3 W power resulting in radial center of mass motional frequencies of $f_x \approx f_y \approx 1.86$ MHz. The axial potential is set for optimizing the stability of the employed linear ion string, which for the hydrogen pressure analysing measurements with 34 ions corresponds to the center of mass mode frequency $f_z \approx 91$ kHz and $U_{tip} = 8$ V. The micromotion has been carefully optimized for employed trapping potential settings. The Doppler cooling of ions is realized by a 397 nm laser red detuned from the $4S_{1/2} \leftrightarrow 4P_{1/2}$ transition and additional 866 nm laser beam is used for depopulation of the metastable $3D_{3/2}$ manifold, see Fig. 2-a). The 854 nm laser beam set to the $3D_{5/2} \leftrightarrow 4P_{3/2}$ transition resonance is used for depopulation of the $3D_{5/2}$ level, which is populated by extremely rare events corresponding to 397 nm laser excitation of the $4S_{1/2} \leftrightarrow 4P_{3/2} \leftrightarrow 3D_{5/2}$ Raman transition. The 397 nm fluorescence scattered from ions in the direction perpendicular to the symmetry axis of the employed linear Paul trap is collected by a lens positioned outside the vacuum chamber and observed on EMCCD camera. The measured fluorescence emission spectrum with four
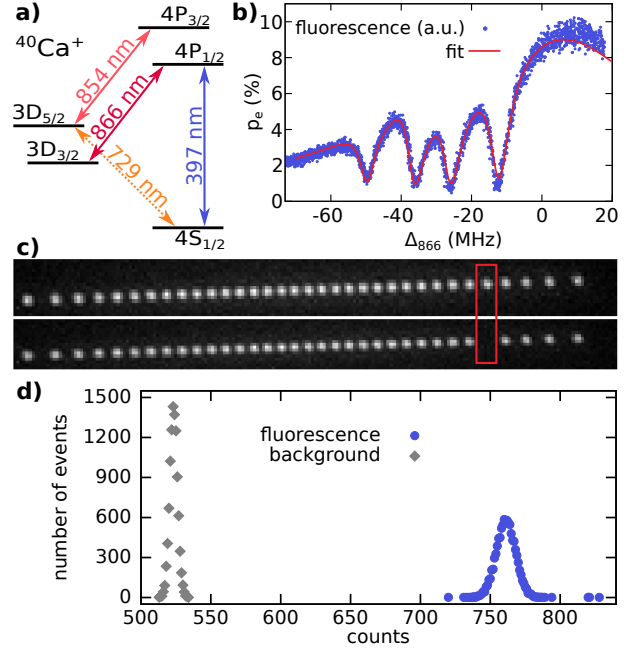

FIG. 2. a) A simplified energy level scheme of $^{40}Ca^+$ with corresponding excitation laser wavelengths. b) Measured and fitted fluorescence spectra as a function of the repumping 866 nm laser detuning for calibration of the $4P_{1/2}$ state population and corresponding detected EMCCD camera intensity. c) The representative images from EMCCD camera showing full 34 ion string (top), and the rare event of string with a single ion becoming non-fluorescing due to the chemical reaction (bottom). d) The evaluated number of detection events with measured intensities of detected fluorescence for the outermost ion in the 34-ion string. The histogram is evaluated from 10^4 measurements on the EMCCD camera, each with an acquisition time of 0.5 s. The large difference between the detected bright ion intensity distribution (blue circles) and background intensity values (grey squares) ensures the unambiguous detection of dark ion production even at timescales shorter than half of our acquisition period.

dark resonances shown in the Fig. 2-b) serves for precise calibration of the $4P_{1/2}$ population p_e using the steady state solution of 8-level optical Bloch equations. The standard Doppler cooling conditions correspond to p_e on the order of a few percent and the chemical reaction rate is too small to be observable in our vacuum level even with several tens of ions. In order to homogeneously enhance the laser induced reaction rate (1), the probability p_e was further tuned up to the average value of $p_e = (15.9 \pm 1.7)\%$ for all ions in the crystal using an additional 397 nm excitation beam propagating along the ion string. Nevertheless, the observation of a few chemical reactions still necessitated very long measurements and thus stable laser excitation parameters were ensured by frequency and intensity stabilizations of both lasers, with frequency locks employing as a reference single optical frequency comb referenced to hydrogen maser.

The illustration of the ion crystal employed in the presented measurement containing 34 $^{40}Ca^+$ ions is shown in

the Fig. 2-c), where the bottom picture illustrates one of the extremely rare events of one ion getting dark. This crystal has been observed for 51 hours and its image has been captured with 1.95 Hz rate and 500 ms acquisition time. The post-processing of the recorded images showed in total 4 reactions. After becoming dark, the ion always stayed in nonfluorescing state on a timescale of minutes, namely for 63.5 s, 934.5 s, 506 s and 366.5 s and then became bright again, which can be most likely attributed to an off-resonant optical dissociation[22]. The time-lapse images were processed one by one by averaging the photon counts from pixels surrounding the ion image for each ion separately. A typical evaluated histogram of detected count rates shown in Fig. 2-d) demonstrates that the fluorescence peak for each ion is separated very well from the background count rate values and thus any nonfluorescing events longer than 0.25 s would be unambiguously recognized. The observed timescales of the three dissociation events statistically practically exclude any dark events where the dissociation time would be faster or comparable to 0.25 s in the same experimental conditions, which further justifies the evaluation of the reaction rate as 1 reaction per 12.75 hours. The corresponding partial pressure of the H_2 in our system can be found using the equation (2), which results in $P_{H_2} \leq (2.1 \pm 1.1) \cdot 10^{-13}$ mBar and $P_{H_2} \leq (5.5 \pm 2.8) \cdot 10^{-12}$ mBar, when employing the reaction rate coefficient k_r from[20] and from[19], respectively. The quoted standard deviations correspond to two statistically independent uncertainty contributions. The dominant contribution is caused by the uncertainty of random and time independent success of observation of molecular reaction. The variance of number of reaction events is given by the Poisson distribution with a very large number of trials and very small success probability corresponding to 4 events per total number of trials. This value has been convolved with statistically independent uncertainty of $4P_{1/2}$ state population, which has been found by the statistical analysis of the detected fluorescence count rate.

The provided partial pressure analysis assumes that all molecular association events correspond to reaction of $^{40}Ca^+$ with H_2. This assumption is based on the dominant residual content of hydrogen observable on RGA before the chamber closure and on the typical characteristics of the residual gas content in the vast majority of stainless steel UHV chambers[6,7,17,29,32]. Although it is unlikely that we see reactions with other vacuum contaminants, it is practically demanding to implement means to unambiguously prove it and we have to regard the presented values as an upper limit on the hydrogen partial pressure, as contribution of any other element to the observed dark ion creation would effectively correspond to smaller hydrogen content in the chamber.

IV. DISCUSSION

The ultra-high-vacuum generation corresponds to a routine, yet the crucial technological task necessary for achieving control over single charged atomic ions and its methods are continuously revisited and improved among whole ion trapping community. Current efforts on scaling some prominent trapped-ion applications require experimenting with stable large ionic arrays which tighten up already stringent requirements on the vacuum levels well below 10^{-9} mBar. A room temperature ion trapping chamber presented here has recently demonstrated the distinctive ability of working with large and stable ion ensembles in experiments, where temporal fluctuations of ion numbers would inevitably cause a severe reduction of the observed phenomena[9,34]. The rigorous estimation of the achieved hydrogen partial pressure using the estimation of molecular reaction rates has led to its upper limits $P_{H_2} \leq (5.5 \pm 2.8) \cdot 10^{-12}$ mBar and $P_{H_2} \leq (2.1 \pm 1.1) \cdot 10^{-13}$ mBar using the reaction rate coefficient from[19] and from[20]. This corresponds to four chemical reactions in 51 hours long measurement with 34 ion crystal, which, to the best of our knowledge, is the lowest value reported for a room-temperature ion trapping experiment. The dominant uncertainty in the observed upper limit on the hydrogen partial pressure is caused by the large discrepancy in the reported reaction rate constants, which could not be feasibly resolved in the current vacuum apparatus. We plan to implement measures in a new vacuum chamber with Ca^+ ion trap comprising a high precision residual gas analyser, which would allow for its comparison.

The provided explicit instructions for the vacuum generation, hydrogen pressure estimation, and the achieved vacuum level itself, do not intend to be recognized as a milestone breaking, but rather constitute a solid and reliable reference for the realization and calibration of a chamber capable of temporarily stable storage of large ionic arrays. They complement a rich variety of recent notable reports from ion trapping community on measurement of effective lifetimes of ion strings with atomic ions localized in Paul traps. We do not attempt to quantitatively compare the reported vacuum levels, as different measures and atomic species could in principle lead to incomplete conclusions. We instead enlist the recent reported measurements relevant for the potential applications. The collision rates on the order of a single collision per hour per trapped ion have been reported by observations of dark ion position change in the $^{171}Yb^+$ ion string[3]. The same setup reported an average lifetime of about 5 minutes for 53 ion crystal with rare events reaching up to 30 minutes. Measurements of rates of the dark ion position change in the $^{40}Ca^+$ crystal resulted in single ion position change every 86 s on average for a 6-ion crystal and every 27 s for a chain of 20 ions[33]. The same method employed for a 5-ion crystal of $^{171}Yb^+$ resulted in hopping every 49 s on average[35]. The recent rigorous analysis of reorder rate for a two-ion $^{40}Ca^+ - ^{27}Al^+$ crystal motivated by the estimation of frequency shift in the optical atomic clock caused by background gas collisions resulted in the hydrogen-dominated background gas pressure of $(5.47 \pm 0.08) \times 10^{-10}$ mBar[32]. We stress again, that these results are generally dependent on trapping and laser cooling parameters, and thus not directly comparable. Alternative approach for achieving very low vacuum levels employs cryogenic vacuum setups[6,7]. Besides simplifying and speeding up the vacuum construction due to suppressed desorption rates, the reduced kinetic energy of the background gases limits the

observable heating of the ion crystal caused by collisions. The background gas pressure of $P_{4K} < 1.3 \cdot 10^{-13}$ mBar was estimated from dark ion production rates, while counting of the sensitive zig-zag crystal structural changes gave $P_{4.7K} < 1.3 \cdot 10^{-12}$ mBar[7]. Cryogenic setup reported in reference[6] employed highly charged ions and the charge-exchange reactions with hydrogen to derive its upper vacuum pressure limit of $P_{4.6K} < 1.26(-0.11/+0.12) \cdot 10^{-14}$ mBar. We believe that, together with these recent remarkable achievements, presented guidelines for the ion trapping vacuum chamber construction and achieved pressure estimation will facilitate current efforts in mastering large trapped ion arrays for a broad range of applications of quantum technologies[3,8–14].

ACKNOWLEDGMENTS

[1] A. D. Ludlow, M. M. Boyd, J. Ye, E. Peik, and P. O. Schmidt, "Optical atomic clocks," Reviews of Modern Physics 87, 637 (2015).

[2] T. Monz, D. Nigg, E. A. Martinez, M. F. Brandl, P. Schindler, R. Rines, S. X. Wang, I. L. Chuang, and R. Blatt, "Realization of a scalable shor algorithm," Science 351, 1068–1070 (2016).

[3] J. Zhang, G. Pagano, P. W. Hess, A. Kyprianidis, P. Becker, H. Kaplan, A. V. Gorshkov, Z.-X. Gong, and C. Monroe, "Observation of a many-body dynamical phase transition with a 53-qubit quantum simulator," Nature 551, 601 (2017).

[4] A. B. Salvador, G. Zarantonello, H. Hahn, A. Preciado-Grijalva, J. Morgner, M. Wahnschaffe, and C. Ospelkaus, "Multilayer ion trap technology for scalable quantum computing and quantum simulation," New Journal of Physics 21, 043011 (2019).

[5] M. Niedermayr, K. Lakhmanskiy, M. Kumph, S. Partel, J. Edlinger, M. Brownnutt, and R. Blatt, "Cryogenic surface ion trap based on intrinsic silicon," New Journal of Physics 16, 113068 (2014).

[6] P. Micke, J. Stark, S. A. King, T. Leopold, T. Pfeifer, L. Schmöger, M. Schwarz, L. Spieß, P. O. Schmidt, and J. López-Urrutia, "Closed-cycle, low-vibration 4 k cryostat for ion traps and other applications," arXiv preprint arXiv:1901.03630 (2019).

[7] G. Pagano, P. W. Hess, H. B. Kaplan, W. L. Tan, P. Richerme, P. Becker, A. Kyprianidis, J. Zhang, E. Birckelbaw, M. R. Hernandez, Y. Wu, and C. Monroe, "Cryogenic trapped-ion system for large scale quantum simulation," Quantum Science and Technology 4, 014004 (2018).

[8] N. Friis, O. Marty, C. Maier, C. Hempel, M. Holzäpfel, P. Jurcevic, M. B. Plenio, M. Huber, C. Roos, R. Blatt, and B. Lanyon, "Observation of entangled states of a fully controlled 20-qubit system," Physical Review X 8, 021012 (2018).

[9] P. Obšil, L. Lachman, T. Pham, A. Lešundák, V. Hucl, M. Čížek, J. Hrabina, O. Číp, L. Slodička, and R. Filip, "Nonclassical light from large ensembles of trapped ions," Physical Review Letters 120, 253602 (2018).

[10] T. Monz, P. Schindler, J. T. Barreiro, M. Chwalla, D. Nigg, W. A. Coish, M. Harlander, W. Hänsel, M. Hennrich, and R. Blatt, "14-qubit entanglement: Creation and coherence," Physical Review Letters 106, 130506 (2011).

[11] J. Keller, T. Burgermeister, D. Kalincev, A. Didier, A. Kulosa, T. Nordmann, J. Kiethe, and T. Mehlstäubler, "Controlling systematic frequency uncertainties at the 10- 19 level in linear coulomb crystals," Physical Review A 99, 013405 (2019).

[12] J. Kiethe, R. Nigmatullin, D. Kalincev, T. Schmirander, and T. Mehlstäubler, "Probing nanofriction and aubry-type signatures in a finite self-organized system," Nature Communications 8, 15364 (2017).

[13] C. Maier, T. Brydges, P. Jurcevic, N. Trautmann, C. Hempel, B. P. Lanyon, P. Hauke, R. Blatt, and C. F. Roos, "Environment-assisted quantum transport in a 10-qubit network," Physical Review Letters 122, 050501 (2019).

[14] S. Ulm, J. Roßnagel, G. Jacob, C. Degünther, S. Dawkins, U. Poschinger, R. Nigmatullin, A. Retzker, M. Plenio, F. Schmidt-Kaler, and K. Singer, "Observation of the kibble–zurek scaling law for defect formation in ion crystals," Nature communications 4, 2290 (2013).

[15] C. D. Bruzewicz, R. McConnell, J. Chiaverini, and J. M. Sage, "Scalable loading of a two-dimensional trapped-ion array," Nature Communications 7, 13005 (2016).

[16] A. H. Nizamani, M. A. Rind, N. M. Shaikh, A. H. Moghal, and H. Saleem, "Versatile ultra high vacuum system for ion trap experiments: Design and implementation," Intl. Journal of Advancements in Research & Technology 2 (2013).

[17] R. Calder and G. Lewin, "Reduction of stainless-steel outgassing in ultra-high vacuum," British Journal of Applied Physics 18, 1459 (1967).

[18] L. D. Carr, D. DeMille, R. V. Krems, and J. Ye, "Cold and ultracold molecules: science, technology and applications," New Journal of Physics 11, 055049 (2009).

[19] A. K. Hansen, M. A. Sørensen, P. F. Staanum, and M. Drewsen, "Single-ion recycling reactions," Angewandte Chemie International Edition 51, 7960–7962 (2012).

[20] N. Kimura, K. Okada, T. Takayanagi, M. Wada, S. Ohtani, and H. A. Schuessler, "Sympathetic crystallization of cah+ produced by a laser-induced reaction," Phys. Rev. A 83, 033422 (2011).

[21] C.-w. Chou, C. Kurz, D. B. Hume, P. N. Plessow, D. R. Leibrandt, and D. Leibfried, "Preparation and coherent manipulation of pure quantum states of a single molecular ion," Nature 545, 203 (2017).

[22] R. Rugango, A. T. Calvin, S. Janardan, G. Shu, and K. R. Brown, "Vibronic spectroscopy of sympathetically cooled cah+," ChemPhysChem 17, 3764–3768 (2016).

[23] P. F. Staanum, K. Højbjerre, P. S. Skyt, A. K. Hansen, and M. Drewsen, "Rotational laser cooling of vibrationally and translationally cold molecular ions," Nature Physics 6, 271 (2010).

[24] T. Schneider, B. Roth, H. Duncker, I. Ernsting, and S. Schiller, "All-optical preparation of molecular ions in the rovibrational ground state," Nature Physics 6, 275 (2010).

[25] S. Schiller and V. Korobov, "Tests of time independence of the electron and nuclear masses with ultracold molecules," Physical Review A 71, 032505 (2005).

[26] D. Petitprez, B. Lemoine, C. Demuynck, J. Destombes, and B. Macke, "Infrared diode laser spectroscopy of cah and cad (x 2σ+). determination of mass-independent parameters," The Journal of Chemical Physics 91, 4462–4467 (1989).

[27] M. Guggemos, Precision spectroscopy with trapped $^{40}Ca^+$ and $^{27}Al^+$ ions, Ph.D. thesis, University of Innsbruck (2017).

[28] S. V. Kagwade, C. R. Clayton, D. Chidambaram, and G. P. Halada, "Photochemical breakdown of acetone on copper," Electrochimica Acta 46, 2337–2342 (2001).

[29] A. Chambers, Modern vacuum physics (CRC Press, 2004).

[30] L. Westerberg, B. Hjörvarsson, E. Wallén, and A. Mathewson, "Hydrogen content and outgassing of air-baked and vacuum-fired stainless steel," Vacuum 48, 771–773 (1997).

[31] W. Prins and J. J. Hermans, "Theory of permeation through metal coated polymer films," J. Phys. Chem. 63 (1959).

[32] A. Hankin, E. Clements, Y. Huang, S. Brewer, J.-S. Chen, C. Chou, D. Hume, and D. Leibrandt, "Systematic uncertainty due to background-gas collisions in trapped-ion optical clocks," arXiv preprint arXiv:1902.08701 (2019).

[33] C. Hempel, Digital quantum simulation, Schrödinger cat state spectroscopy and setting up a linear ion trap, Ph.D. thesis, University of Innsbruck (2014).

[34] P. Obšil, A. Lešundák, T. Pham, G. Araneda, O. Číp, R. Filip, and

L. Slodička, "Scalable phase interference from trapped ion chains," arXiv preprint arXiv:1804.01518 (2018).

[35]H. A. Fürst, *Trapped ions in a bath of ultracold atoms*, Ph.D. thesis, Van der Waals-Zeeman Institute (2019).

Research article 2

Optical frequency analysis on dark state of a single trapped ion

A. Lesundak, T. M. pham, M. Cizek, P. Obsil, L. Slodicka, AND O. Cip

Optical frequency analysis on dark state of a single trapped ion

ADAM LEŠUNDÁK[1,*], TUAN M. PHAM[1], MARTIN ČÍŽEK[1], PETR OBŠIL[2], LUKÁŠ SLODIČKA[2], AND ONDŘEJ ČÍP[1]

[1] *Institute of Scientific Instruments of the Czech Academy of Sciences, Královopolská 147, 612 64 Brno, Czech Republic*
[2]*Department of Optics, Palacký University, 17. listopadu 12, 771 46 Olomouc, Czech Republic*
**lesundak@isibrno.cz*

Abstract: We demonstrate an optical frequency analysis method using the Fourier transform of detection times of fluorescence photons emitted from a single trapped ^{40}Ca$^+$ ion. The response of the detected photon rate to the relative laser frequency deviations is recorded within the slope of a dark resonance formed in the lambda-type energy level scheme corresponding to two optical dipole transitions. This approach enhances the sensitivity to the small frequency deviations and does so with reciprocal dependence on the fluorescence rate. The employed lasers are phase locked to an optical frequency comb, which allows for precise calibration of optical frequency analysis by deterministic modulation of the analyzed laser beam with respect to the reference beam. The attainable high signal-to-noise ratios of up to a MHz range of modulation deviations and up to a hundred kHz modulation frequencies promise the applicability of the presented results in a broad range of optical spectroscopic applications.

1. Introduction

The optical atomic spectroscopy is a well-developed research field comprising some of the most advanced applications of optical and laser technologies. It provides many crucial investigation methods and contributes to a whole spectrum of modern natural sciences. At the same time, it still holds an immense potential for further advancements by utilization of newly available tools for light generation, control and analysis developed within studies of light and matter at the level of individual particles [1-3]. The possibilities of employing the individual atomic systems for optical spectroscopy have in the last decade to a large extent governed the development in the field of optical frequency metrology and its attainable accuracies [4]. The implementation of frequency analysis with individual atomic particles has been dominantly focused on the development of optical frequency references utilizing a direct probing of narrow atomic transitions. Related phenomenological advancements have mostly been corresponding to knowledge improvements of atomic internal structure and its sensitivity to external disturbances. The development of advanced methods for laser frequency stabilization complemented by progress in generation and control of optical frequency combs seen in the past few years have recently enabled the pioneering excitations of Raman transitions in the gigahertz [5, 6] and terahertz domain [7] as well as new atomic spectroscopy methods [8].

Here we present a method for optical frequency analysis based on the time resolved spectroscopy on atomic dipole transitions with enhanced sensitivity to frequency deviations using the probing of individual atoms close to a two-photon resonance in a lambda-like three-level energy scheme. The spectral resolution and bandwidth of the presented approach profit from both, the high attainable count rates on atomic transitions with large decay rates and, at the same time, possibilities of continuous probing of narrow two-photon resonances with disparate optical wavelengths enabled by the sub-wavelength localization of probed single

atom. The two-photon interference not only enhances the spectral sensitivity but, crucially, it allows for optical frequency analysis of target optical field on optical reference field with very different frequency, which corresponds to a paramount task in many metrological applications [9-11]. The interference mediated by laser cooled atoms allows for optical frequency beating of two optical fields separated by hundreds of THz. This is typically realized indirectly via an optical frequency comb, which provides a traceability to stable frequency reference in a broad optical ruler [12, 13]. The presented method provides an alternative approach within limited spectral range, by representing a convertor of the relative optical frequency difference to the intensity of fluorescence emitted by a single atom.

We implemented a continuous measurement scheme on a single trapped ^{40}Ca$^+$ ion excited in the lambda-type energy level scheme $4S_{1/2} \leftrightarrow 4P_{1/2} \leftrightarrow 3D_{3/2}$ by two lasers at wavelengths 397 nm and 866 nm, respectively. The 397 nm laser is simultaneously used for Doppler cooling, while the 866 nm laser serves as a repumper from a long-lived $3D_{3/2}$ manifold. Both lasers are phase locked to particular teeth of a fiber frequency comb referenced to a hydrogen maser. In this way, they adopt known frequency linewidths and stability of the optical reference. We analyze the properties of the presented scheme in terms of the fluorescence intensity response to imposed laser frequency characteristics and measurement length. For this purpose, the repumping laser serves as an analyzed field to which a deterministic frequency modulation is applied, while the cooling laser is the reference field with fixed frequency. A simple theoretical model for achievable signal-to-noise ratios (*SNR*) is compared with measured fluorescence intensity responses in a range of modulation frequencies and amplitudes. Finally, we estimate the limits of the presented method and discuss the comparisons of measured data with simulations.

2. Experimental scheme

To measure the dynamic response of ion fluorescence to the frequency detuning of the excitation lasers, it is necessary to narrow the linewidths and stabilize the frequencies of the lasers to levels where they do not interfere with the measurements. For this reason, two extended-cavity diode lasers (ECDLs) are phase locked to the optical frequency comb. The whole experimental setup is schematically shown in Fig. 1 with three parts: a) is dedicated to the ECDLs, b) to the phase locking and c) to the ion trap. The frequency comb with a center frequency at 1550 nm is frequency doubled by the second harmonic generation (SHG) process and broadened by a photonic crystal fiber to generate an optical supercontinuum ranging from about 600 nm to 900 nm. This broad spectrum is mixed with both laser beams to create beat notes with particular frequency comb teeth. The product of this mixing is spatially separated according to the wavelengths by a diffraction grating and serves as a signal for phase locked loop (PLL), which efficiently narrows a laser linewidth down to linewidth of a single component of the frequency comb. This method allows for stabilization of multiple lasers in near infrared and visible range to a single frequency reference within one optical setup. The two radio frequency parameters of optical frequency comb - the repetition rate f_{rep} and the offset frequency f_{ceo} are referenced to a hydrogen maser, which is disciplined for long-term stability by a GPS clock.

Particular beat note signal between the nearest comb tooth and the laser is amplified, and mixed with a reference signal. This reference signal is generated by a radiofrequency (RF) synthesizer referenced to the hydrogen maser, and has the value of desired beat note frequency f_{b}. After low-pass filtering, the product of the mixing is a DC signal that is proportional to the phase error of the comb-laser beat note and serves as the error signal for laser phase-locked loop (PLL). The PLL is realized with fast analog control electronics. In this way, the laser linewidths efficiently adopt the linewidths of the frequency comb. The cooling laser at 397 nm cannot be directly locked to the frequency comb and the lock is realized at its fundamental wavelength at 794 nm. The laser frequencies written in terms of the comb frequencies are then: $v_{866} = 2(n_{(2\cdot866)}f_{\text{rep}} + f_{\text{ceo}}) + f_{\text{b866}}$ and $v_{397} = 2[2(n_{(2\cdot794)}f_{\text{rep}} + f_{\text{ceo}}) + f_{\text{b794}}]$. The frequency difference

between lasers as seen by the ion is $\Delta_v = (4n_{(2 \cdot 794)} - 2n_{(2 \cdot 866)})\, f_{\text{rep}} + 2f_{\text{ceo}} + f_{\text{b794}} - f_{\text{b866}}$, where $4n_{(2 \cdot 794)} - 2n_{(2 \cdot 866)} = 1635856$. Standard deviations of the comb basic frequencies are $\sigma(f_{\text{rep}}) \leq 1$ mHz and $\sigma(f_{\text{ceo}}) \leq 1$ Hz at 100 s averaging time, which indicates standard deviation of laser frequency detuning below 1 Hz at the same averaging timescales. We measured the linewidth of a single comb tooth by beating it with a laser at 1540 nm which has linewidth at the level of a few Hz and obtained FWHM = 40 kHz with 1 kHz resolution bandwidth setting. The main contribution to this linewidth comes from the f_{ceo}. The f_{rep} contribution in these time scales can be neglected. After each SHG process, the linewidth is also doubled. However, since the noise source is common for both 397 nm and 866 nm lasers, a simple estimation of their mutual linewidth based on Δ_v leads to 80 kHz.
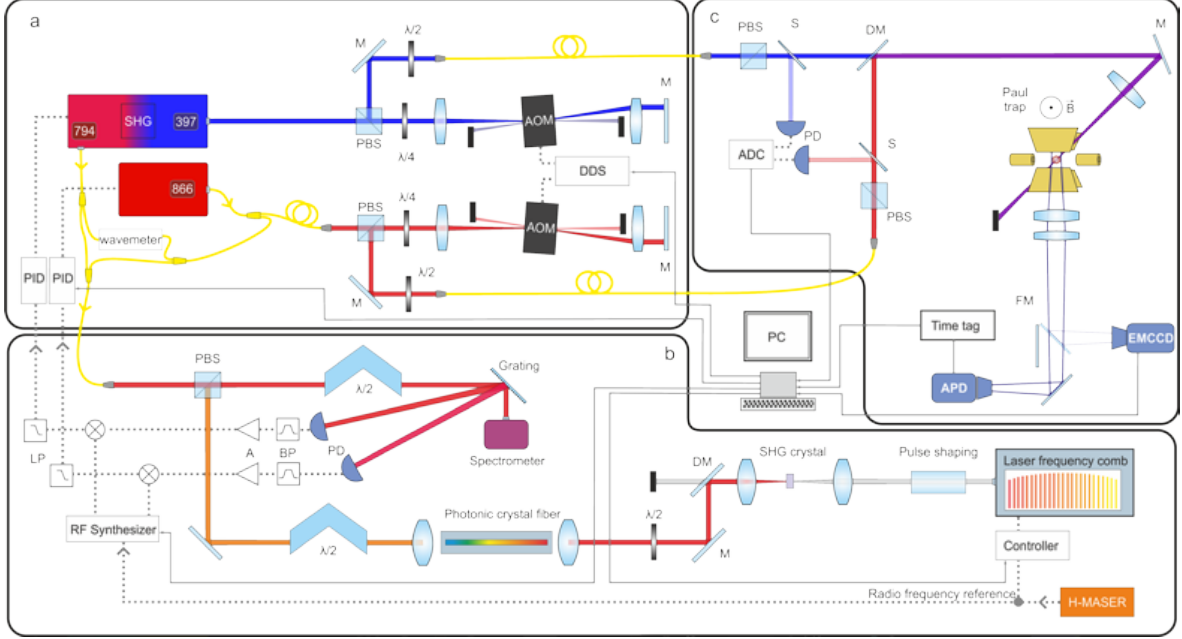

Fig. 1. Scheme of the experimental setup distributed over three optical tables corresponding to parts *a, b* and *c*. The cooling laser beam is generated by doubling the 794 nm ECDL laser to 397 nm. The near infrared laser beams are sent through an optical fiber to table *b* for frequency stabilization. Laser beams prepared for excitation with the trapped ion are led into acousto-optic modulators (AOMs) in double pass configurations for frequency and amplitude modulation and then sent to the ion trap positioned on optical table *c*. The optical frequency comb comprising the units for frequency doubling and supercontinuum generation is optically mixed with lasers for generating the error signals for frequency stabilization. The excitation laser fields are set to particular desired polarization and are amplitude stabilized at the proximity of the ion chamber on optical table *c*. The single ion fluorescence is collected by a lens with numerical aperture of 0.2 and detected by EMCCD camera or single photon avalanche diode (APD). The detection signals including precise photon arrival times are recorded using fast time-tagging module or converted by analog-digital card (ADC) for further processing.

The target frequencies of atomic transitions are achieved by fine frequency tuning with acousto-optic modulators (AOM) in double-pass configuration. These AOMs are also used for stabilization of excitation laser intensities. The beams are combined by a dichroic mirror and focused to the center of the linear Paul trap with 45° angle of incidence relative to the trap axis. The ion is trapped in the radial *x, y* directions by harmonically oscillating electric field at frequency of 30 MHz and with an amplitude corresponding to the radial secular motion frequency $f_{x,y} \approx 1.66$ MHz. The axial position is confined by the voltage applied to tip electrodes $U_{\text{tip}} = 500$ V, leading to the axial secular frequency $f_z \approx 780$ kHz. The ion is Doppler cooled by a red detuned 397 nm laser. Fluorescence from the ion is collected in the direction of the magnetic field using a lens system with numerical aperture of 0.2. A flip mirror in the optical path is used to switch the detection between the electron multiplying CCD (EMCCD) camera

and single-photon avalanche detector (SPAD). The photon detection times are recorded with fast time tagging module with up to 4 ps resolution.

In the case of $^{40}Ca^+$ ion, the convenient three-level systems with Λ configuration can be realized on transitions $4S_{1/2} \leftrightarrow 4P_{1/2} \leftrightarrow 3D_{3/2}$, which are simultaneously driven by two laser fields at wavelengths 397 nm and 866 nm. For the individual laser detunings set to the two-photon resonance corresponding to the vanishing difference $\Delta_{866} - \Delta_{397} = 0$, the population of the excited state $4P_{1/2}$ disappears in ideal case. This corresponds to a dark state with no fluorescence emission [14, 15]. In practice, the dark state population is limited by the finite linewidth of the two involved lasers and finite coherence between the ground states $4S_{1/2}$ and $3D_{3/2}$ as well as thermal population of atomic motion [16-19]. The magnetic field of 6.1 Gauss is applied at the position of the ion to lift the degeneracy of Zeeman states which results in effective internal energy level scheme with eight states, see Fig. 2-a). The angle between linear polarization of laser fields is chosen to be perpendicular to the magnetic field, therefore only transitions with $\Delta m_j = \pm 1$ are excited, which allows for efficient depopulation of the outermost states from the $3D_{3/2}$ manifold and leads to the observation of four dark resonances. Tuning the 866 nm laser to the slope of particular dark resonance, which is described by the slope parameter $m(\Delta_{866})$ representing the resonance gradient, allows to use the ion as a direct convertor of frequency deviation to fluorescence intensity due to its quasi-linear dependence. See Fig. 2-b) for schematic explanation. The fluorescence spectrum with dark resonances can be very well reproduced using standard approach based on 8-level optical Bloch equations [20], which allow for the estimation or cross-check of several experimental parameters including laser detunings, intensities or magnetic field amplitude and direction.
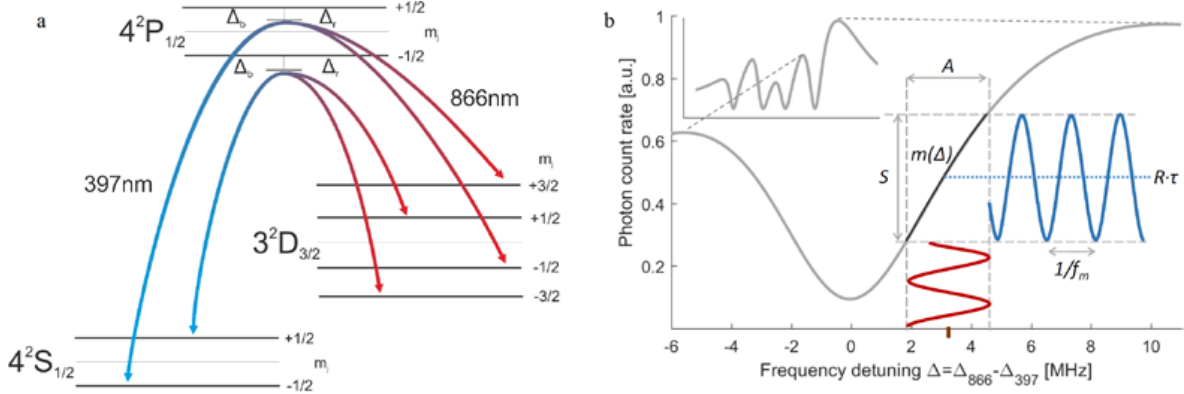

Fig. 2. Principle of operation of time-resolved optical spectroscopy close to a dark-resonance of a trapped $^{40}Ca^+$ ion. a) The employed energy level scheme of $^{40}Ca^+$. The two laser fields with polarizations perpendicular to the magnetic field lead to observation of four dark states between $S_{1/2}$ and $D_{3/2}$ manifolds. b) A simulation of the $P_{1/2}$ level occupation probability proportional to fluorescence intensity as a function of 866 nm laser frequency detuning Δ_{866}. The detail of the selected dark resonance depicts the fundamental parameters determining the performance of the spectral analysis including the detuning Δ_{866}, frequency deviation of the frequency modulation A, modulation frequency f_m, conversion through the slope with parameter m onto the fluorescence with an average photon rate per second R and measured with a SPAD gate interval τ.

The enhancement of the dark resonance contrast and slope steepness by utilization of frequency stabilization of 397 nm and 866 nm lasers to the frequency comb is illustrated in Fig. 3. At this locking configuration, the fluorescence spectrum is measured, though only in narrow bandwidth limited by the PLL frequency range corresponding to $f_{rep}/2$. The whole spectrum containing all dark resonances is measured again but with the 866 nm laser frequency locked to the wavemeter with time constant in order of a second. This "wavemeter frequency lock" does not enhance the coherence properties of the laser in relevant frequency bandwidth in our scope of interest, but ensures well defined frequency scanning of the whole dark resonance spectra. Both fluorescence spectra are fitted with the optical Bloch equations; see Fig. 3. From

observed four resonances, one corresponding to transition between electronic states $|S_{1/2},+1/2\rangle$ and $|D_{3/2},-3/2\rangle$ is chosen for frequency analysis experiments because it is the closest one to a global fluorescence maximum and has the longest resonance slope. The measurement point Δ_{M1} is chosen in the middle of the slope of the dark resonance to maximize the measurable amplitudes of frequency modulation. The slope parameter for linear approximation at this measurement point was evaluated to $m(\Delta_{M1}) = 1.79\pm0.01$ counts s^{-1}·kHz^{-1}, with corresponding photon count rate of 6800 counts·s^{-1}. The frequency detunings of analyzed and reference lasers from their corresponding transition frequencies are $\Delta_{866} \approx$ -9 MHz and $\Delta_{397} \approx$ -12 MHz. The fit of optical Bloch equations of the measured fluorescence rates does not perfectly follow the fluorescence curve since the equations do not include the ion motion affected by the Raman cooling and heating processes naturally involved within the measurement scheme [16]. Particularly at the measurement point Δ_{M1} its gradient corresponds to $m_{Bloch}(\Delta_{M1}) = 2.21$ counts·s^{-1}·kHz^{-1}, which is 24% greater than the gradient of the numerical fit. For this reason, we use the polynomial fit as the slope function m_{nl}, instead of the fit of the optical Bloch equations. The fit parameters are: the magnetic field **B** = 6.1 Gauss, the detuning of the blue laser Δ_{397} = -12 MHz, angle between the light fields and the magnetic field α= 90°, saturation parameters S_{397}=1, S_{866}=4 and combined linewidth of the two lasers Γ= 251 kHz and Γ=124 kHz for the case of employed PLL frequency stabilization.
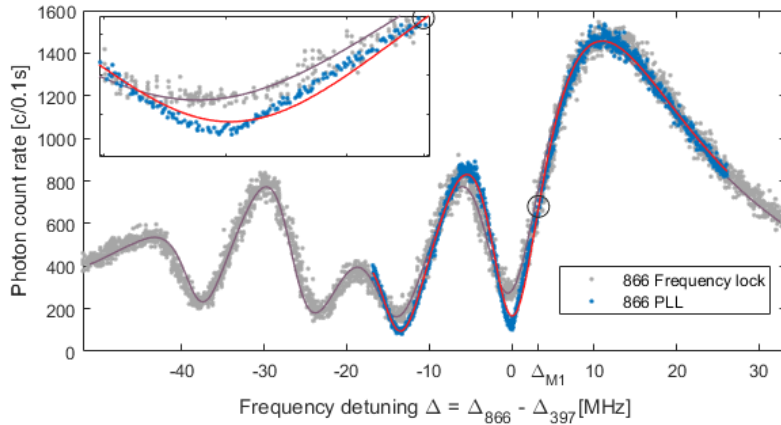

Fig. 3. Dark blue dots represent the fluorescence spectrum measured with both ECDL lasers phase-locked to the frequency comb with limited bandwidth due to PLL limited scanning range. Red line is the fit and black circle corresponds to the measurement point. Parameters of the fit are the magnetic field: **B**= 6.1 Gauss, the detuning of the blue laser Δ_{397} = -12 MHz, angle between the light fields and the magnetic field α= 90°, saturation parameters S_{397}=1, S_{866}=4 and combined linewidth of both lasers Γ=124 kHz. Light blue dots represent the fluorescence spectrum with all dark resonances visible, measured by scanning of the 866 nm laser frequency locked to the wavemeter. Purple line shows its theoretical fit with the lasers combined linewidth parameter Γ=251 kHz. The black circle marks the chosen measurement point Δ_{M1}. The inset depicts the lower part of the resonance slope to show the differences between the two spectra and the fits in the relevant region.

3. Analysis of the spectral sensitivity

To determine the dynamic response of the ion as a detector of mutual frequency shifts of the two lasers, we introduce a controlled frequency modulation of one of the lasers followed by fluorescence signal processing. A phase noise power spectral density distribution of both phase locked ECDLs to the optical frequency comb has dominantly *1/f* noise shape profile [21]. The low magnitude of the noise has no influence on the dynamic response of the ion characterization. The modulation is applied to the 866 nm repumping laser as a harmonic frequency modulation with specific modulation frequency f_m and peak frequency deviation A (frequency deviation), see Fig. 2. The modulation results in a periodic signal on fluorescence which can be considered harmonic due to the quasi-linearity of the slope close to the measurement point. The fluorescence signal is detected by the SPAD and recorded as arrival

times of detected photons by the time tagging module. The timing resolution of the detected fluorescence is limited by the resolution of the SPAD and is on the level of 1 ns. The processing of such discrete signal with a nanosecond-sampling period can be simplified by summing the number of photon counts over time τ (gate interval). This acts as the filtering by a low-pass filter, which does not limit the extracted information about the spectrum if the fluorescence signal does not contain significant spectral components above the low-pass filter frequency band. The time tag record is thus processed into data of photon count rate in units of number of photon counts per interval bin τ.

To determine the theoretical response function of the detected fluorescence photon rate to the introduced frequency modulation, we compare natural fluorescence noise to the observable signal in the evaluated frequency spectrum. The equation for the SNR is derived as the ratio of function describing the amplitude of harmonically modulated fluorescence $S(f_m, \tau, A)$ to amplitude of fluorescence detection noise $N(R, T, \tau)$. The signal function converts the 866 nm laser frequency deviation A to the amplitude of fluorescence harmonic signal $S(f_m, \tau, A)$ according to the slope parameter of dark resonance $m(\Delta_{866})$, modulation frequency f_m and the gate interval τ. Although not necessary, a linear approximation of the slope parameter can simplify the evaluation and is defined as $m = \partial(\langle n \rangle \cdot s^{-1})/\partial \Delta_{866}$ at measurement detuning point Δ_M, where $\langle n \rangle \cdot s^{-1}$ is an average number of detected photons per second. In case of $(1/f_m) \ll \tau$ and the linear slope parameter m, the fluorescence signal amplitude can be approximated as $S(f_m, \tau, A) \approx mA\tau$. The modulation frequency f_m and the gate interval τ affects effective fluorescence modulation amplitude A_{eff} by averaging the fluorescence over time τ,

$$A_{\text{eff}}(\tau) = \frac{1}{\tau} \left| \int_0^\tau A \cos(f_m t) \, dt \right| = A \left| \text{sinc}(f_m \tau) \right|. \tag{1}$$

The resulting amplitude S of the imposed signal is

$$S = mA\tau \left| \text{sinc}(f_m \tau) \right|. \tag{2}$$

The SNR can be then found by comparing the amplitudes of detectable signal and the noise for a given frequency bandwidth. In an ideal case, when the noise contributions from the reference laser field and the applied magnetic fields are negligible, the noise of detected fluorescence corresponds to the shot noise. The noise amplitude can then be expressed as the shot noise of the average photon count rate R over number of measurement samples $n_s = T/\tau$,

$$N = \sqrt{\frac{R\tau}{T}}, \tag{3}$$

where $R = \langle n \rangle / \tau$ is the average count rate per gate interval τ, and T is the measurement time. The corresponding SNR is

$$SNR = \frac{S}{N} = \sqrt{\frac{T\tau}{R}} mA \left| \text{sinc}(f_m \tau) \right|. \tag{4}$$

In case of large frequency deviations ($A \approx$ hundreds of kHz) it is important to include a function, which reflects a true response of the observable fluorescence rate to the relative frequency detuning of analyzed laser Δ_{866}. The nonlinear slope function $m_{nl}(\Delta_{866})$ is taken from a polynomial fit of a measured fluorescence spectrum around the measurement point. To obtain the signal amplitude, modulation amplitude factor $m \cdot A$ is replaced with one half of the fluorescence difference at the two extremes of modulated detuning frequency $\Delta_M + A$ and $\Delta_M - A$. This yields

$$SNR = \frac{1}{2} \sqrt{\frac{T\tau}{R}} \sum_{n=1}^{5} \left[p_n (\Delta_M + A)^{n-1} - p_n (\Delta_M - A)^{n-1} \right] \left| \text{sinc}(f_m \tau) \right|, \tag{5}$$

where p_n are coefficients of nth degree polynomial fit $m_{nl}(\Delta_{866})$.

4. Measurements of the fluorescence intensity response to the laser frequency modulation

The spectrum of the analyzed 866 nm laser deviations is measured by keeping the reference 397 nm laser at a constant detuning Δ_{397} and modulating the frequency detuning $\Delta_{866}(t) = \Delta_M + A\cos(f_m t)$. The measurements are done for various sets of modulation frequencies, frequency deviations and frequency detunings. Each measurement is analyzed in terms of its frequency spectrum with respect to the time bin length τ. For the given τ, the FFT algorithm evaluates the spectrum and the frequency component at the given modulation frequency (or with the highest amplitude) is compared to the average amplitude of the whole spectrum. The length of individual measurements is set to be an integer multiple of $1/f_m$, to avoid the spectral leaking in the FFT spectrum. The natural unmodulated fluorescence has Poissonian distribution, thus its spectrum has the character of white noise and can be averaged as a whole.

Relatively low photon count rate does not theoretically place any fundamental limit on the detectable modulation frequency. The information about frequency modulation is obtained from the modulation of the photon counts in the time bins and the information is thus still preserved even when the average count per bin is below one. Note that this should not be confused with the frequency detuning out of dark resonance slope, e.g. detuning into the bottom of the dark resonance where the count rate could eventually drop to zero. As mentioned above, the slope function m_{nl} is defined in a certain region of the count rate (2000 c·s^{-1} to 14000 c·s^{-1}). These boundaries obviously scale with the gate interval. A check that fluorescence has not crossed these boundaries, e.g. due to laser-locking dropout or ion vacuum impurity kick, has been performed for all measurements with 10 ms gate interval. Very rare but possible dropouts with prompt reappearing on shorter time scales can be considered to have negligible effect on the resulting signal.

We summarize the results of the frequency response measurements in four figures. Three of them are done at measurement point Δ_{M1} and emphasize the $SNR(\tau)$ dependence on the critical measurement and evaluation parameters with respect to the gate interval τ, simulating variable gate time of a photodetector. These important parameters include modulation frequency, frequency deviation, and measurement time. The minimum of τ is chosen such that $\text{sinc}(f_m\tau_{min}) > 0.99$ and the maximum is chosen arbitrary but always much higher than $1/f_m$. The last figure compares the $SNR(\Delta_M)$ for two modulation frequencies with respect to the measurement point Δ_M to allow for estimation of optimal measurement points in future experiments. Note that we do not attempt to cover the whole accessible spectral range of modulation frequencies f_m and frequency deviations A, but rather illustrate the working mechanism of the presented scheme and show its intrinsic limits.

4.1 Modulation frequency

First, we evaluate $SNR(f_m,\tau)$ performance of the method in term of the frequency bandwidth by realization of the measurements with varying modulation frequencies and constant frequency deviation. We set the length of the measurements to $T = 300$ s, frequency deviation to $A = 300$ kHz to be well within the employed resonance slope and range of modulation frequencies from $f_m = 66$ Hz to 120 kHz. For values of τ longer than the period corresponding to the modulation frequency f_m, the modulation component is aliased in the spectrum at aliased frequencies $f_{alias} = |b/(2\tau) - f_m|$, where folding factor b is the closest even integer of multiple $2f_m\tau$. The values of signal-to-noise ratio are then $SNR = S_m/N_m$, where S_m is the FFT frequency component at the modulation frequency f_m or at the frequency f_{alias} (for $\tau > 1/f_m$) and N_m is the average amplitude of the whole FFT spectrum excepting the DC component. Importantly, the single ion based spectral analysis presented in Fig. 4. shows high attainable SNR in the whole measured spectral range of f_m. The observed $SNR(f_m,\tau)$ ratios are well reproduced by the theoretical predictions of eq. (5) up to modulation frequencies comparable to the photon count rate $R = 6800$ c·s^{-1}.
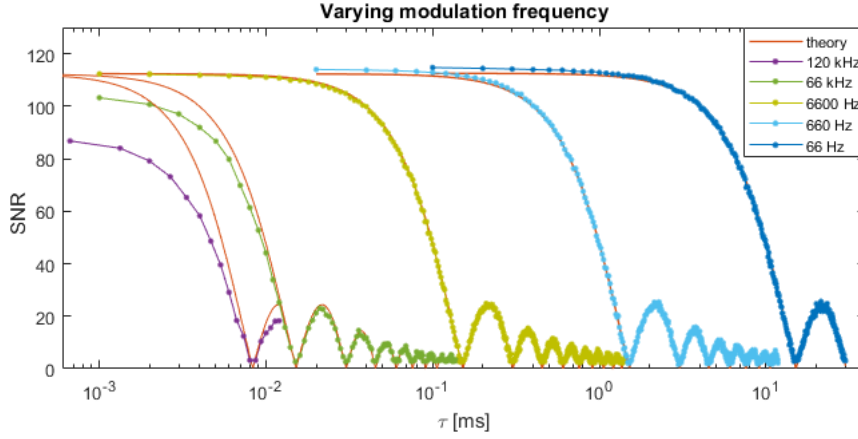
Fig. 4. Measured signal-to-noise ratio for 300 s long measurements of fluorescence intensity response to modulated detuning Δ_{866} as a function of the analysis gate interval τ. Frequency deviation is kept at 300 kHz and modulation frequency varies in a broad range from 66 Hz to 120 kHz. The measured data are shown as full circles and red lines are corresponding theoretical plots evaluated using nonlinear slope function m_{nl}. The mean time between two successive photon detections is ~ 0.15 ms.

4.2 Frequency deviation and measurement time

We have studied the potential of the presented spectrometry method with respect to capturing the frequency deviation A within the measurement time T. The expectable upper limit will be given by the spectral width of the dark resonance slope, while the lowest detectable modulation depths will depend on the amount of the detection noise. The SNR dependence on the gate interval is measured for low modulation frequency $f_m = 66$ Hz to avoid any effect of fast modulation on the observability of high modulation amplitudes. Figure 5. shows measured data of SNR for A ranging from 10 to 1000 kHz and T from 2.5 to 500 s.
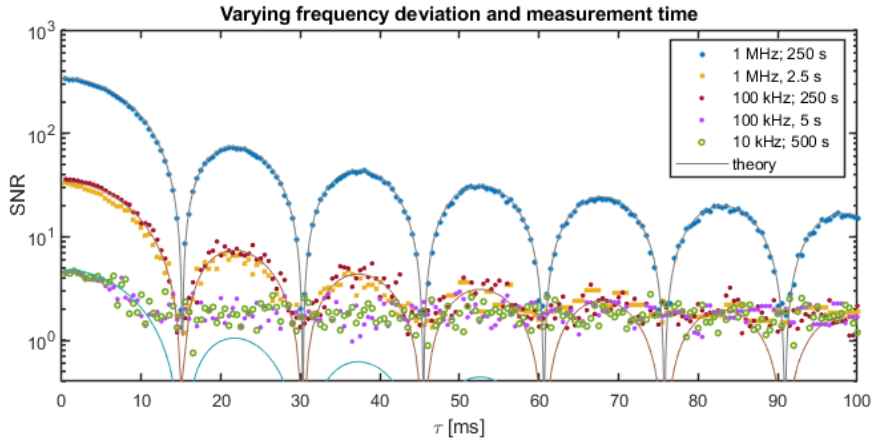

Fig. 5. Signal-to-noise ratio measurements of fluorescence with harmonically modulated detuning of analyzed laser field Δ_{866} with modulation frequency set to 66 Hz as a function of a gate interval τ. The measured data for selected combinations of frequency deviations and measurement times are shown with dots. Lines show the theoretical simulation of SNR. Amplitude levels for signals are taken from known frequency position in the spectrum.

The combinations are chosen in a manner to advert that an x-times lower A gives the same value of SNR if the measurement time is an x^2-times longer, reflecting the close to ideal Poissonian character of the detection noise. The measured SNR data nicely reproduces the theoretical predictions down to a plateau of the lowest detectable signal, which has its limits given by amplitudes of shot noise at the specific frequency components f_m or f_{alias}. The plateau is measured to be on the level of $SNR_{pl} = 1.8\pm0.4$, which corresponds to $A_{pl} = 38\pm8$ kHz for $T = 5$ s respectively $A_{pl} = 3.8\pm0.8$ kHz for $T = 500$ s.

4.3 SNR limit for unknown modulation frequency

For a general task of estimation of amplitude of unknown frequency components, the whole FFT spectrum has to be searched. In this case, the signal-to-noise ratio can be calculated as $SNR(T,\tau) = S_{max}/N_m$, where S_{max} is the highest amplitude component of the whole FFT frequency spectrum excepting the DC component. Thus, there is always a spectral component with amplitude at least on the level corresponding to the detectable limit defined here as variable SNR_{lim}. That means, if there is an unknown frequency modulation, we are able to detect it only if its SNR is higher than SNR_{lim}. It is obtained by simulating data of shot noise with Poissonian distribution. The simulated data represent pure fluorescence without any modulation and have the same count rate R and measurement length T as the real data. This simulated fluorescence is analyzed in the same way as the measured data and the SNR_{sim} is calculated. An average of 500 simulations SNR_{sim} is used for estimation of the detection limit $SNR_{lim}(T,\tau) = \langle SNR_{sim} \rangle_{500}$. Fig. 6. shows two measurements of $SNR(T,\tau)$ both with $f_m = 66$ Hz, $A = 300$ kHz and with total measurement times T equal to 3 and 300 s. Observed $SNR(T,\tau)$ values strictly follow theoretical curves in all regions above the limit of $SNR_{lim}(T,\tau)$. Importantly, the figure also shows the effect of the measurement length T on the detectable limit SNR_{lim} and as can be seen, the limit is not constant with T. A simple explanation is, as there is a higher probability for higher noise amplitude in longer measurements, SNR_{lim} actually increases with measurement time. The rise of SNR_{lim} is compensated by a decrease of noise mean value N. This ensures better detection sensitivity for longer measurements. For the two measurements times and gate interval $\tau = 1$ ms, the detectable limit levels are $SNR_{lim}(3\text{ s},1\text{ ms}) = 3.2\pm0.3$ and $SNR_{lim}(300\text{ s},1\text{ ms}) = 4.0\pm0.2$ with corresponding detectable laser frequency deviations $A_{lim} = 86\pm8$ kHz respectively $A_{lim} = 10.8\pm0.5$ kHz. In addition, for comparison with the previous paragraph and measurement times 5 and 500 s, the corresponding detectable frequency deviations are $A_{lim} = 68\pm5$ kHz s and $A_{lim} = 8.6\pm0.4$ kHz, respectively.
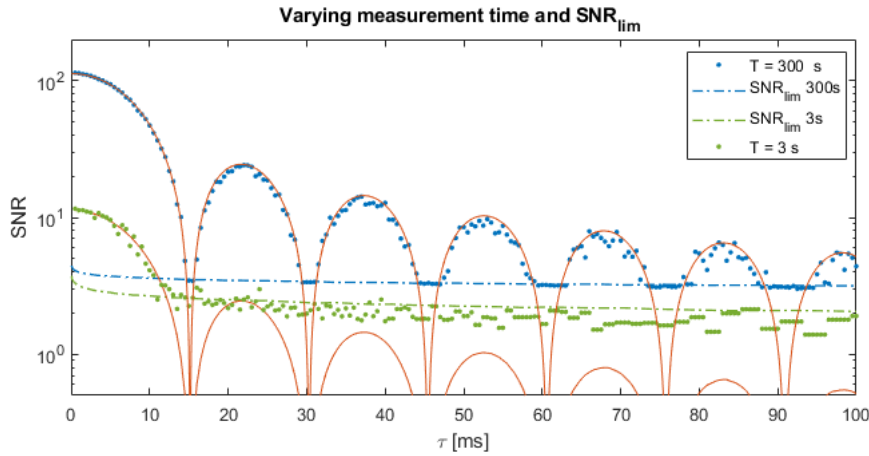

Fig. 6. Signal-to-noise ratio data for 3 s and 300 s measurement of fluorescence with harmonically modulated analyzed laser detuning Δ_{866}. Modulation frequency and frequency deviation are fixed to 66 Hz and 300 kHz, respectively. The signal amplitudes are found as the maximum of the whole frequency spectrum except DC. The full circles show the measured data, red lines depict the corresponding simulated values. Dashed lines represent numerical limits given by simulated signal with Poisson distribution SNR_{lim}.

4.4 Measurement point

We have further searched for optimal measurement point by characterization of the reciprocal dependence of the SNR on the count rate R, as shown in Fig. 7. Measurements of $SNR(R)$ for two modulation frequencies $f_m = 12$ Hz and $f_m = 120$ kHz with $A = 300$ kHz are realized along the dark resonance spectrum by changing the frequency detuning measurement point Δ_M. Gate interval τ is chosen such that $\text{sinc}(f_m,\tau) > 0.99$. At each measurement point, the average SNR of ten measurements with $T = 10$ is compared with theoretical SNR calculated using the slope

parameter m obtained directly from the measured fluorescence spectrum. Furthermore, the ratio between the measured results of the two f_m sets shows a decrease of SNR for the signal with $f_m > R$ and that this decrease is proportional to $\sim 1/R$.
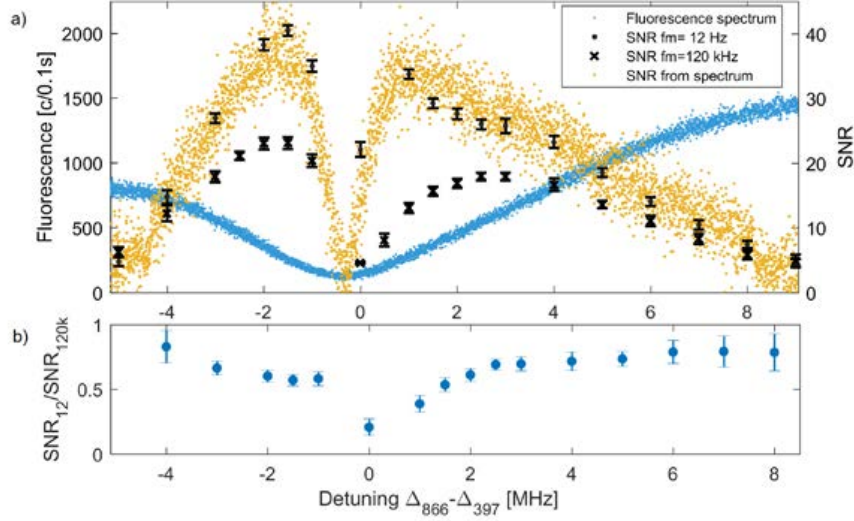

Fig. 7. a) The comparison of achievable signal-to-noise ratios for frequency analysis with various reference laser detuning. The detected fluorescence rates across dark resonance are shown as blue dots and the measured signal-to-noise data for 20 measurement points are shown for two modulation frequencies f_m of 12 Hz and 120 kHz depicted as black dots and crosses, respectively. The yellow dots are theoretical SNR data calculated from the measured dark resonance. Plot b) shows the ratio between measured SNR for the two modulation frequencies.

5. Results and Discussion

We have proposed and implemented a method for the estimation of optical frequency spectrum using the time resolved measurement of light scattered from a single trapped ion with a sensitivity enhanced by the excitation on the slope of dark resonance. Fluorescence rate sensitivity to laser frequency deviation A is given by the slope function of the dark resonance m, which depends on the parameters of applied magnetic and laser fields. The measurement point Δ_{M1} stands on the slope, whose length in the axis of frequency detuning has been set by the parameters of excitation lasers approximately to 8 MHz. This gives us the fundamental upper limit of the presented method on the frequency deviation and modulation frequency. According to the Carson rule for frequency modulation bandwidth with 98% of modulation energy [22], combined frequency deviation and modulation frequency has to satisfy the condition $2(A+f_m) \approx 8$ MHz, this condition was well satisfied for all presented measurements. The smallest detectable modulation amplitudes are limited by the amount of fluorescence noise. In terms of signal to noise ratio, this limit is defined in two approaches; when the signal part is taken from real data at specific frequency – SNR_{pl} and when the signal part is taken in the whole FFT spectrum of simulated data – SNR_{lim}. Specifically for measurements at measurement point Δ_{M1} the empirical limit is measured as $SNR_{pl} = 1.8\pm0.4$, which corresponds to the lowest detectable frequency modulation $A_{pl} = 38\pm8$ kHz for $T = 5$ s or $A_{pl} = 3.8\pm0.8$ kHz for $T = 500$ s. The simulated limit scales up with measurement time, however the mean level of amplitudes of noise frequency spectrum N is proportional to $\sqrt{R\tau/T}$ thus the lowest detectable frequency deviation scales down with longer measurement times. The corresponding detectable frequency deviations in our setup are $A_{lim} = 68\pm5$ kHz for $T = 5$ s and $A_{lim} = 8.6\pm0.4$ kHz for $T = 500$ s.

The detectable modulation frequency should be, according to the presented theory Eq. (5), unlimited. However, the measurement results show a decrease of $SNR(f_m, \tau)$ for high modulation frequencies. The decrease has been observed for modulation frequencies higher than the photon

count rate R, where signals start to be undersampled. Comparisons of SNR for two modulation frequencies $f_m = 12$ Hz and $f_m = 120$ kHz measured at 20 points along the dark resonance indicate a correlation of the decrease with fluorescence intensity, although the theoretical simulation shows that the undersampling itself should not limit the observable modulation frequency detection bandwidth. Simulation results did not show any decrease of SNR, even for an order of magnitude higher modulation frequencies observed with the same photon rate. Other possible effects, including leaking of the spectral modulation sidebands out of the resonance slope or the frequency response of the AOM, were also investigated and do not explain the observable decrease of SNR. Thus, at this point, we leave the attainable bandwidth limit of the presented method, as well as the studies if possible excitation of the motional sidebands within the employed Raman excitation scheme might play a role, for further investigation.

The atomic level scheme that enables observation of dark-states in emitted fluorescence is occurring among vast majority of species commonly employed in ion trap experiments. Different branching ratios of the decay constants leads to different spectral shapes of the fluorescence. In general, the optimal spectral shape will depend on experimental parameters such as detuning of a cooling laser, laser intensities and strength and direction of applied magnetic field. A lower intensity and lower detuning of the cooling laser should always lead to narrower resonances and higher fluorescence gradients. On the other hand, such adjustment decreases the spectral width of dark resonances thus limiting spectral bandwidth of the method, also decreases fluorescence rate, and leads to unstable Doppler cooling performance. We provide a simplified comparison of $^{40}Ca^+$ with other frequently employed alkaline earth metal ions, such as $^{88}Sr^+$ and $^{138}Ba^+$ by estimating the values of fluorescence gradients on the same lambda scheme incorporating $S_{1/2}$, $P_{1/2}$ and $D_{3/2}$ levels. This is done by simulating dark resonance spectra, using optical Bloch equations and the same experimental parameters as described in section 2. For $^{40}Ca^+$ the highest gradient is on transition between Zeeman states $|S_{1/2},-1/2\rangle$ and $|D_{3/2},-1/2\rangle$ with $m_{(-1/2,-1/2)} = 2.3$ counts·s^{-1}·kHz^{-1}. For $^{88}Sr^+$ it is $m_{(-1/2,-1/2)} = 2.4$ counts·s^{-1}·kHz^{-1} and for $^{138}Ba^+$ the highest gradient is on transition between states $|S_{1/2},+1/2\rangle$ and $|D_{3/2},+1/2\rangle$ with value $m_{(+1/2,+1/2)} = 2.6$ counts·s^{-1}·kHz^{-1}. In practice, a better Doppler cooling performance and smaller broadening of resonances by motion for the heavier elements should increase the attainable gradients and higher detection efficiency at strontium's 422 nm and barium's 493 nm wavelengths can enhance the sensitivity of the method too.

The presented method of optical frequency analysis has been verified in a range of experimental parameters. The observed sensitivity to frequency deviations and achievable spectral bandwidths, which are in good agreement with theoretical model, are already sufficient for a large range of interesting applications in the optical spectral analysis [23]. Besides the techniques employing optical frequency combs, it offers an alternative method for frequency analysis of spectral noise of two frequencies of very distant lasers, which can excite transitions in atomic probes sharing a common level. The method can be extended to analysis of complementary experimental platforms for atomic trapping in optical lattices or tweezers. Another natural application of the presented scheme corresponds to analysis and phase locking of the two lasers for the purposes of coherent operations on Raman transitions incorporating two disparate wavelengths [7]. In addition, the method can be directly applied to spectral noise analysis of magnetic field seen by the ion. This simple sensing scheme with spatial resolution on the level of tens of nm can be beneficial when the knowledge of spatial dependence of the magnetic field within the Paul trap is of interest. Such knowledge is essential e.g. for quantum algorithms where multiple ions are stored at different locations of a segmented Paul trap and accumulate undesired position-dependent phases [24]. In comparison with traditional spectroscopy on narrow transitions or with direct analysis on dark resonances, this method can provide complete information of magnetic field change in time. The presented lowest detectable laser frequency deviations for $T = 500$ s would allow for detecting magnetic field deviations of $B_{pl} = 1.9\pm0.3$ mG and $B_{lim} = 2.8\pm0.1$ mG in the corresponding frequency range. The sensitivity

of the detectable fluorescence rate to the analyzed probe frequency deviations can be further improved by increasing the overall fluorescence detection efficiency, which has been in our case limited mostly by numerical aperture of the collection optics to 2% of the full solid angle. The other feasible option is to increase the number of trapped ions. Both approaches will linearly enhance fluorescence intensity and thus the steepness of the dark resonance slope.

Funding

Disclosures

The authors declare no conflicts of interest.

References

1. C. Cohen-Tannoudji and D. Guéry-Odelin, *Advances in atomic physics : an overview* (World Scientific, Singapore ; Hackensack, NJ, 2011), pp. xxv, 767 p.
2. "Atomic physics: precise measurements and ultracold matter," Choice: Current Reviews for Academic Libraries **51**, 1846-1846 (2014).
3. A. Predojevic and M. W. Mitchell, "Engineering the Atom-Photon Interaction: Controlling Fundamental Processes with Photons, Atoms and Solids," Nanopt Nanophoto, 1-405 (2015).
4. A. D. Ludlow, M. M. Boyd, J. Ye, E. Peik, and P. O. Schmidt, "Optical atomic clocks," Rev Mod Phys **87**, 637-701 (2015).
5. D. Hayes, D. N. Matsukevich, P. Maunz, D. Hucul, Q. Quraishi, S. Olmschenk, W. Campbell, J. Mizrahi, C. Senko, and C. Monroe, "Entanglement of Atomic Qubits Using an Optical Frequency Comb," Phys Rev Lett **104**(2010).
6. A. G. Paschke, G. Zarantonello, H. Hahn, T. Lang, C. Manzoni, M. Marangoni, G. Cerullo, U. Morgner, and C. Ospelkaus, "Versatile Control of Be-9(+) Ions Using a Spectrally Tailored UV Frequency Comb," Phys Rev Lett **122**(2019).
7. C. Solaro, S. Meyer, K. Fisher, M. V. Depalatis, and M. Drewsen, "Direct Frequency-Comb-Driven Raman Transitions in the Terahertz Range," Phys Rev Lett **120**(2018).
8. M. Collombon, C. Chatou, G. Hagel, J. Pedregosa-Gutierrez, M. Houssin, M. Knoop, and C. Champenois, "Experimental Demonstration of Three-Photon Coherent Population Trapping in an Ion Cloud," Phys Rev Appl **12**(2019).
9. H. Schnatz, B. Lipphardt, J. Helmcke, F. Riehle, and G. Zinner, "First phase-coherent frequency measurement of visible radiation," Phys Rev Lett **76**, 18-21 (1996).
10. S. W. Kim, "Combs rule," Nat Photonics **3**, 313-314 (2009).
11. S. T. Cundiff, J. Ye, and J. L. Hall, "Optical frequency synthesis based on mode-locked lasers," Rev Sci Instrum **72**, 3749-3771 (2001).
12. R. Holzwarth, T. Udem, T. W. Hansch, J. C. Knight, W. J. Wadsworth, and P. S. J. Russell, "Optical frequency synthesizer for precision spectroscopy," Phys Rev Lett **85**, 2264-2267 (2000).
13. M. Collombon, G. Hagel, C. Chatou, D. Guyomarc'h, D. Ferrand, M. Houssin, C. Champenois, and M. Knoop, "Phase transfer between three visible lasers for coherent population trapping," Opt Lett **44**, 859-862 (2019).
14. E. Arimondo, "Coherent population trapping in laser spectroscopy," Prog Optics **35**, 257-354 (1996).
15. I. Siemers, M. Schubert, R. Blatt, W. Neuhauser, and P. E. Toschek, "The Trapped State of a Trapped Ion - Line Shifts and Shape," Europhys Lett **18**, 139-144 (1992).
16. J. Rossnagel, K. N. Tolazzi, F. Schmidt-Kaler, and K. Singer, "Fast thermometry for trapped ions using dark resonances," New J Phys **17**(2015).
17. C. Lisowski, M. Knoop, C. Champenois, G. Hagel, M. Vedel, and F. Vedel, "Dark resonances as a probe for the motional state of a single ion," Appl Phys B-Lasers O **81**, 5-12 (2005).
18. D. Reiss, K. Abich, W. Neuhauser, C. Wunderlich, and P. E. Toschek, "Raman cooling and heating of two trapped Ba+ ions," Phys Rev A **65**(2002).
19. J. Eschner, G. Morigi, F. Schmidt-Kaler, and R. Blatt, "Laser cooling of trapped ions," J Opt Soc Am B **20**, 1003-1015 (2003).

20.   R. Loudon, *The quantum theory of light,* 3rd ed., Oxford science publications (Oxford University Press, Oxford ; New York, 2000), pp. ix, 438 p.
21.   N. Scharnhorst, J. B. Wubbena, S. Hannig, K. Jakobsen, J. Kramer, I. D. Leroux, and P. O. Schmidt, "High-bandwidth transfer of phase stability through a fiber frequency comb," Opt Express **23**, 19771-19776 (2015).
22.   J. R. Carson, "Notes on the theory of modulation," P Ire **10**, 57-64 (1922).
23.   N. Picque and T. W. Hansch, "Frequency comb spectroscopy," Nat Photonics **13**, 146-157 (2019).
24.   T. Ruster, H. Kaufmann, M. A. Luda, V. Kaushal, C. T. Schmiegelow, F. Schmidt-Kaler, and U. G. Poschinger, "Entanglement-Based dc Magnetometry with Separated Ions," Phys Rev X **7**(2017).

Research article 3

Frequency stabilisation of 729 nm external cavity diode laser with a combined approach using the high finesse cavity and transfer oscillator technique

M. T. Pham, M. Cizek, A. Lesundak, A. Kovalenko, P. Obsil, P. Jedlicka, L. Slodicka and O. Cip

Frequency stabilisation of 729 nm external cavity diode laser with a combined approach using the high finesse cavity and transfer oscillator technique.

T. M. Pham,[1, a)] M. Cizek,[1] A. Lesundak,[1] A. Kovalenko,[2] P. Obsil,[2] P. Jedlicka,[1] J. Lazar,[1] L. Slodicka,[2] and O. Cip[1]

[1)]*Institute of Scientific Instruments of the CAS, v. v. i.*

[2)]*Palacky University Olomouc*

(*Electronic mail: tuan@isibrno.)

(Dated: 3 July 2022)

Standard methods for stabilising laser for precision spectroscopy on trapped particles are either to lock it to the ultra-stable reference such as a high finesse cavity or a transfer-oscillator technique. Both of them used alone has their imperfections. Cavities are affected by environmental elements such as thermal dependent and ageing-related drift. On the other hand, the transfer-oscillator technique is limited by the complexity of the locking cascade of regulators. This paper demonstrates using only the best properties of both techniques and achieving a stable and precise laser for precision spectroscopy and experiment on the trapped calcium ion.

This paper report on a method of the frequency stabilisation and fast locking of the Extended cavity diode laser using the high finesse cavity and the transfer oscillator technique. We illustrate the effect of this implementation by analyzing the noise spectra of the laser and the benefits of suppressing it by using the laser to drive the narrow $|^2S_{1/2}, m = -1/2\rangle \leftrightarrow |^2D_{5/2}, m = -1/2\rangle$ transition of $^{40}Ca^+$ ion. The achieved result shows the increase in Ramsey coherence time by an order of two. Likewise the spectral purity of the laser show no residual noises in the area of the carrier.

I. INTRODUCTION

High spectral purity and coherence laser source is a crucial feature for many applications, such as atomic physic, high-resolution spectroscopy of trapped ions, coherent manipulation, and communication, to name a few. To acquire a stable and reliable laser source, one usually uses the conventional method by stabilizing the laser source onto ultra-stable references also known as hight finesse cavities (HF-cavity). They are made from material that has a very low expansion coefficient, like Ultra-low Expansion glass (ULE®) or a silicon single-crystal[1–3]. They are broadly used and already commercialized (Stable Laser Systems, Menlo Systems). The Important property of these cavities is that their fractional frequency instability of the longitudinal cavity mode directly relates to its fractional length instability. Thus the HF-Cavities serve as a very narrow frequency discriminator. Using the Pound-Drever-Hall (PDH)[4] locking technique one then can easily lock the spectroscopy laser into its length and achieve a laser with Hz or sub-Hz resolution.

[a)]Also at Institute of Scientific Instruments of the CAS, v. v. i.; https://www.isibrno.cz

What is more, one can find a relation between the finesse of the cavity and the locking process. The higher the finesse, the higher gain one can achieve in the control loop. In addition, perturbation added to the error signal, like residual amplitude modulation, will have a minor effect on the control loop. The finesse of these cavities is usually in the range of 10^5. The limitation of this technique lies in the Brownian thermo-mechanical noise[5,6] in the material, which directly leads to fluctuation of the optical length of the interferometer and thus changes the frequency stability of the laser stabilized to it. Using this method, one can also frequency stabilize only one laser. The stability of the laser stabilized by this method can reach 10^{-16} fractional instability.

Another stabilization method is by using a so-called Transfer-oscillator technique. This technique allows us to transfer the stability of the ultra-stable source into the stabilized laser. The advantage of this technique indeed arises when using it with the optical frequency comb (OFC), hereinafter referred to as comb. One can then realize many frequency locking stages for lasers at different wavelengths. The disadvantage lies in the complexity of the whole setup with many wideband servo loops that inevitably lead to the transfer also residual noise from the reference source into the resulting laser. By combining the advantages of both methods, we achieved a stable and precise laser source for high-precision spectroscopy on $|S_{1/2}\rangle \rightarrow |D_{5/2}\rangle$ atomic transitions of the $^{40}Ca^+$ ion. The HF-cavity, in this case, will deliver ultimate short-term stability while the long-term stability will be obtained using the transfer-oscillator as a fine-tuning against the cavity's slow drifts. Here we analyze the performance of the commercial extended-cavity laser (ECDL) working at 729 nm laser stabilized by the scheme mentioned above. Then we characterize the power spectral noise density (PSD) of this laser. We demonstrate the practical impact of this enhancement by performing a coherent state manipulation of the $|^2S_{1/2}, m = -1/2\rangle \rightarrow |^2D_{5/2}, m = -1/2\rangle$ transition on the trapped and laser-cooled $^{40}Ca^+$ ion.

II. EXPERIMENTAL SETUP AND METHODS

The whole experimental setup is schematically illustrated in Fig. 2. We use a linear Paul trap with four blades separated by 1.13 mm and two tip electrodes separated by 4.5 mm, providing the radial and axial confinement. By applying the radio frequency (RF) of 29.8 MHz and power of 4W to the trap radial electrodes and setting the mean tip voltage to 1200V, we achieve typical secular frequencies $omega_r/2\pi = 2.7 MHz$ in the radial and $omega_a/2\pi = 1.1 MHz$ in the axial direction. The single Ca^+ ion is loaded into the trap by photo-ionizing a beam of neutral calcium atoms. Everything is enclosed by an ultrahigh vacuum $> 10^{-11}$ mbar[7], sufficient isolation from the environment perturbation. Each optical axis is equip with a pair of coils allowing for generating the three axis magnetic field. We used a constant magnetic field of ≈ 3.2 G to split the $|S_{1/2}\rangle \to |D_{5/2}\rangle$ transition onto 10 Zeeman components. Choosing a good geometry for polarization, k-vector and magnetic field direction, we selected two transitions with good coupling strength for our experiments ($\Delta m = 0$ and $\Delta m = 2$). The whole trap apparatus is then situated inside a passive magnetic shield box to suppress the magnetic perturbation during the experiment.

For the spectroscopy laser used in our experiments, we have chosen an ECDL working at 729 nm (Toptica, TA Pro). The laser emits a spectrum with ≈ 300 kHz linewidth. This relatively broad linewidth does not fulfill the requirement for sufficient coherence time of many experiments (Ramsey interferometry or quantum memory[8]). It needs to be narrowed down by several orders of magnitude using an ultra-stable reference. The reference for stabilizing the spectroscopy laser is a high finesse cavity working at 729 nm (c729). The c729 is manufactured from ULE and purchased by Stable Laser Systems. With a finesse approx 3×10^5 and a free spectral range (FSR) of 3.14 GHz, a spectral linewidth of its mode is roughly 8 kHz. This provides enough room for detecting laser frequency changes down to sub-Hz level. To minimize the environmental vibrations on the resonator and thus reach a low level of thermal noise, the resonator is sealed in the vacuum chamber. The chamber is thermally stabilized with a Peltier element with the 1 mK stability and lies on the actively controlled vibration isolation table. As the cavity is mounted the way that the axis of the spacer is horizontally oriented, we have decided to minimize the sensitivity of the spacers for vertical vibrations by placing the whole setup on a 250 kg block of granite. The granite block lies on a fine sand bed, and a thermal isolation box then encloses the Whole setup. The temperature inside of the box is stabilized by a water cooling system (Fig. 1).

The laser beam travels to HF-cavity via a 10 m long polarization-maintaining optical fibre. As this long fibre takes many perturbations from the environment, such as temperature or acoustic pressure from the normal speech, it leads to a broadening of the spectrum towards the kilohertz domain[9,10]. To stabilize the fibre length in terms of cancellation of this induced phase noise, we apply the Fibre Noise Cancellation (FNC) technique involving the Michelson interferometer and an acousto optic modulator (AOM) placed before the fibre[11]
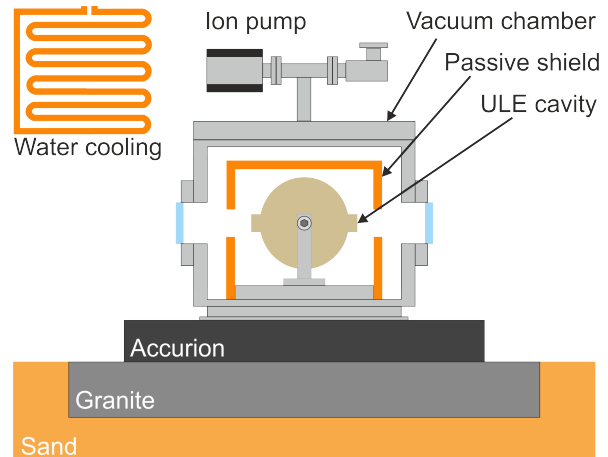

FIG. 1. Schematic of the vibration and thermal isolation platform including the vacuum chamber and the passive heat shield centered around the ULE cavity. Whole setup is then enclosed in the wooden box with thick layers of thermal isolation material.

(see the AOM3 in Fig. 2). Many other teams widely accepted and implemented this simple yet very effective correction scheme[9,12,13] for compensating short-term fractional frequency instabilities below 10^{-13}. The AOM3 driven by a radio frequency of 70 MHz is double passed with a retro-reflecting beam from the beam sampler (BS) at the fibre end. Laser beam propagated through the fibre will accumulate phase noise ϕ_f. Thus twice the fibre phase noise information will appear as phase shifts on the 140 MHz radio frequency (RF) beat note signal detected by the avalanche photodiode (APD) at the source end. The detected signal is processed by the digital Fibre Noise Cancellation controller (FNC control) where its instantaneous phase is compared to that of the RF reference by a phase detector producing an error signal. The error signal is processed by a digital loop filter and its output is relayed to a DDS driving AOM3. The bandwidth achieved by this control loop is approx. 40 kHz which is sufficient enough for compensating all common mechanical and acoustic vibrations effects. The digital fiber noise cancellation controller has already been described in more detail in our previous work[14].

Although the spectral line of L729 locked to the optical resonator using the above method is very narrow, its central frequency follows the slow drift of the HF-cavity resonant mode caused by Brownian thermal motion and ageing. To ensure repeatability of spectroscopic measurements this frequency needs to be tracked by comparing to an optical reference with a high long-term fractional frequency stability.

For reliable referencing of several concurrent experimental setups, our laboratory uses an ensemble of microwave and optical references, which is formed of an active Hydrogen maser (H-maser) (T4 Science iMaser 3000), highly coherent 1540.57nm laser and an optical frequency comb. The primary optical reference (L1540) consists of a narrow-linewidth (FWHM < 1 kHz) laser (NKT Koheras Basik) working at 1540.57 nm locked to a HF-cavity (ULE from Stable Laser

Systems) using the PDH technique to suppress the residual phase noise reducing its spectral linewidth to sub-Hz level. The finesse of the cavity is approx 4.5 x 10^5. The cavity is equipped with similar protective elements as previously mentioned 729. To correct the resonator's slow drift (70 mHz·s^{-1})[14], the laser output is coupled into the femtosecond optical frequency comb setup. The comb is used in a regime that is referred to as the optical frequency divider. In this regime the offset frequency of the COMB f_{ceo} is locked to RF reference derived from a H-maser. The repetition frequency f_{rep} of the comb is actuated so the distance of the comb tooth nearest to the L1540 remains constant. All changes made to the optical frequency of L1540 are thus transmitted proportionally to the f_{rep}. By a sensitive phase demodulator (6.14×10^{-6} rad resolution), the phase of the RF signal produced by a photo detector monitoring f_{rep} of the comb is compared to that of a 250MHz reference signal derived from the H-maser. This error signal is then processed by a loop filter steering the driving frequency of AOM4 so the phase difference remains zero. This leads to a CW laser output after AOM5 that has its high coherence given by the PDH lock to the cavity and long-term relative frequency stability same as that of the H-maser. Also the teeth in OFC spectrum adopt their coherence from the L1540 laser and the long-term fractional stability of the teeths' frequencies is given by locking to the H-maser.[14]

The OFC is equipped by the fundamental output especially for beating with CW lasers in the infra red C-band and the second-order harmonic output in the visible part of the spectrum generated by the SHG unit. The fundamental comb spectrum can be expressed as $\nu_k = f_{ceo} + k \cdot f_{rep}$, where ν_k is the optical frequency of a comb tooth with index $k \in N$. The second-order harmonic comb spectrum generated by the SHG unit can be expressed as $\nu_k = 2 \cdot f_{ceo} + k \cdot f_{rep}$. This second-order harmonic output is used for measuring the drift of the L729. The transfer oscillator technique with signal conditioning described further is used for producing a virtual beat note signal between L729 and the L1540 reference laser.

As it was said, the beat note between L1540 reference laser and the nearest comb tooth with index of k_{1540} is phase locked to a RF reference by actuating f_{rep}. Any residual frequency deviations of the L1540 beat are thus translated via the f_{rep} to deviations of the optical frequency of the comb tooth with indexed of k_{729} closest to the L729 laser. The L1540 beat frequency deviations translated to the L729 beat detected at PD3 can be expressed as $\Delta \nu_1 = \pm \Delta \nu_{L1540} \cdot k_{729}/k_{1540}$. To subtract this multiplied frequency noise from the L729 beat detected by PD3, the frequency of L1540 beat signal detected by PD4 is multiplied by ratio of k_{729}/k_{1540} using DDS3 (by ≈ 2.112 in our case) and then mixed with the L729 beat. The "$\pm$" sign denotes that the beat frequency deviation can be both positive or negative multiple of the actual CW laser optical frequency deviation. It depends on whether the laser frequency is higher or lower than the optical frequency of the nearest comb tooth.

The f_{ceo} of the OFC is locked to the RF reference derived from the H-maser. Since the f_{ceo} lock has a bandwidth limited by approx. 9 kHz, there is some non-negligible frequency noise from the comb pump laser present at higher Fourier fre-

quencies of the f_{ceo} signal. This frequency noise is present in the L1540 beat as well and thus translated via the f_{rep} in the same way as described in the previous paragraph. We can express the f_{ceo} contribution to the L729 beat frequency noise as: $\Delta \nu_2 = \pm 2 \cdot \Delta f_{ceo} \pm \Delta f_{ceo} \cdot k_{729}/k_{1540}$. To subtract this residual f_{ceo} noise from the beat signal detected by PD3, the f_{ceo} signal from the comb is frequency multiplied by DDS2 (by ≈ 0.112 in our case) and mixed with the mixing product described in the previous paragraph.Finally we get the virtual beat note signal between L729 and L1540 that is cleaned from the comb f_{ceo} noise and free of noise multiplied through the f_{rep}.

In order to obtain a long-term frequency stable L729 with a narrow spectral emission line the transfer beat signal can be principally used in two ways. The most straightforward method implemented by various teams is to use the virtual beat signal directly in a wide band servo loop to lock L729 to L1540. The main advantage of this solution is that it does not require locking L729 to the c729 H-F cavity[15–17]. However as it will be shown in Section III a high-bandwidth PLL can imprint certain high-frequency noise into the resulting laser emission spectrum. The source of this residual noise may be in the main optical reference, in servo-loops stabilising the OFC or in the RF signal conditioning electronics.

The method used by our team utilizes the virtual beat signal for precise monitoring of long-term frequency drifts of L729 locked to the c729 H-F cavity. To compensate this drift actively the virtual beat signal is followed by a tracking oscillator (TO) as shown in Fig. 2. In order to reject majority of fibre-induced and other technical high-frequency noise, the tracking oscillator bandwidth is set to $\approx$5 Hz. A correction computed by the controller is applied to AOM2 keeping the resulting L729 optical frequency long-term stable. This solution reduces the number of high-speed servo loops in the cascade interacting with the L729 from four (L1540 P-D-H lock, OFC f_{rep} lock to L1540 optical reference, OFC f_{ceo} lock to RF reference, L729 transfer beat lock to just one, which is the P-D-H lock of L729 to the c729 H-F cavity.

III. MEASUREMENTS AND RESULTS

All the presented measurements involving the $^{40}Ca^+$ were measured in the $|^2S_{1/2}, m = -1/2\rangle \leftrightarrow |^2D_{5/2}, m = -1/2\rangle$ transition ($\Delta m = 0$) as it is least sensitive to magnetic fluctuation. The pulse sequence cycle consists of 1 ms of Doppler cooling on $S_{1/2} \leftrightarrow P_{1/2}$ at a wavelength of 397 nm and 866 nm as a repumper. The state initialization step consists of wavelength 854 nm to prevent pumping into $D_{5/2}$ and an optical pumping into $|^2S_{1/2}, m = -1/2\rangle$. After that, we use the L729 frequency stabilized by the method mentioned above to carry out the experiment on the $|^2S_{1/2}, m = -1/2\rangle \leftrightarrow |^2D_{5/2}, m = -1/2\rangle$ transition.

The Ramsey spectroscopy is perfectly suited for a test of qubit's decoherence[18]. The experiment consists of two $\pi/2$ pulses with probe time duration $20\mu s$ separated by a waiting time τ_R. After applying the second pulse, the state of the ion was detected by electron shelving using the APD for fluores-
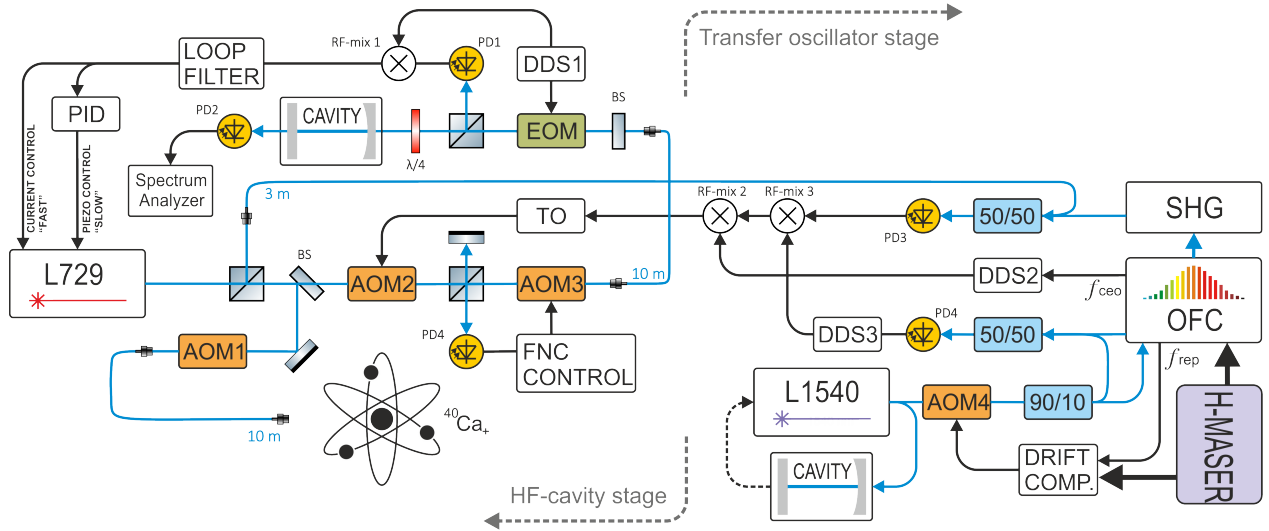
FIG. 2. Setup for the frequency stabilization of an ECDL L729 to an ensemble of references formed of H-Maser, L1540 and optical frequency comb. PID: Proportional-integral-derivative controller, DDS: Direct digital synthesizer, Drift comp.: L1540 resonator cavity drift compensation controller, AOM: Acousto-optic modulator, TO: Transfer oscillator, EOM: Electro-optic modulator, SHG: Second harmonic generation, FNC: Fiber noise cancelation controller[14], x/y: Fiber optic coupler

cence detection. Each experiment was repeated 100 times to obtain an excitation probability. Ideally, the excitation to $D_{5/2}$ should exhibit the modulation between zero and one when changing the phase between two pulses. The loss of contrast in this observed pattern is caused by a dephasing of the qubit levels when the superposition of the $|S\rangle$ and the $|D\rangle$ is exposed to decoherence for a long time. We have systematically measured the Ramsey contrast for varied delay times between two pulses (5 μs up to 10000 μs). Each data set was fitted to a sinusoidal function to get the final contrast. The observed contrast $C = P_D^{max} - P_D^{min}/P_D^{max} + P_D^{min}$ was plotted versus the delay time in Fig. 4.

To describe the decrease of contrast we fit the measured data with a Gaussian function. The resulting laser linewidth achieved from the fit is $\Delta_{\nu_{FWHM}} = 28.9$ Hz correspond to Ramsey time of 7.64 μs. For comparison to the same measurement with L729 locked to L1540 using the virtual beat signal directly in a wide band servo loop, the resulted laser linewidth was 57.3 Hz, which correspond to Ramsey time of 3.65 μs. Thus with our proposed method, when L729 is locked to c729 and using the virtual beat signal as a slow-tuning tool, we increased the Ramsey contrast by an order of two. For the comparison, we also measured the Ramsey contrast for $\Delta m = 2$ with a similar result.

Many experiments, such as those in trapped ion simulation and quantum computing, require a few-μs to few-ten-μs pulses, thus a relatively high laser intensity. The high laser intensity will manifest the spectrum in terms of power broadening and will reduce the measurement's fidelity. The Fig. 4) demonstrate the frequency spectrum over the $\Delta m = 0$ transition with L729 stabilized to the HF-cavity length as a primary stable reference and using the transfer beat signal only for correcting the resonant frequency drift. The fidelity ob-
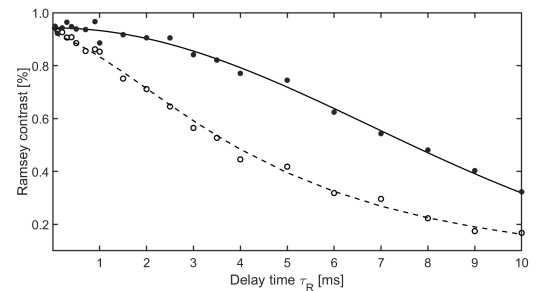

FIG. 3. The Contrast of the Ramsey pattern as a function of the delay time. Both (solid and open) circles are the data measured on the same Zeeman component ($|^2S_{1/2}, m = -1/2\rangle \leftrightarrow |^2D_{5/2}, m = -1/2\rangle$) and with the same waiting time (τ_R). Open circles represent measurement when the L729 was locked to the virtual transfer beat. Solid circles represent the measurement when the L729 was referenced by HF-cavity length and its drift compensated using the transfer oscillator technique. The coherent time was extended nearly twice

tained using this method is 99%. For comparison, we add the same spectral line scanned with the L729 locked directly to the using the transfer beat signal. One can see that the spectrum also contains the broadening caused by residual high-frequency noise from the servo. The excitation contrast is limited 94%. In both cases, the laser intensity was stabilized so that the π pulse remains 25μs.

To illustrate the possible mechanism of frequency noise imprinting to the resulting L729 spectral emission profile Fig. 5 shows frequency noise power spectrum density of f_{ceo} and L1540 beat signals used for generating the transfer beat signal. These plots are compared to actual out-of-loop frequency
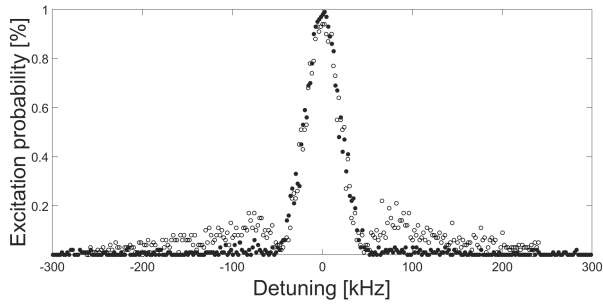
FIG. 4. Spectroscopy of the $|^2S_{1/2}, m=-1/2\rangle \leftrightarrow |^2D_{5/2}, m=-1/2\rangle$ transition with L729 locked to the virtual beat we obtain 94% excitation contrast (open circle). With L729 locked to HF-cavity and steered with transfer beat signal, the excitation contrast was measured over 99% (filled circles). In both measurements the laser L729 was intensity stabilized so that the π pulse remain always $25\mu s$
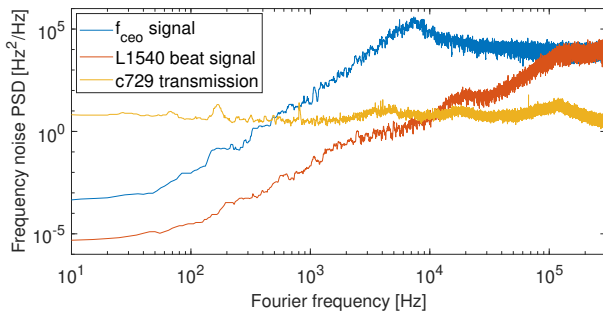

FIG. 5. The illustration of imprinting frequency noise while locking L729 directly to the virtual transfer beat. Frequency noise power spectrum density of f_{ceo} (blue) signal and L1540 beat signal (red) used for generating the transfer beat signal compared to that of L729 obtained with c729 working as a frequency discriminator (yellow).

noise measured using the c729 working as frequency discriminator. Note that the response of the discriminator was corrected based on the knowledge of its ring-down decay time constant. One can see that side-band peaks visible in Fig. 4 correspond to noise peaks visible on the L729 frequency noise PSD plot in Fig. 5. These peaks correspond to excess noise visible in the transfer beat input signals. Although these signals contain useful information at most the extra noise is difficult to overcome. Therefore using the transfer beat only in slow servo loops with bandwidth below 1 kHz can be seen as an effective engineering solution.

IV. CONCLUSION

For decades atomic frequency standards played a critical role in basic science and precision measurement. During this period, the increasing need for more precise timing and synchronisation for a wide range of applications, including navigation, synchronisation or test of fundamental physic, has demanded oscillators with higher frequencies and higher perfor-

mance. To excite those oscillators coherently, a high spectra purity of the laser source is a crucial feature and stabilisation techniques have constantly been renewed and developed over time.

A commonly used technique is stabilising the laser optical frequency to an ultra-stable length of the high-finesse cavities. However, the cavity is a physical component, and thus it is susceptible to environmental perturbations from which it needs to be isolated. Even well isolated, the cavity exhibit a slow drift due to Brownian thermal motion and the ageing effect. In our case, it is approximately 0.3 Hz·s^{-1}, which reduces the laser's liability and fidelity of the measurement. Another commonly used technique is to transfer the stability from an ultra-stable master source into a laser using the mediator. However, due to the complexity of this technique, it can lead to transferring the residual noise from wide band servo loops into the resulting laser.

To overcome the shortcoming of both stabilisation techniques, we propose an implementation setup where only the best feature of both techniques is used. The short-term stability is full-filed by locking the L729 to the c729 HF-cavity, while the long-term stability is achieved by utilising the virtual beat signal for precise monitoring and servo-loop frequency correction of c729 HF-cavity. In this case, the only wide band servo loop interacting directly with L729 is the P-D-H lock to the resonator.

We demonstrate the practical impact of this method by performing a coherent manipulation on the $|^2S_{1/2}, m=-1/2\rangle \leftrightarrow |^2D_{5/2}, m=-1/2\rangle$ narrow transition of the $^{40}Ca^+ ion$. The finite laser coherence value was estimated through a Ramsey separated oscillating field method. The resulting laser linewidth is calculated from the fit over the set of measured Ramsey contrasts. Our implementation results in Ramsey time of 7.64, correspond to laser linewidth μs $\Delta_{\nu_{FWHM}} = 28.9$ Hz. This is near twice the improvement compared to when the virtual beat signal is directly used in a wide band servo loop for locking the L729 to L1540. Many experiments demand a pulse's length in a few milliseconds range. In this regime, the power broadening caused by high laser power operation can magnify the residual noises that are contained in the spectra. In our case, the only wide band servo loop is the P-D-H lock with a bandwidth of a few kHz. Thus the higher frequency noises are suppressed. This is demonstrated in the measured transition spectra of the ion. We do not intend to claim the novelty of this implementation as a breaking new method for locking the optical frequencies but rather to present an additional way of enhancing the yet-existed and well-developed method.

[1] T. Kessler, C. Hagemann, C. Grebing, T. Legero, U. Sterr, F. Riehle, M. J. Martin, L. Chen, and J. Ye, "A sub-40-mhz-linewidth laser based on a silicon single-crystal optical cavity," Nature Photonics **6(10)** (2012).

[2] B. C. Young, F. C. Cruz, W. M. Itano, and J. C. Bergquist, "Visible lasers with subhertz linewidths," Phys. Rev. Lett. **82** (1999).

[3] J. Alnis, A. Matveev, N. Kolachevsky, T. Udem, and T. W. Hänsch, "Sub-hertz linewidth diode lasers by stabilization to vibrationally and thermally compensated ultralow-expansion glass fabry-pérot cavities," Physical Review A **77(5)** (2008).

[4] P. W. R. Drever, L. J. Hall, and V. F. Kowalski, "Laser phase and frequency stabilization using an optical resonator," Appl. Phys. (1983,).

[5] T. Kessler, T. Legero, and U. Sterr, "Thermal noise in optical cavities revisited," NJOSA B **29** (2012).

[6] K. Numata, A. Kemery, and J. Camp, "Thermal-noise limit in the frequency stabilization of lasers with rigid cavities," Phys. Rev. Lett. **93** (2004).

[7] P. Obšil, A. Lešundák, T. Pham, K. Lakhmanskiy, L. Podhora, M. Oral, O. Číp, and L. Slodička, "A room-temperature ion trapping apparatus with hydrogen partial pressure below 10^{-11} mbar," Rev. Sci. Instrum. **90** (2019).

[8] P. Wang, C.-Y. Luan, M. Qiao, M. Um, J. Zhang, Y. Wang, X. Yuan, M. Gu, J. Zhang, and K. Kim, "Single ion qubit with estimated coherence time exceeding one hour," Nature Communications **12** (2021).

[9] L. S. Ma, P. Jungner, J. Ye, and J. L. Hall, "Delivering the same optical frequency at two places: accurate cancellation of phase noise introduced by an optical fiber or other time-varying path," Optics Letters **19** (1994).

[10] P. A. Williams, W. C. Swann, and N. R. Newbury, "High-stability transfer of an optical frequency over long fiber-optic links," J. Opt. Soc. Am. B, JOSAB **25** (2008).

[11] O. Lopez, A. Haboucha, B. Chanteau, C. Chardonnet, A. Amy-Klein, and G. Santarelli, "Ultra-stable long distance optical frequency distribution using the Internet fiber network," Optics Express **20**, 23518–23526 (2012), publisher: Optica Publishing Group.

[12] A. Didier, S. Ignatovich, E. Benkler, M. Okhapkin, and T. E. Mehlstäubler, "946-nm Nd:YAG digital-locked laser at $1.1x10^{-16}$ in 1 s and transfer-locked to a cryogenic silicon cavity," Optics Letters **44**, 1781–1784 (2019), publisher: Optica Publishing Group.

[13] B. Rauf, C. V. Lopez, Maria, P. Thoumany, M. Pizzocaro, and D. Calonico, "Phase noise cancellation in polarisation-maintaining fibre links," Review of Scientific Instruments **89** (2018).

[14] M. Cizek, L. Pravdova, M. T. Pham, A. Lesundak, J. Hrabina, J. Lazar, T. Pronebner, E. Aeikens, J. Premper, O. Havlis, R. Velc, T. Schumm, J. Vojtech, A. Neissner, and O. Cip, "Coherent fibre link for synchronization of delocalized atomic clocks," Optics Express **30(4)**, 15 (2022).

[15] N. Scharnhorst, J. B. Wübbena, S. Hannig, K. Jakobsen, J. Kramer, I. D. Leroux, and P. O. Schmidt, "High-bandwidth transfer of phase stability through a fiber frequency comb," Optics Express **23(15)** (2015).

[16] H. Telle, B. Lipphardt, and J. Stenger, "Kerr-lens, mode-locked lasers as transfer oscillators for optical frequency measurements," Applied Physics B: Lasers and Optics **74** (2002).

[17] J. Stenger, H. Schnatz, C. Tamm, and H. R. Telle, "Ultraprecise measurement of optical frequency ratios," Physical Review Letters **88** (2002).

[18] F. Schmidt-Kaler, S. Gulde, M. Riebe, T. Deuschle, A. Kreuter, G. Lancaster, C. Becher, J. Eschner, H. Haffner, and R. Blatt, "The coherence of qubits based on single $^{40}ca^+$ ions," Journal of Physics B: Atomic, Molecular and Optical Physics **36(3)**, 13 (2003).

[19] G. D. Domenico, S. Schilt, and P. Thomann, "Simple approach to the relation between laser frequency noise and laser line shape," Applied Optics **49(25)** (2010).

[20] N. Bucalovic, V. Dolgovskiy, C. Schori, P. Thomann, G. di Domenico, and S. Schilt, "Experimental validation of a simple approximation to determine the linewidth of a laser from its frequency noise spectrum," Applied Optics **51(20)** (2012).

[21] G. Xu, D. Jiao, L. Chen, L. Zhang, R. Dong, T. Liu, J. Wang, and S. Zhang, "Analysis of vibration sensitivity induced by the elastic deformation of vertical optical reference cavities," IEEE Access **8** (2020).

[22] C. Salomon, D. Hils, and J. L. Hall, "Laser stabilization at the milihertz level," The Journal of the Optical Society of America. (1988).

[23] D. Leibfried, R. Blatt, C. Monroe, and D. Wineland, "Quantum dynamics of single trapped ions," Rev. Mod. Phys. **75** (2003,).

[24] W. Demtroder, "Laser spectroscopy, basic concepts and instrumenta-tion, third edition," Springer (2003).

Appendix IV

Curriculum vitae

PERSONAL INFORMATION

Pham Minh Tuan

📍 Královopolská 147, 612 64 Brno, Czech Republic

📞 +420 541 514 532   📠 +420 731 819 893

✉ tuan@isibrno.cz

🌐 http://www.isibrno.cz/

Sex Male | Date of birth 05/05/1988 | Nationality Czech Republic / Viet Nam

WORK EXPERIENCE

2014-onwards

Ph.D. Student

Institute of Scientific Instruments, Czech Academy of Sciences, Královopolská 147, 612 64 Brno, Czech Republic

- Frequency stabilization of laser working at 729 nm for ion cooling.
- Research in laser optics and laser spectroscopy with trapped and cooled Ion.
- Vacuum technology, design and assembly of new apparatus.
- High finesse optical resonators and stabilisation techniques.

Science, optics, metrology

2012-onwards

Technologist of DBR diode lasers

Institute of Scientific Instruments, Czech Academy of Sciences, Královopolská 147, 612 64 Brno, Czech Republic

- Technology and investigation of broad tunable narrow-linewidth diode laser working at 633 nm for metrology and molecular spectroscopy.

Science, optics, metrology

EDUCATION AND TRAINING

2014-onwards

Doctoral study, Ph.D.   ISCED6

Brno University of Technology, Faculty of Mechanical Engineering, Institute of Physical Engineering, program Physical and Material Engineering

- Ph.D. Thesis: " Single-frequency laser with narrow spectral linewidth for cold ion spectroscopy"

2012-2014

Master study, Dipl.- Ing.   ISCED5

Brno University of Technology, Faculty of Electrical Engineering and Communication, Institute of Biomedical Engineering, study program Biomedical Engineering and Bioinformatics.

- Diploma thesis: "Analysis of volumetric change of hippocampus caused by Alzheimer's disease", a development of software for analysing and segmentation of 3D data from MRI.

05-06/2018

Visiting researcher"

The National Physical Laboratory, GB

- building and characterising an Yb+ ion trap for use in Host's optical atomic clock. Building an optical and electrical infrastructure for stabilising an optical frequency on high finesse cavity.

06/2017

Professional course "Time and Frequency seminar"

The National Institute of Standards and Technology, US

- optical clock, oscillators, atomic frequency standards, quantum information, phase-noise measurements

8/2016

Visiting researcher"
The Observatoire de Paris, France
- Frequency tripling of telecom laser diode
- Stabilisation of the lase to iodine hyperfine line

07/20016, 1 week

The 26th International Travelling Summer School on Microwaves and Lightwaves
L´Aquila, Italy

- Laser instrumentation, optics, terahertz technologies and application.

PERSONAL SKILLS

Mother tongue(s)

Vietnamese

Other language(s)

UNDERSTANDING		SPEAKING		WRITING
Listening	Reading	Spoken interaction	Spoken production	
C2	C2	C1	C1	C1
B2	B2	B2	B2	B1

Czech (C2, C2, C1, C1, C1)
English (B2, B2, B2, B2, B1)

Communication skills

Ability to work and communicate in teams. Good communication adaptation due to many international visited work travels and conference in different fields of interest.

Organisational / managerial skills

Doctoral and high school studies and managerial skills gained through managing of investigated projects. Organisational and pedagogic skills gained through experiences from many years of leading sport and health related clubs.

Job-related skills

Experience gained through daily experimental laboratory work with optics and optomechanics. Design and realization of vacuum and optomechanical assembly. Collecting and processing measured data.

Computer skills

Routine usage of PC, office SW, Corel Draw, programming and processing of scientific data in MATLAB computational SW, programming and controlling of experiments in LabVIEW, Design of electronic circuits and printed circuit boards via system Eagle. Design of mechanical parts using Autodesk Inventor.

Driver licence

B

ADDITIONAL INFORMATION

Applied research results

Product:1
Software for segmentation and measuring of volume of hippocampus, 2014

Honours and awards

2016 – Award of the ITSS (International Travel Summer School on Microwaves and Lightwaves) – First place for team project.

PUBLICATIONS

Journals

- Obšil, P., Lešundák, A., Pham, T., Lakhmanskiy, K., Podhora, L., Oral, M., Číp, O., & Slodička, L. (2019). *A room-temperature ion trapping apparatus with hydrogen partial pressure below 10−11 mbar*. *Review of Scientific Instruments*, *90*(8), 083201. https://doi.org/10.1063/1.5104346

- Lešundák, A., Pham, T. M., Čížek, M., Obšil, P., Slodička, L., & Číp, O. (2020). *Optical frequency analysis on dark state of a single trapped ion*. *Optics Express*, *28*(9), 13091. https://doi.org/10.1364/oe.389411

- Podhora, L., Pham, T., Lešundák, A., Obšil, P., Čížek, M., Číp, O., Marek, P., Slodička, L., & Filip, R. (2020). Unconditional accumulation of nonclassicality in a single-atom mechanical oscillator. *Advanced Quantum Technologies*, *3*(11), 2000012. https://doi.org/10.1002/qute.202000012

- Obšil, P., Lachman, L., Pham, T., Lešundák, A., Hucl, V., Čížek, M., Hrabina, J., Číp, O., Slodička, L., & Filip, R. (2018). Nonclassical light from large ensembles of trapped ions. *Physical Review Letters*, *120*(25). https://doi.org/10.1103/physrevlett.120.253602

- Obšil, P., Lešundák, A., Pham, T., Araneda, G., Čížek, M., Číp, O., Filip, R., & Slodička, L. (2019). *Multipath interference from large trapped ion chains*. *New Journal of Physics*, *21*(9), 093039. https://doi.org/10.1088/1367-2630/ab4081

- Rerucha, S., Yacoot, A., Pham, T. M., Cizek, M., Hucl, V., Lazar, J., & Cip, O. (2017)., *Investigation of an iodine stabilized system based on narrow linewidth 633 nm DBR diode*. *Measurement Science and Technology*, *28*(4), 045204. https://doi.org/10.1088/1361-6501/aa5ab9

- Hrabina, J., Zucco, M., Philippe, C., Pham, T., Holá, M., Acef, O., Lazar, J., & Číp, O. (2017). Iodine absorption cells purity testing. *Sensors*, *17*(12), 102. https://doi.org/10.3390/s17010102

- Cizek, M., Pravdova, L., Minh Pham, T., Lesundak, A., Hrabina, J., Lazar, J., Pronebner, T., Aeikens, E., Premper, J., Havlis, O., Velc, R., Smotlacha, V., Altmannova, L., Schumm, T., Vojtech, J., Niessner, A., and Cip, O. (2022). *Coherent Fibre Link for synchronization of delocalized atomic clocks. Optics Express*, *30*(4), 5450. https://doi.org/10.1364/oe.447498

Conferences

- Pham, T. M., Cizek, M.; Hucl, V., Lazar, J., Hrabina, J., Rerucha, S., Lesundak, A., Obsil, P., Filip, R., Slodicka, L., Cip, O., *Analysis of Frequency Noise Properties of 729 Nm Extended Cavity Diode Laser with Unbalanced Mach-Zehnder interferometer. 20th Slovak-Czech-Polish Optical Conference on Wave and Quantum Aspects of Contemporary Optics*, doi: 10.1117/12.2264455. ISSN: 0277-786X WOS:000393152700013.

- Pham, T. M., Cizek, M., Lesundak, A., Hucl, V., Lazar, J., and Cip, O. (2018). Two-stage stabilization setup of the laser working on 729 nm for spectroscopy with cold 40ca+ ion. *2018 European Frequency and Time Forum (EFTF)*. https://doi.org/10.1109/eftf.2018.8409075

- Pham, T. M., Lesundak, A, Cizek, M, Rerucha, S, Lazar, J., Jedlicka, P., Cip, O., Podhora, L., Slodicka, L., *Meas-urement of Magnetic Field Stability Using Ca-40(+) ion.* 2021 *Joint Conference of the European Frequency and Time Forum and Ieee International Frequency Control Symposium (ieee Eftf-Ifcs 2021)*, isbn 978-1-66543-935-0. ISSN: 2327-1914 WOS:000784693000001.

- Pham, M. T., Hucl, V., Cizek, M., Mikel, B., Hrabina, J., Rerucha, S., Cip, O., Lazar, J., Narrow-linewidth tunable laser working at 633 nm suitable for industrial interferometry. *Optical Measurement Systems for Industrial Inspection Ix. Bellingham: Spie-Int Soc Optical Engineering, 2015*, vol. 9525, 95254N, isbn 978-1-62841-685-5. doi: 10.1117/12.2190748. ISSN: 0277-786X WOS:000357981400128. 53

- Philippe, C., Le Targat, R., Holleville, D., Lours, M., Minh-Pham, T., Hrabina, J., Du Burck, F., Wolf, P., Acef, O., IEEE, *Frequency tripled 1.5 mu m telecom laser diode stabilized to iodine hyperfine line in the 10(-15) range*, 2016, *30th European Frequency and Time Forum (EFTF),* APR 04-07, 2016, BN 978-1-5090-0720-2, UT WOS:000386307700072

- Podhora, L., Lachman, L., Pham, T., Lesundak, A., Cip, O., Slodicka, L., Filip, R., Quantum non-Gaussianity of multi-phonon states of a single atom, *Conference on Lasers and Electro-Optics Europe / European Quantum Electronics Conference (CLEO/Europe-EQEC), 2021,* DOI10.1109/CLEO/Europe-EQEC52157.2021.9542529

- Slodicka, L., Minh, TP., Lesundak, A., Hucl, V., Cizek, M., Hrabina, J., Rerucha, S., Lazar, J., Obsil, P., Filip, R., Cip, O., *Trapping and cooling of single ions for frequency metrology and quantum optics experiments*, *15th International Seminar on Recent Trends in Charged Particle Optics, and Surface Physics Instrumentation*, 2016 UT WOS:000391254000031

- Cip, O., Lesundak, A., Pham, M. T., Hucl, V., Cizek, Hrabina, J., Rerucha, S., Lazar, J., Obsil, P., Filip, R., Slodicka, L., *The compact setup for laser cooling and high-resolution spectroscopy with cold 40Ca+ ions*, *2018 European Frequency and Time Forum (EFTF)*, 2018, pp. 392-394, doi: 10.1109/EFTF.2018.8409077.